Prostate high dose-rate brachytherapy in men with bilateral hip prostheses.

David K Waterhouse

School of Chemistry and Physics

Faculty of Science

Adelaide University

AUSTRALIA

Presented as partial fulfilment of the requirements for the degree of Master of Science at Adelaide University

Abstract.

Bilateral hip prostheses challenge the acquisition of clinically useful treatment planning images for prostate HDR brachytherapy. Prostheses can introduce severe artifact into the principal modalities used for HDR prostate brachytherapy imaging – ultrasound, magnetic resonance imaging (MR) and computed tomography (CT). This study aimed to develop a protocol for clinically useful image acquisition that would ensure accurate and reliable implanted needle identification in all patients, including those with bilateral hip prostheses.

It was found that in conventional B-mode grey-scale ultrasound images used routinely for image guidance in brachytherapy procedures, artefact such as shadowing and reverberation were confounding factors for accurate HDR brachytherapy treatment planning and delivery. For MR imaging, spatial distortion due to local magnetic field disruption, local signal void within prostheses, and localised areas of high signal intensity near the prostheses all complicated image interpretation for treatment planning. On the other hand, CT images were generally free from distortion and were spatially accurate. The impact of volume averaging on the accuracy of needle tip identification was studied with models of steel implant needles, and CT level and window settings to ensure tip definition to within ±0.7 mm (ensuring dosimetric accuracy of better than 0.7%), were determined.

In a study of 91 patients with stainless steel needle implants and without hip prostheses, the mean caudal displacement before adjustment was 5.4 mm (SD 3.3 mm). Plastic needle implants in 14 patients with bilateral hip prostheses was examined, and the mean caudal displacement before adjustment was 1.6 mm (SD 3.1 mm). Nitinol marker wires developed for use in plastic needles implanted into prosthesis patients were found to be superior when compared with standard rigid obturators. The wires, with the same flex properties as an active Ir-192 source wire, assist accurate identification of needle tips and may also provide an improved match to the treatment geometry for treatment planning purposes.

The impact of stainless steel and plastic needle movement on treatment efficacy was studied via Tumour Control Probability (TCP) calculations using three different TCP models and simulated brachytherapy treatment plans. This study showed that it was feasible to maintain displacements less than 3 mm, and that if this limit were adopted, it would result in most patients having TCP close to or greater than 95% of the original.

Statement of originality and acknowledgement.

This work contains no material accepted for the award of any other degree or diploma in any university or other tertiary institution and, to the best of my knowledge and belief, contains no material previously published or written by another person, except where due acknowledgment is made in the text.

I give consent to this copy of my thesis, when deposited in the University Library, being made available for loan and photocopying.

David K Waterhouse
March 2011

Acknowledgements.

This work is the summation of small, and not so small, contributions from many people. I am deeply indebted to Pete Camille, who quite simply is a really good bloke. Pete spent many hours chasing images, negotiating for time on CT and MR scanners, carting the BLIP phantom around, and sending data everywhere for me. He also certainly spent many hours pondering the sense of some of my ideas. I owe Pete many thanks.

To my three supervisors, I offer many thanks. Judith Pollard at Adelaide University is excellent – a strong supporter, and a patient listener. Wearing his supervisor's hat, Martin Ebert made the right noises at the right times and this project is better for his subtle steering. Annette Haworth kept the pressure on, and was an excellent monitor of my progress. Without Annette's determination, this report may well have been lost in the pile of gunna's at the bottom of my cellar.

Nikki Caswell deserves my sincere thanks in no small measure. No one person has helped me more in Radiation Oncology Medical Physics than Nikki. Thankyou.

To Pete Lanzon and the physics and radiation therapy staff at SCGH: many thanks for providing a friendly, engaging, and altogether good workplace. Thanks to Dr Albert Tiong and to Katherine Langham at SCGH for their work (including much of the statistical analysis) in the numerous needle shift studies that were undertaken by us.

Many, many others deserve thanks as this project spanned four hospitals in three states — Sir Charles Gairdner Hospital in WA, Royal Adelaide Hospital in SA and The Peter MacCallum Cancer Institute and The Epworth Tattersalls Cancer Centre in Victoria. Specific highlights include: Brendan McKernan's unending help with various incarnations of the BLIP phantom; Pete Lanzon's sell-out Australian tour with the same phantom; Rob Day's assistance with the acquisition of hip prostheses (some used, some new); Eric Carlson at Stryker for providing lots of prosthesis data; Natalie Clements for her invaluable contribution towards my literature searches, and the HDR brachytherapy team at Royal Adelaide Hospital for their hospitality and assistance with ultrasound-based HDR treatment planning. Thanks to Karl Roozen and all in 'the swamp' at Peter Mac East Melbourne for making my 12 months in there a very enjoyable experience.

My family - Beck, princess Katie, and little Abbie....

Table of Contents.

List of Figures.

List of Tables.

Chapter 1 . Introduction.

Prostate high dose-rate (HDR) brachytherapy as a boost treatment following conventional external-beam radiotherapy (EBRT) is becoming more prevalent (Guedea *et al.*, 2011). The primary aim of this work was to develop a protocol for the effective and reliable acquisition of clinically useful image data for HDR prostate brachytherapy treatment planning in patients with bilateral hip prostheses. A concurrent aim was to ensure that bilateral hip prosthesis patients receiving prostate HDR brachytherapy achieved at least as good treatment dosimetry outcomes as non-prosthetic patients. Specific questions addressed in this work were:

- Is there an optimal prostate imaging technique for patients with bilateral hip prostheses? This work assessed ultrasound (U/S), magnetic resonance (MR or MRI) and computed tomography (CT) imaging modalities, with particular emphasis upon accurate and reliable imaging of implanted brachytherapy needles.

- Which needle type is better? Stainless steel and plastic implant needles with stainless steel and nitinol (50:50 Ni:Ti alloy) obturators were assessed to determine which offered an optimum imaging solution.

- Are inter-fraction needle movements different? Needle movement between the two or three fractions of radiation dose commonly delivered in HDR brachytherapy boost treatments can be significant. This work investigated differences in movement between stainless steel and plastic needles, and used Tumour Control Probability calculations to indicate the radiobiological efficacy of radiation dose delivery to the target volume. This work also investigated the variation of TCP with needle movement in the target volume.

In a typical prostate HDR brachytherapy procedure at SCGH, 15 hollow stainless steel or plastic needles are inserted into the prostate via the perineum. Occasionally at SCGH 16 or 17 needles were implanted into large prostates. It is common practice to obtain x-ray computed tomography (CT) images of the patient's pelvic region to enable needle identification for treatment planning using volume-based, dose optimised computerised planning techniques. At Sir Charles Gairdner Hospital (SCGH), a growing number of prostate HDR patients present with bilateral hip prostheses. Prostheses introduce

significant artifact and signal deficit to CT images, making it difficult to discern soft tissue detail in the brachytherapy target volume. The radiation oncologist must then rely upon a combination of pre-implant images obtained from a trans-rectal ultrasound (TRUS) volume study, implanted fiducial markers, and memory, to define the treatment volume. The situation is not much improved with magnetic resonance (MR) images, due to magnetic susceptibility artifact and signal distortion from the prosthesis components. As well, the distal tips of implanted needles can be difficult to identify with sufficient accuracy. Image flare at the needle tips can be problematic for high density stainless steel needles but conversely for plastic needles, their similarity to soft tissue density can also make the needle tips difficult to identify.

In Chapter 2 an overview of treatment options for prostate cancer patients is presented, and the radiobiological basis for HDR brachytherapy is discussed. It will be shown that HDR brachytherapy offers a sufficiently high clinical advantage for prostate cancer that it is well-worthwhile developing a protocol to obtain suitable images for treatment planning in patients with bilateral hip prostheses. Chapter 2 also describes the composition of typical hip prostheses and the prevalence of different prostheses in Australia. Additional detail on prostheses is provided in Appendix 1. Chapter 2 concludes by estimating the number of men with bilateral hip prostheses who will present for HDR brachytherapy in any year.

The location of an irradiating Ir-192 source in any existing brachytherapy after-loading device is referenced to the distal tip of each implanted needle. Hence, while HDR brachytherapy treatment delivery is very precise, it is only as accurate as identification of distal needle tips will allow. Needle tip identification is heavily dependent upon image quality, and Chapter 3 discusses the human eye, DICOM grey-scale medical imaging, and windowing and levelling for contrast and detail enhancement. Each of the imaging modalities mentioned earlier has advantages and disadvantages for HDR brachytherapy treatment planning. The selected imaging technique must provide adequate soft tissue detail and accurate spatial information about the implanted needles. Challenges in the CT, MR and U/S imaging modalities that are typically used to acquire suitable images for HDR brachytherapy treatment planning of prostate tissue and implanted needles that lie between bilateral hip prostheses are described. Chapter 3 concludes with a summary of the prospects of successful image acquisition with each investigated modality with respect to a set of criteria that define clinically useful prostate HDR brachytherapy images.

In Chapter 4 the CT, MR and U/S imaging modalities typically used for HDR brachytherapy treatment planning image acquisition are examined in more detail (the well-documented theory of each modality is presented for completeness in Appendix 2). The results of phantom studies aimed at optimising images for HDR prostate brachytherapy implants situated between bilateral hip prostheses are presented and discussed. In this work, a phantom was developed to test the impact of bilateral hip prostheses on the clarity and utility of different imaging modalities. As well, a new CT and MR compatible marker wire for plastic needles was developed, and a revised approach to needle tip identification using the marker wires is discussed. For MR, the challenges of imaging without an endorectal coil are made evident. For CT, the impact of partial volume effects on needle tip definition is examined, and use of U/S for 'real time' treatment planning and pre-implant volume study acquisition is discussed. For each imaging modality, results obtained from in-vivo scans are compared and contrasted.

The needle locations recorded in treatment planning images, howsoever obtained, form the baseline dataset for treatment planning and subsequent treatment delivery. Chapter 5 investigates and characterises the effects of inter-fraction needle displacements in HDR prostate brachytherapy. At each treatment fraction, the observed needle locations may be compared with the baseline locations and treatment conditions can be modified to compensate for observed displacements. The differences between patients with and without prostheses are compared and contrasted, and treatment dosimetry parameters and their potential impact on tumour control are discussed and demonstrated. Chapter 5 is based upon work published in a peer-reviewed journal article (Tiong *et al* 2009). The text was largely revised compared with the publication, and all of the bilateral hip prosthesis patient analysis was done by the candidate. Stainless steel needle shift data were analysed by Tiong, and the candidate was directly involved in data accumulation and initial processing. The TCP calculations were completed by Caswell and Ebert, using software developed by Ebert and the candidate (published in Haworth *et al* 2004a,b). The TCP calculations were repeated by the candidate to obtain absolute rather than relative values. Contributors to needle displacement were analysed by Langham *et al* (2006) and the candidate contributed by way of data acquisition and some assistance with data analysis. The work on clinically determined needle shifts was done by the candidate.

Chapter 6 provides a summary of this thesis and discusses potential directions for future research.

Chapter 2 . Prostate cancer treatment and hip prostheses.

Prostate cancer accounts for about 25% of all new cases of cancer in males, and about 9% of all cancer-related deaths in men (Jemal *et al.*, 2009). The introduction of diagnostic prostate specific antigen (PSA) tests after 1987, combined with digital rectal examination, assists early detection (Smith *et al.*, 2009b), and some (Sun *et al.*, 2007) suggest a PSA threshold of 2.5ng/ml and PSA velocity > 0.60 ng/ml/yr are acceptable markers of being at high risk of prostate cancer.

Prostate cancer severity is classified by the tumour size, node involvement, and presence of metastases (TNM) score (Sobin *et al.*, 2009). Tumour aggressiveness is indicated by the Gleason score (Gleason and Mellinger, 1974) – a number, range 2-10, that sums the two most common tumour growth patterns found in trans-rectal ultrasound-guided biopsy specimens (Punnen and Nam, 2009). However, the need for aggressive therapy is not clear-cut as some prostate cancers grow slowly and are unlikely to become life-threatening, or even to produce symptoms before the patient dies from other causes.

2.1 Treatment options for men with prostate cancer.

Clinical markers such as Gleason score, PSA, and clinical stage assist to determine a patient's risk group and treatment options:

2.1.1 Watchful waiting / active surveillance.

Disease progression is monitored and treatment is deferred until needed. For some patients the psychological impact of 'doing nothing' can make this approach undesirable. Active surveillance may not be demonstrably worse than other treatment options (Bill-Axelson *et al.*, 2008) for a 'low risk' patient (PSA < 10 ng/ml, biopsy Gleason score ≤ 6, T1c–T2a, life expectancy < 10 yr). PSA-doubling times below three years and repeat biopsies indicate the need for treatment intervention.

2.1.2 Radical prostatectomy.

Surgical resection is the most common treatment for prostate cancer (Sriprasad *et al.*, 2009), and recent developments include laparoscopic and robotic surgery. To preserve

quality of life, nerve-sparing procedures to maintain potency and continence are routine for men with localised disease and normal erectile function. For men with low risk disease (T1c, PSA < 10ng/ml, Gleason ≥ 6) the risk of lymph-node involvement is low, but a pelvic lymphadenectomy is recommended for men with intermediate (T2a, PSA 10-20 ng/ml, Gleason > 7) or high risk disease (>T2b, PSA > 20 ng/ml, Gleason > 8). A combined surgical and radiotherapy approach may be used for T3 disease due to the risk of positive lymph nodes and/or positive resection margins.

2.1.3 Androgen deprivation.

That prostate cancers shrink and can be 'down-staged' by androgen deprivation was shown long ago (Huggins and Hodges, 1941). Recent analysis (Shelley *et al.*, 2009) showed that neo-adjuvant hormone therapy can improve disease-free survival when given with radiotherapy, and in patients undergoing surgery who show positive margins or lymph nodes, but it may not improve overall survival compared with radiotherapy or prostatectomy alone. Others (Valero *et al.,* 2009) showed that androgen deprivation combined with EBRT and an HDR brachytherapy boost has similar 5-year outcomes as for EBRT with androgen deprivation alone. Side effects of androgen deprivation include hot flushes, gynaecomastia, and haematological complications.

2.1.4 External Beam Radiation Therapy (EBRT).

Prostate EBRT uses a linear accelerator (linac) to deliver well-collimated high energy (typically 6 or 18 MV) photon irradiation to a target volume at the linac gantry's rotation isocentre. The targeted volume usually includes a margin for setup and delivery uncertainties, for prostate motion with respect to reference anatomical structures, and in high risk patients a margin may be included for nodal and seminal vesicle involvement. A sequence of linac gantry angles are used, and with multi-leaf collimators (MLC's) the radiation field shape can be matched to the apparent target shape at each linac gantry angle, reducing the amount of irradiated normal tissue, allowing higher target doses. The total radiation dose to any point is the sum of dose delivered to that point from each treatment angle, and dose to normal tissues in the individual beam paths is reduced. The target volume dose is typically homogenous, to within -5% to +7% of the prescribed dose. Repair mechanisms in normal tissue tend to be more efficient than in tumour tissue, and a differential response becomes apparent with fractionated dose delivery over days or weeks.

EBRT dose escalation. The radio-sensitivity of prostate cancer is characterised by its α/β ratio. For prostate cancer, spirited debate on the α/β ratio – summarised by Ritter (2008) and by Lee (2009) – continues, but it is believed to be low (Ahmad *et al.*, 2009; Williams *et al.*, 2007; Nickers *et al.*, 2010; Bentzen and Ritter, 2005; Fowler, 2005). Hypo-fractionated treatment may thus improve tumour control for prostate cancer, but at the potential cost of damage to late-responding normal tissues such as rectal tissue. Biochemical disease-free survival data (Zelefsky *et al.*, 2008) showed that dose > 72 Gy is useful to control low-risk prostate cancer. For intermediate and high risk patients, dose escalation to 78 Gy can be beneficial (Kuban *et al.*, 2008).

Intensity modulated radiotherapy. IMRT is an EBRT technique that uses conformal field shapes and dynamic or step-and-shoot beam intensity control, so that different portions of the irradiated field can receive different dose. IMRT delivery can achieve much tighter conformal dose around a tumour, reducing dose to surrounding normal tissue when compared with 3D conformal EBRT. The delivered dose can be made deliberately heterogeneous in the target volume to (for example) reduce dose to the urethra while increasing dose to known tumour sites within the prostate. At the same time, dose to nearby organs at risk such as the rectum and bladder can be reduced. IMRT demonstrates improved survival data compared with conventional EBRT (Cahlon *et al.*, 2008a; Zelefsky *et al.*, 2008; Alicikus *et al.*, 2011) and potentially reduced long term toxicity even for significantly increased dose prescriptions (Cahlon *et al.*, 2008b; Alicikus *et al.*, 2011). IMRT is a complex technique that is relatively new, and survival and toxicity outcomes may further improve as the technique matures and longer term data become available.

2.1.5 Brachytherapy.

Brachytherapy delivers dose to target volumes from ‘inside-out’, compared with EBRT modalities that deliver dose from ‘outside-in’(Koukourakis *et al.*, 2009). The relatively low energy of the radioactivity ensures steep dose gradients, enabling high conformality to the target volume and an opportunity to minimise dose to nearby organs at risk. In contrast with EBRT, brachytherapy doses are highly heterogeneous, and 35% (or more) of the target volume may receive 150% of the prescribed dose.

Low dose-rate brachytherapy (LDR). Transperineal LDR brachytherapy involves permanent implantation of around 100 small radioactive I-125 or Pd-103 ‘seeds’ into the

prostate. It is a technique that in Australia can be applied to patients with prostate cancers of stage T1b–T2a N0, M0, and Gleason score ≤ 7, assessed on a sufficient number of random biopsies, and an initial PSA level < 10 ng/ml. Recurrence-free survival after 5 years typically exceeds 95%, and 10-year recurrence free survival is 80% or higher, depending upon the reporting institution (Morris *et al.*, 2009; Zelefsky *et al.*, 2007). It is known that a prostate volume lower than 50 cm^3 and a good International Prostatic Symptom Score are indicators for successful treatment. About 10% of patients experience acute symptoms such as urinary retention shortly after implantation, which may lead to incontinence (Keyes *et al.*, 2009). LDR brachytherapy is characterised by highly conformal treatment volumes, and recent work (Stone *et al.*, 2009) suggests that when combined with EBRT it can be an effective treatment option for localised high-grade prostate cancer.

High dose-rate prostate brachytherapy (HDR). The average energy of gamma-rays emitted by Ir-192 is 370 keV, making it an attractive short-range high dose-rate radiation source. For HDR brachytherapy, a single high-activity (~150 Gyh^{-1}) Ir-192 source contained within a remote after-loading device is remotely driven into hollow needles temporarily implanted in and around a target volume to deliver a short-range radiation dose. The time the source dwells at a particular location determines the radiation dose it delivers to that point, allowing precise control of dose and treatment volume conformality. Unlike in EBRT where the photon beam is well collimated, gamma radiation is nearly isotropically emitted from an Ir-192 source and dose follows the inverse square law. Interstitial HDR brachytherapy irradiates the tumour from the inside out, and compared with EBRT, smaller volumes of normal tissue are irradiated. A key advantage of tissue sparing is that higher tumouricidal dose can be delivered. Extensive dose fractionation is not required and the effective dose $E = \alpha D + \beta dD$ is increased because dose d per fraction can be higher (6 - 10 Gy). Compared with weeks of EBRT treatment, the accelerated schedule is convenient, however HDR brachytherapy is more suited to small to medium tumours in patients fit enough to undergo a surgical procedure with anaesthesia. HDR is commonly used as a boost treatment with EBRT (Bachand *et al.*, 2009; Kovacs *et al.*, 2005; Pisansky *et al.*, 2008), and typically 14 - 20 Gy in 2 - 3 fractions is prescribed. High dose per fraction and excellent target volume conformality exploit the radio-sensitivity of prostate cancer tissue. The efficacy of HDR boost treatments is demonstrated by 5-year relapse-free survival in over 90% of low risk, 85% of intermediate risk, and 65% of high risk patients, with morbidities comparable with EBRT alone (Duchesne *et al.*, 2007).

Evidence is accumulating for the efficacy of HDR as a monotherapy (Corner *et al.*, 2008; Demanes *et al.*, 2011), but it is not yet in widespread use.

2.2 Radiobiological basis for HDR brachytherapy boost treatments.

The goal of radiotherapy in cancer treatment is to kill cancer cells while sparing healthy tissue. The 4 R's of radiotherapy – repair of DNA damage, redistribution through cell phases after irradiation, repopulation of healthy stem cells (and tumour cells), and re-oxygenation – well documented by Steel (2002), or Giaccia and Hall (2006) describe the biological processes that occur during and after irradiation, and that modify the radiation response of tissues. Eventually, loss of successfully dividing stem cells may lead to clinically observable consequences of a deficit of differentiated cells within tissue. The Linear-quadratic (LQ) model (Chadwick and Leenhouts, 2005; Kellerer and Rossi, 1971) that describes the fraction of cells surviving irradiation is:

$$\text{Surviving Fraction } S = \exp-(\alpha D + \beta D^2) \qquad (2.1)$$

where the total dose $D = nd$ (n fractions of dose d). Irreparable damage is represented by α, and β represents repairable damage. Typically α is set to 0.30-0.35 Gy^{-1}, and the dose at which $\alpha D = \beta D^2$ is $D = \alpha/\beta$. A small α/β ratio indicates good repair capacity and hence low radio-sensitivity, while large α/β ratio indicates poor repair capacity and therefore high sensitivity. Fractionation of dose delivery allows time for normal cells to repair and repopulate between fractions, and in fractionated treatment the effective dose is higher to late-responding tissue ($\alpha/\beta \approx 3$ Gy) than to early-responding ($\alpha/\beta \approx 10$ Gy) tissue. Late-responding tissue is more sensitive to high dose per fraction, and as the α/β ratio may be as low as 1.5 Gy for prostate cancer (Fowler, 2005; Brenner *et al.*, 2002; Williams *et al.*, 2007; Wang *et al.*, 2003), the ability of HDR brachytherapy to deliver significantly higher target doses with each fraction while sparing surrounding tissue is particularly attractive (Duchesne and Peters, 1999; Ritter *et al.*, 2009).

2.2.1 Effect of radiation on normal tissue.

For any tissue, cell repair rates limit the radiation damage that can be tolerated before complications and toxicities arise. Typical tumour cells proliferate more quickly than normal healthy cells, and a comparable dose of radiation is likely to kill more tumour than

normal cells. Figure 2-1 shows the probability of tumour cell kill (Tumour Control Probability – TCP), and the likelihood of complications in normal tissue (Normal Tissue Complication Probability – NTCP) as a function of radiation dose. A key feature is that usually the TCP curve leads the NTCP curve. The slope and starting point of the dose response curves depends upon the organ's radiation sensitivity and its architecture (serial – nerves, intestine; parallel – kidney, bladder).

Radiotherapy aims to deliver a dose D corresponding to the peak in the blue curve in figure 2-1, where TCP and NTCP values are optimised. However at this point, small deviations from target dose D can significantly reduce TCP, or increase NTCP. By minimising the amount of irradiated normal tissue, the total dose D that can be delivered to tumour tissue is higher, thus increasing TCP, while NTCP is kept at or below a threshold value.

NOTE:
This figure is included on page 9 of the print copy of the thesis held in the University of Adelaide Library.

Figure 2-1: Tumour control probability (TCP – green curve), Normal tissue complication probability (NTCP – red curve), optimum dose response curve (blue). From http://www.dkfz.de/en/medphys/appl_med_rad_physics/Biological_models.html

Depending upon the tumour location and the type of surrounding normal tissue, damage caused by exceeding the normal tissue tolerance dose can range from minor loss of quality of life, to death. For EBRT treatments skin irradiation is unavoidable, with moist desquamation and ulceration being common complications when the skin tolerance dose is exceeded. Other site-dependent complications include pneumonitis in the lungs, eye cataracts, heart failure, and paralysis due to excessive spinal cord irradiation (Steel 2002, (Kunkler, 2003a). Once a tissue's tolerance dose is reached no additional radiation can be

delivered without inducing complications, making it vital that the delivered dose is maximized the first time (Kunkler, 2003a, b). With normal tissue complications in mind, curative radiotherapy techniques are still limited by dose to normal tissue.

Target conformality enables delivery of more dose to tumour tissue before exceeding dose limits for normal tissue and organs at risk (for prostate irradiation the small bowel, rectum, and bladder are organs at risk). For EBRT, target volume dose conformality can be improved with pre-treatment imaging techniques such as electronic portal imaging, cone-beam CT and mega-voltage on-board imaging techniques. HDR brachytherapy is a highly conformal treatment modality in which the highest doses are concentrated within the target volume, however dose to nearby surrounding tissues, and the patient's integral dose, is reduced. Indeed, Bowes and Crook (2011) suggest that brachytherapy may be the optimal technique for intra-prostatic dose escalation.

2.2.2 EBRT with HDR brachytherapy boost.

The strengths of HDR brachytherapy complement the weaknesses of EBRT, and vice versa, resulting in very good tumour dose delivery and better avoidance of healthy tissues. Where EBRT treatment requires margins around the gross tumour volume to account for setup uncertainties and organ motion in the external beam's eye view, HDR brachytherapy can set zero margins as the radioactive source moves when the patient or organ moves. This feature alone allows tighter dose conformation. There is (usually) an inherently more rapid dose fall-off outside the tumour in HDR brachytherapy than in EBRT and IMRT – for example at a point 1cm outside the target volume, the typical IMRT treatment dose will be ≈ 60% of the target dose, whereas for HDR Ir-192 brachytherapy the dose will be only 30%. However, HDR cannot reproduce the dose homogeneity of EBRT (Fatyga *et al.*, 2009), and up to 35% of the target volume can receive at least 150% of the prescribed dose. In contrast, with EBRT the maximum target dose typically does not exceed 107% of the prescribed dose. Deutsch *et al* (2010) reported enhanced therapeutic ratios and reduced complication rates when IMRT + HDR boost was compared with IMRT alone, while Pieters *et al* (2008) found the combination improved tumour coverage and maintained acceptable doses to surrounding critical organs. Others (Martin *et al.*, 2011) recently published guidelines to assist prostate IMRT treatment planning optimisation.

For any patient, not just those with bilateral hip prostheses, the advantages of developing a suitable imaging technique to provide clinically useful images for prostate HDR brachytherapy treatment planning are clear. The radiobiological rationale for combining an HDR brachytherapy boost with EBRT is compelling. As well, prostate HDR brachytherapy offers accelerated treatment schedules and highly conformal dose distributions that spare large volumes of healthy tissue from radiation, while EBRT (particularly IMRT) provides highly uniform dose throughout the target volume. Avoidance of critical structures using IMRT, and dose reduction to healthy tissue using HDR brachytherapy offers a beneficial combination for the recipient patient.

The challenge, that this work addresses, is to obtain images of the treatment target volume and implanted brachytherapy needles with sufficient detail to enable accurate and precise HDR brachytherapy radiation dose delivery. Unfortunately, clinically available hip prostheses are significantly more dense than human tissue and bone, and typically contain metals that introduce artifacts into each of the imaging modalities investigated here – ultrasound, computed tomography and magnetic resonance imaging.

2.3 Bilateral hip replacements.

A typical modern total hip prosthesis system is shown in Figure 2-2. The femoral head is press-fitted onto the stem and articulates against a specialised liner in the acetabular cup. The stem is inserted into the femur, and the acetabular shell or cup is fitted into the acetabulum. The stem and cup can be cemented, screwed, or press-fitted into the bones. The history and characteristics of hip prostheses is discussed in more detail in Appendix 1.

NOTE:
This figure is included on page 11 of the print copy of the thesis held in the University of Adelaide Library.

Figure 2-2: Typical modern total hip replacement system, exploded view (image adapted from Exactech, Inc., Florida USA).

2.3.1 Prostheses types and compositions.

According to the Australian Orthopaedic Association (Graves *et al.*, 2009), in Australia more than 100 different types of femoral stems were used in 2008, but the 10 most frequently used stems accounted for 68% of all implants. Overall the two most common stems, the Exeter V40 (Stryker) stainless steel stem for cemented insertion and the Corail (DePuy) forged titanium stem for cementless insertion, accounted for nearly 36% of all implants. Prior to 2008, the Synergy (Smith-Nephew) forged titanium stem for cementless insertion was common. Similarly, more than 80 different types of acetabular cup were used in 2008, but the Trident (Stryker) titanium acetabular cup and the Pinnacle (DePuy) titanium cup accounted for nearly 40% of all cups inserted. The Reflection (Smith-Nephew) alumina-ceramic acetabular system was also widely used. In the late 1990's the Spectron EF (Smith-Nephew) cobalt-chrome system was common, as was the ABGII (Stryker) cobalt-chrome system. It appears that Australian surgeons are moving away from cobalt-chrome inserts. The composition of prosthesis components is shown in Table 2-1.

COMPOSITION OF HIP PROSTHESES						
	Stainless steel		CoCr Alloy		Titanium Alloy TiAl6V4	
	ASTM F 1586		ASTM F 1537		ASTM F 136	
Element	Weight %		Weight %		Weight %	
	Min	Max	Min	Max	Min	Max
Iron (Fe)	58.0	66.0		0.8		0.3
Cobalt (Co)			60.0	65.0		
Chromium (Cr)	19.5	22.0	27.0	30.0		
Titanium (Ti)					89.0	91.0
Molybdenum (Mo)	2.0	3.0	5.0	7.0		
Vanadium (V)					3.5	4.5
Aluminum (Al)				0.3	5.5	6.5
Nickel (Ni)	9.0	11.0		1.0		
Manganese (Mn)	2.0	4.3		1.0		
Niobium (Nb)	0.3	0.8				
Silicon (Si)		0.8				
Copper (Cu)		0.3				
Electron Density (relative to water)	6.51		6.73		3.66	

Table 2-1: Elemental composition of hip prostheses and acetabular cups. The most commonly implanted components in Australia today are stainless steel and titanium alloy stems, with titanium alloy acetabular cups. In the 1990's cobalt-chrome stems were popular.

For projection x-ray imaging techniques such as fluoroscopy and CT, the electron density of a material is indicative of the amount of dose that will be absorbed by the object. Materials with high electron density, such as stainless steel, absorb more x-rays and hence appear dark on fluoroscopy images. Downstream from the object the reduced x-ray intensity leads to loss of detail and reduced exposure, reducing image contrast. For this reason, titanium prostheses would be preferred over stainless steel or cobalt-chrome prostheses.

Magnetic susceptibility indicates how strongly a material will interact with a magnetic field, providing a guide to the amount of spatial distortion and loss of signal that may be observed. More artifact is observed in materials with higher magnetic susceptibility (Thomsen *et al.*, 2001; Kolind *et al.*, 2004). Stainless steel components with high ferromagnetic composition produce most artifact in MRI images, followed by cobalt-chrome alloys. Titanium alloys produce less artifact and are less likely to interfere with prostate HDR brachytherapy image acquisition for treatment planning.

2.3.2 Prevalence in men with prostate cancer.

The load-bearing hip joint is subject to wear, deterioration, and degeneration over time. Osteoarthritis, rheumatoid arthritis, osteonecrosis, bone injury, and bone tumours all lead to joint breakdown. Much of the available data on hip and prostate disease and treatment trends relates to the US population, and these data will be used in the following discussion. Between 75% and 97% of total hip replacements are undertaken to alleviate the symptoms of osteoarthritis (Merx *et al.*, 2003; Birrell and Felson, 2009), and a recent meta-study (Dagenais *et al.*, 2009) found the prevalence of radiographically detectable hip osteoarthritis in males is about 8.5%.

In the US, about 100 000 total hip replacements are performed on men each year (AAOS, 2009), with more than ten-fold higher prevalence in the 60+ age group than in the sub-60 age group (Eskelinen *et al.*, 2005; Lohmander *et al.*, 2006). The average hip patient is 60 – 70 years old (Ackerman *et al.*, 2009). The life expectancy for American males aged 65 is 20 years (Arias, 2007), and it may be estimated that 8.5% of the 23 million US men aged over 60 have a total hip replacement. Australian data (Graves *et al.*, 2009) indicates that 12% of subjects have had both hips replaced within 8 years of an initial replacement. Therefore, about 300 000 men over 65 in the US have a bilateral hip replacement.

Prostate cancer. In recent times in the US, the lifetime risk of developing prostate cancer was 1 in 6. Over 200 000 new cases of prostate cancer are diagnosed each year, and 95% of those men are over 55 years of age. Studies suggest that hip prostheses do not significantly affect the incidence of cancer (Gillespie *et al.*, 1988; Visuri *et al.*, 2006), so that we might expect 8.5% or 17 000 men newly diagnosed with prostate cancer will have had a total hip replacement, and that about 2 400 will have bilateral hip prostheses.

Radiotherapy. The proportion of prostate cancer patients selecting radiotherapy as their primary treatment modality increased from 30% prior to 1995, to more than 45% in 2002 (Warren *et al.*, 2008). Within the patient cohort who select primary radical prostatectomy, almost 15% received secondary radiotherapy treatment (Krupski *et al.*, 2006). We might therefore expect that 10000 men with total hip replacements will present for radiotherapy treatment in the US each year, and that more than 1200 will have bilateral hip prostheses.

Differences in local or regional preferences for prostate cancer treatment, or in the rate of prosthetic hip use, or variations in population demographics, will affect the number of prostate cancer patients with prostheses presenting for HDR brachytherapy treatment. However, as populations age and life expectancy increases, the incidence of prostate cancer will rise (Smith *et al.*, 2009a) and the prevalence of hip prostheses is predicted to more than double over the next 30 years (Birrell *et al.*, 1999; Kurtz *et al.*, 2007), and the challenge of obtaining clinically useful images for prostate brachytherapy treatment planning in patients with bilateral hip prostheses will become more frequent.

Applying the statistics to SCGH. Similar estimates can be developed for SCGH, using Australian data from Graves *et al* (2009), the ABS (2009), and the AIHW (2005). Each year more than 500 men are treated for prostate cancer using radiotherapy at SCGH, and nearly 100 of them receive HDR brachytherapy. We may reasonably expect that every year 2 or 3 men with bilateral hip prostheses will present for HDR brachytherapy. In the 5 years during which data were acquired and analysed for this work, SCGH applied HDR brachytherapy to 16 prostate cancer patients with bilateral hip replacements, in reasonable agreement with the estimates given above. Prior to HDR brachytherapy the patient's medical records were retrieved, or their orthopaedic surgeon was contacted, to determine the implanted prostheses compositions. Table 2-2 below summarises the prosthesis materials used in the treated patients.

Patient	Lt Cup	Rt Cup	Lt Stem	Rt Stem
1	Co	Co	Co	Co
2	Co	Ti	Co	Co
3	Ceramic	Co	Ti	Co
4	Ceramic	Ceramic	Ti	Ti
5	Ti	Ti	Co	Co
6	Ti	Ti	Co	Co
7	SS	SS	SS	SS
8	Ti	Ti	Co	Co
9	Ti	Ti	Co	Co
10	Ti	Ti	Co	Co
11	SS	Ti	SS	Co
12	Ti	Ti	Co	Co
13	Ti	Ti	Co	Co
14	Ti	Ti	Co	Co
15	Ti	Ti	Co	Co

Table 2-2: Composition of hip prostheses and acetabular cups in patients treated at SCGH. Co = cobalt-chrome, Ti = titanium, SS = stainless steel, Ceramic = aluminium oxide ceramic.

SCGH patients included in this study had total hip replacements between 1986 and 2004, when cobalt chrome prostheses were popular. As table 2-2 shows, all but four patients received cobalt-chrome stems with titanium-shell UHWMPE acetabular cups. One patient had two stainless steel prostheses, and one patient had a stainless steel prosthesis in one hip and cobalt-chrome in the other. Considering recent trends in prosthesis use, the popularity of cobalt-chrome stems may be waning, and stainless steel or titanium prosthetic stems may be encountered more frequently in the future. According to Graves *et al*, (2009) cementless insertions using titanium components account for more than 60% of current implants in Australia. Stainless steel stems tend to be used in procedures where the stem is cemented into the femur.

Chapter 3 . Imaging for HDR prostate brachytherapy treatment planning.

Imaging has a key role in prostate cancer management and identification. For prostate brachytherapy, trans-rectal ultrasound (TRUS) is used for cancer staging and for guidance during biopsies, and has an important role in needle guidance during an HDR brachytherapy implant procedure. Fluoroscopic x-ray imaging is used during implantation and treatment to monitor the prostate and needle locations. Computed tomography (CT) assists diagnosis and staging of more advanced prostate disease, and so far is the preferred modality for treatment planning in HDR brachytherapy. Magnetic resonance imaging (MR) and particularly endorectal coil MR provide high-quality images of localised prostate cancer, but MR-compatible HDR brachytherapy is challenging.

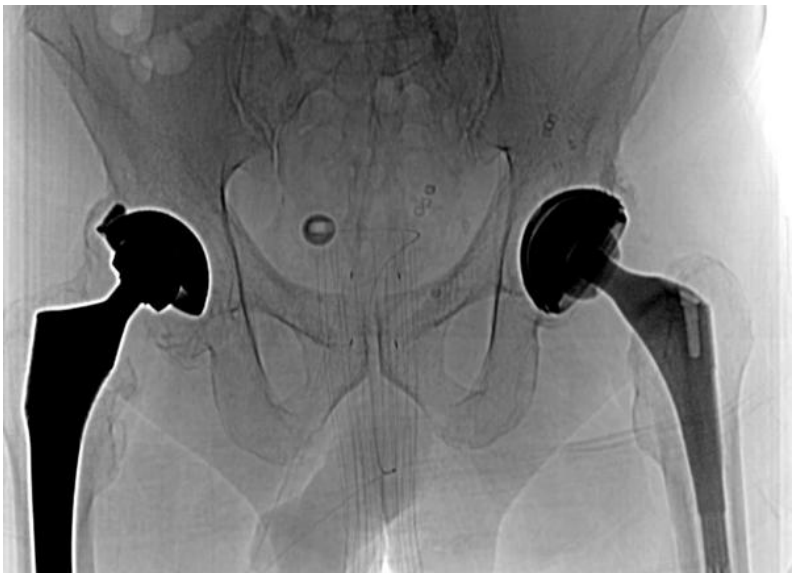

Figure 3-1: Fluoroscopic x-ray image of implanted plastic needles with obturators. Prostate tissue cannot be distinguished, and implanted fiducial markers are essential for localisation.

CT and TRUS presently are the preferred imaging modalities for prostate HDR brachytherapy treatment planning, but hip prostheses are made from materials with significantly higher density than human tissue and bones (figure 3-1). They are relatively opaque to low energy x-rays, and projection x-ray imaging techniques such as fluoroscopy or CT are thus at a disadvantage when visualising the prostate through hip prostheses. Significant density differences from normal tissue mean that prostheses are highly reflective to U/S, and the relatively short range of U/S signal typically precludes it as an external prostate imaging technique. Hip prostheses also contain materials with comparatively high magnetic susceptibility, making MR imaging challenging too.

3.1 Criteria for clinically useful images.

Conventional imaging techniques used in HDR prostate brachytherapy may not provide clinically useful images from patients with bilateral hip prostheses. The selected modality must provide adequate visualisation of prostate tissue (or implanted surrogate markers) for accurate target delineation for treatment planning, and during pre-treatment patient set-up and quality assurance.

A key requirement in HDR prostate brachytherapy is accurate identification of each needle implanted into the prostate. Needles must be clearly separable from patient anatomy to enable accurate treatment planning and delivery, and without adequate visualisation, HDR brachytherapy treatments cannot proceed. Usually each needle projects slightly beyond the prostate base, typically with distal ends in line with the femoral heads.

In the co-ordinate systems typically employed by HDR brachytherapy afterloaders, distal needle tips define the 'origin' from which all Ir-192 source dwell positions are referenced. Given the high dose gradients in HDR brachytherapy, it is especially important that distal tips are identified accurately; if accurate and reliable tip identification is not possible, the needle cannot be used for treatment. GEC-ESTRO (Kovacs *et al.*, 2005) recommends the uncertainty at treatment delivery should not exceed 3 mm from the treatment plan. Given the likelihood of needle movement within a patient between planning and treatment (see chapter 5), this places high demands upon the accuracy required of needle tip definition.

The impact of inaccurate needle-tip definition can be illustrated with an example. Figure 3-2 shows the difference between the calculated TG-43 dose distribution for an Ir-192 source located accurately at co-ordinate (0,0,0) and the same source located at (0,0,0.1) (dimensions quoted in cm). In this example the source is parallel to the Z axis. The figure shows that a 1 mm radioactive source displacement means the dose delivered to a point 1 cm from the source at (1,0,0) – yellow dot in figure – is only about 1% different, but at the location (1,0,1) – blue dot – almost 12% more than the expected dose is delivered. Three centimetres from the source in any direction, the dose error is around ±4%. For a +2 mm needle-tip definition error, the dose difference is about 5% at (0,1,0), and nearly 25% at (1,0,1). This amount of difference may have implications for patient treatment if, for example, a significantly higher than planned dose is delivered to an organ at risk such as the urethra or rectum.

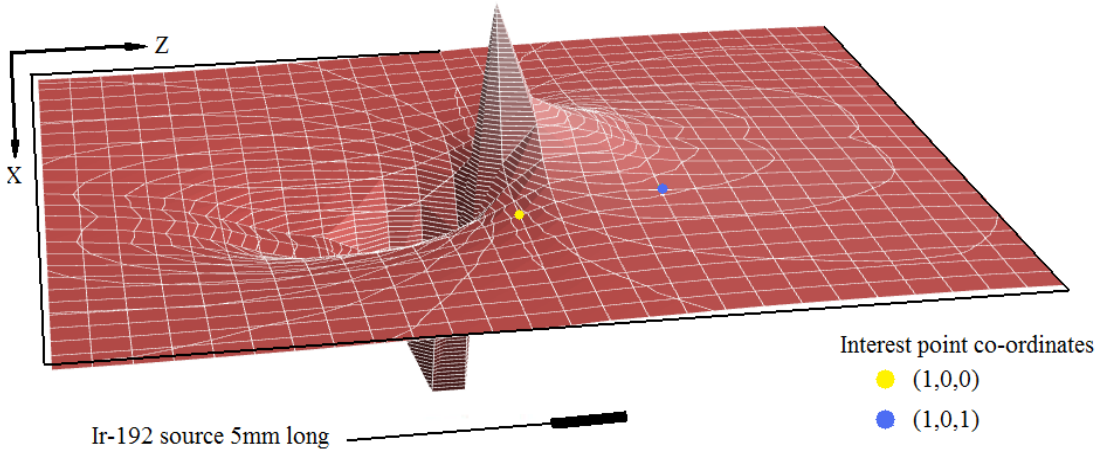

Figure 3-2: Dose difference (%) from expected dose in X-Z plane for +1 mm source position error (i.e. to the right). Grid squares are 2.5 x 2.5 mm, contour spacing = 2%. Peak is at new source centre. Underdose truncated to -100%. Source lies in the *X*-*Z* plane, along *Z* axis.

Thus, 'clinically useful' images for HDR brachytherapy will ideally provide:

- Accurate visualisation of implanted HDR brachytherapy needles, with no loss of detail particularly at the needle tips.
- In the case of fractionated HDR treatment, clear visualisation of implanted fiducial markers for prostate and needle localisation at each fraction.
- Distortionless images for accurate volume definition and accurate needle separation, ensuring accurate dose calculation.
- Clear detail of prostate anatomy – at least, sufficient detail to enable accurate definition of the target volume for radiotherapy treatment planning.

In the discussion that follows, some general aspects of medical greyscale imaging are described, with particular reference to digital image manipulation to optimise visualisation of objects of interest.

3.2 The human eye and medical grey-scale images.

The human eye can resolve features as small as 60 cpd (cycles per degree). At 0.5m, the distance at which many will observe a computer's visual display, this equates to objects only 0.15 mm wide (Barten, 1999). Whether this level of detail will actually be observed depends upon viewing conditions: brightness (luminance) of the surrounding environment, amount of contrast between adjacent objects (contrast ratio), and the individual observer. Figure 3-3 plots the eye's modulation transfer function for a range of pupil diameters, and shows why diagnostic images are better observed in a dark room:

Figure 3-3: Modulation transfer function of human eye for different pupil diameters (from Prof B Girod, http://www.stanford.edu/class/ee368b/Handouts/09-HumanPerception.pdf).

The human eye can better-resolve objects with low contrast resolution when the pupil is wide – in a dim environment the eye can admit more light and contrast differences between adjacent objects don't need to be as great to separate them. By reducing light in the local environment, the contrast sensitivity at the small-scale end is improved. Typically, the eye is most sensitive to objects in the 0.2-10 cpd size range. At 50 cm, this corresponds to objects with dimensions from 45 mm down to about 0.8 mm.

All of the CT, MR, TRUS and fluoroscopic images discussed in this work were displayed as grey-scale images. Imaging modalities typically deliver images as 12-bit (4096 shades of grey), or 16-bit data (65536 shades). However, HDR brachytherapy treatment planning systems are often supplied with a computer monitor that uses only 8-bit RGB (Red-Green-Blue) to generate colours, and shades of grey equate to equal proportions of each colour. There can be 256x256x256 = 16.7 million different colours, but only 256 shades of grey from (0,0,0) = black, to (255,255,255) = white. Already, patient images are degraded as the 12-bit or 16-bit data are truncated to 8 bits for display on the computer monitor. Demand for better than 8 bit grey-scale is limited, so that specialist 10 or 12 bit grey-scale monitors and associated video processors are presently comparatively expensive.

3.2.1 DICOM (Digital Imaging & Communications in Medicine) standard.

Loss of image detail and contrast resolution due to data truncation only partly explains why images may appear less good on some monitors than others. Most monitors have an inherent 'colour bias' wherein not all tones are displayed with the same luminance. Received image data are processed via a look-up table (LUT) to correct the colour bias. As discussed, human perception of greyscale is better in a darker environment, but the eye adapts to the local environment, making implementation of a universal LUT table very difficult. The DICOM medical imaging standard (NEMA, 2004) is a widely accepted LUT. Figure 3-4 shows the DICOM greyscale standard display function (GSDF – red curve), a LUT that defines a continuous grey scale and corresponding luminance levels.

Figure 3-4: DICOM greyscale standard display function – GSDF (red continuous curve) compared with an 8-bit approximation (blue stepwise curve), NEMA (2004).

The DICOM GSDF is based upon Barten's model of the human visual system's contrast sensitivity (Barten, 1992), which is non-linear in the GDSF luminance range. Between two adjacent shades of grey on the GSDF curve, the corresponding luminance levels give the same impression of a 'just noticeable difference' (JND) in contrast. The DICOM curve is 'perceptually linearised', so the same JND at any luminance provides the same perceived contrast difference. Applying the GSDF at all interfaces in an imaging chain should enable image reproduction with the same impression of contrast on any monitor. However, as

shown in Figure 3-4, the truncation of grey-scale data from 12-bit to 8-bit can introduce as much as 10% deviation from the ideal GSDF function (Matthijs, 2003).

8-bit or 10-bit. Shades of grey on a 10-bit scale are divided into 1024 bins from black to white, while an 8-bit scale divides the greyscale into only 256 bins. In 10-bit CT images, each bin would represent a CT number range of about 40 HU, compared with 160 HU in an 8-bit greyscale. The loss of contrast resolution affects contrast as shown in figure 3-5.

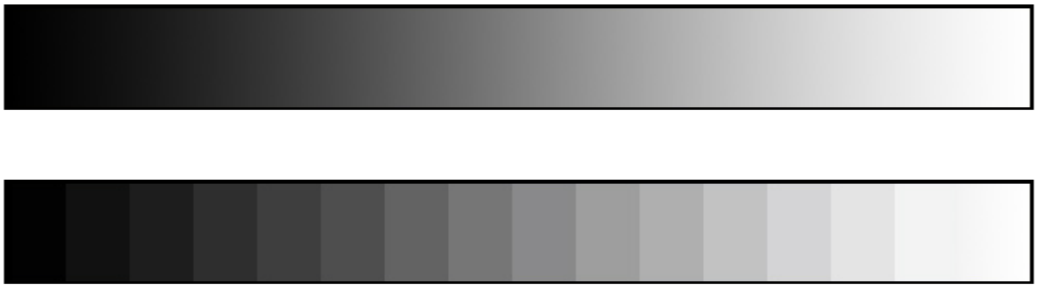

Figure 3-5: Representative contrast resolution in 10-bit (top) and 8-bit greyscale binning.

Unfortunately, most HDR brachytherapy treatment planning systems use 8-bit greyscale displays, and clearly delineated features on a 10-bit grey-scale monitor attached to an MR or CT scanner may be poorly defined or even lost when displayed for HDR brachytherapy treatment planning 8-bit monitors.

LCD or CRT. A survey of the advantages and disadvantages of LCD and CRT monitors was provided by Sorantin (2008). According to the American College of Radiology (ACR, 2008), cathode ray tube (CRT) or liquid crystal display (LCD) monitors are equally good, so long as the monitor complies with relevant performance and acceptance testing procedures such as the AAPM's published guidelines (Samei *et al.*, 2005). The guidelines specify a series of simple and advanced tests to be executed periodically with reference images to ensure ongoing compliance with recommended standards.

3.2.2 Contrast enhancement – windowing and levelling.

Despite the loss of contrast resolution imposed by 8-bit display, digital imaging offers a significant advantage over film: image brightness and contrast can be altered without re-imaging the patient. The full greyscale range can be 'windowed' to cover a smaller portion of the range, centred on a particular value or 'level' *L*.

NOTE:
This figure is included on page 22 of the print copy of the thesis held in the University of Adelaide Library.

Figure 3-6: Effect of different CT window and level settings on the contrast resolution of CT images. A narrow window gives high contrast. Points with CT number > P2 will appear white, below P1 will appear black (from Bushberg *et al* 2nd *ed* p359).

Figure 3-6 shows this feature for CT Hounsfield numbers, where optimum contrast for an object of interest is achieved when the level *L* is set to the object's average CT number. For a window of width *W,* CT numbers less than P_1 are saturated to black, and above P_2 are saturated to white. A narrow window should be used when objects are of similar density, since fewer HU can be assigned to each greyscale increment, providing more contrast.

Selecting levels and windows. In HDR brachytherapy images the implanted needles, marker seeds, and the target volume of soft tissue must be identified. In CT images they can be separated by their CT number ranges, that characterise each material's electron density. Gold seeds typically have CT numbers around 13000 ± 5000 HU, stainless steel needles 3700 ± 1700 HU, and prostate tissue lies close to 40 ± 40 HU. Figure 3-7 shows a transverse CT image slice from an HDR brachytherapy implant as it appears with default window and level settings in figure 3-7(a), and in figure 3-7(b) the window and level are set to 3700 ± 1700 HU to emphasise implanted steel needles. Note the two large whiter spots that correspond to implanted gold fiducial markers.

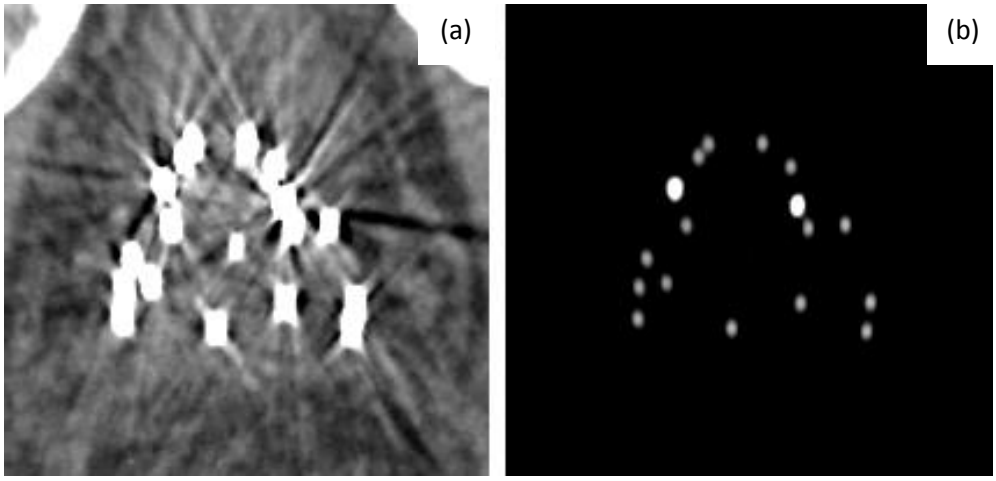

Figure 3-7: Transverse CT image of implanted stainless steel needles and gold fiducial markers near prostate base (a) default window and level (b) level and window set to 3700 ± 1700 HU. Note improved discrimination between needles.

As shown in figure 3-7(b), adjusting a CT level window to match the expected CT number of implanted needles improves their visibility and our ability to separate adjacent needles. Note the clearly identifiable gold fiducial markers in figure 3-7(b) that were difficult to separate from needles in figure 3-7(a). Conversely, soft tissue detail observed in figure 3-7(a) is lost in figure 3-7(b); a level and window adjustment will re-instate soft tissue detail.

3.3 Imaging modalities and clinically useful image acquisition.

The challenges often encountered in each imaging modality when used for prostate HDR brachytherapy treatment planning image acquisition are numerous. Some, such as partial volume averaging due to finite pixel area or voxel volume are common to all modalities, but can be more significant in ultrasound or MR imaging when compared with CT or fluoroscopy for example. Other artifacts may be unique to the particular modality, for example reflections from side lobes in ultrasound imaging or susceptibility artifact and distortion in MR imaging. The challenges for each modality when imaging the prostate and implanted HDR brachytherapy needles in the presence of bilateral hip prostheses will be demonstrated and discussed below. Image artifacts and effects that have the most significant impact in each modality will then be examined in more detail.

3.3.1 Fluoroscopy.

'C-arm' fluoroscopy typically uses a 90-100 keV x-ray source for real-time visualisation of bony anatomy and high-density materials such as hip prostheses and implanted needles in HDR brachytherapy treatments. A disadvantage of fluoroscopic imaging is the time-dependent radiation exposure of patient and staff, and the need for protective shields and/or clothing. Another disadvantage, aside from two-dimensional images, pincushion and sigmoidal image distortions, is the comparative lack of soft-tissue detail – the prostate itself cannot be seen. Implanted radio-opaque markers are needed to indicate its location, and three or four small gold or silver 'seeds' are usually implanted under TRUS guidance during HDR brachytherapy needle implantation to identify the prostate base and apex.

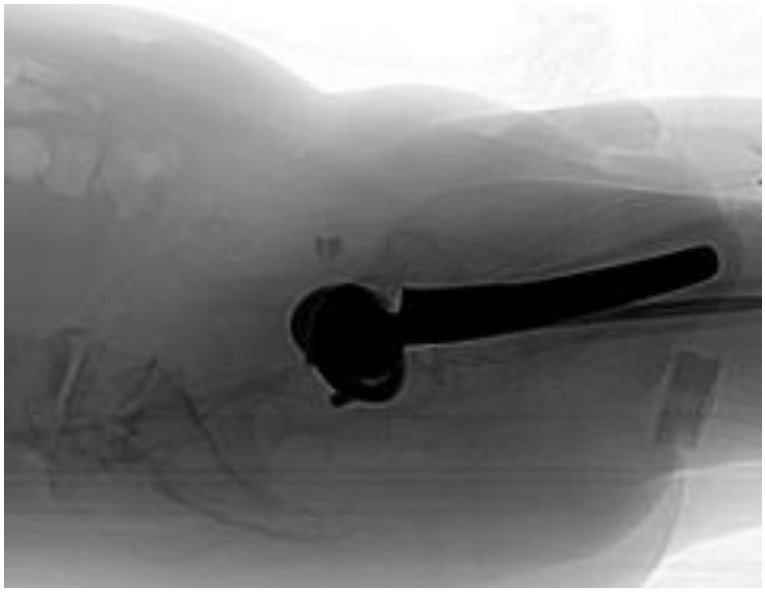

Figure 3-8: Sagittal fluoroscopic x-ray image of implanted plastic needles in bilateral hip prosthesis patient. Note needle template on perineum, needle tips obscured by prosthesis.

Fluoroscopy guides needle insertion during the implant, and coronal images of the implanted prostate markers and needles are used for localisation and verification of patient set-up at each treatment fraction, and to check for needle displacement relative to implanted markers. If necessary, corrective action can be taken prior to radiation delivery (Tiong *et al.*, 2009), to be discussed in more detail in Chapter 5. Figure 3-1 showed a coronal AP image from a prosthesis patient. Implanted steel needles could be easily identified. In contrast, plastic needles may be difficult to identify without metal obturators, and the lateral view can be completely obscured by the implanted prostheses as shown in figure 3-8.

3.3.2 Ultrasound.

Ultrasound is a widely available and comparatively inexpensive real-time imaging modality that provides edge-enhanced images of major tissues and structures (Carson 2009) with good spatial resolution and no known long-term side effects. Ultrasound images are based upon the physical properties of ultrasound pulse formation, the propagation of sound in matter and its interaction with interfaces and materials, and echo detection and processing. The physics of ultrasound is discussed in Appendix 2.1.

Recent work has focussed upon detail contained within the backscattered signal that may enable reliable tumour detection (Pallwein *et al.*, 2008b). For example, contrast-enhanced colour Doppler imaging enables visualisation of prostate blood flow, which is increased in areas of tumour, and thus potentially allows better-targeted biopsies (Mitterberger *et al.*, 2007). Ultrasound elastography or strain imaging uses the increased density of tumour tissue relative to normal tissue to map differences in compression response, to identify for biopsy areas with increased tumour probability (Pallwein *et al.*, 2008a).

Conventional B-mode grey-scale images, such as those used routinely for image guidance in brachytherapy procedures, do not always enable tumour detection due in part to the heterogeneity of the prostate itself, and tumour tissue can be iso-echoic with normal prostate tissue, confounding detection. Usually, prostate tumour is hypo-echoic (appears darker) in B-mode images, but other tissue such as blood vessels and liquid-filled cysts can also appear darker than normal prostate tissue. With modern trans-rectal transducers three-dimensional images of the prostate can be obtained, but imaging is usually limited to either transverse or longitudinal planes, with the operator switching planes as required.

Challenges in ultrasound image acquisition.

No imaging modality is free of complications, challenges, and potential artifacts that affect image utility, and ultrasound is no exception. The most significant disadvantage of U/S for HDR brachytherapy is hyper-echoicity of the implanted needles that reduces image quality, particularly for anatomy and implanted needles anterior to other needles. Another disadvantage is that visualisation of objects above gas can be very poor, and this can be troublesome for TRUS in patients with poor bowel preparation.

In clinical sonography the assumptions at the basis of image formation may not be upheld, leading to inaccurate data display, or artifact. Sources of ultrasound artifacts are many and varied – some are due to differences in acoustic impedance between adjacent objects, or to signals originating from secondary side lobes (unavoidable in ultrasound transducers), and are due to the refraction and reflection of acoustic waves. Multiple echo paths, velocity, and attenuation variations all may cause image artifact. As well, the high frequency (MHz) electrical signals that drive signal propagation, reception, and subsequent signal processing are sensitive to electrical interference that degrades image quality. Artifacts encountered in HDR prostate brachytherapy imaging include:

Shadowing and enhancement. The amplification of ultrasound signal is typically made time dependent, so that signals received later that have travelled further and are more attenuated, are amplified more. The manufacturer's default gain-versus time curve assumes constant attenuation with depth (i.e. uniform acoustic impedance) but clinically this assumption is rarely valid. The ultrasound image behind a strongly attenuating or highly reflecting object appears dark (shadowing) and typically also displays poor contrast, limiting the utility of the image for diagnostic purposes.

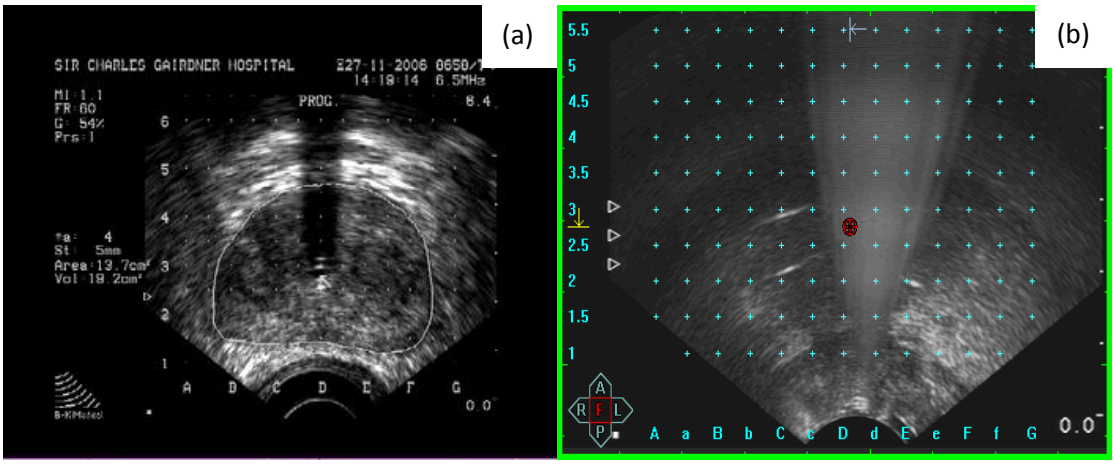

Figure 3-9: (a) Shadowing from urethral catheter at column *D*, row 3. Bright flashes correspond to catheter walls. (b) Shadowing due to gas in rectum. Fan-shaped hyper echoic area possibly originating from calcification between columns *D* and *d* near the rectal wall.

Figure 3-9(a) illustrates typical shadowing artifact from a Foley catheter in the urethra. Use of micro-bubble contrast agents or aerated gel in the catheter causes shadowing artifact anterior of the urethra in TRUS images as shown. However, brachytherapy needles are rarely implanted anterior of the catheter (i.e. in column *D* anterior of the catheter) due to

the risk of penetrating the urethra inferior of the apex, or the bladder neck (or both). Figure 3-9(b) shows a typical fan-shaped hyper-echoic segment originating from close to the rectal wall, possibly from a calcification. Unfortunately, rectal gas close to the transducer surface is highly reflective and causes troublesome shadowing artifact. Even a small amount can cause shadow artifact over a wide sector in a fan-beam image. A trans-rectal transducer may need to be removed and re-inserted to eliminate rectal gas and restore adequate image quality for volume study or needle implant guidance.

Reverberation artifact. Multiple echoes may be generated between closely-spaced highly reflective interfaces, such as the walls of steel brachytherapy needles, as shown in figure 3-10(a) and 3-10(b). Echoes from each needle are observed as multiple equally-spaced boundaries with decreasing brightness as radial distance from the transducer increases. Fortunately, the needles are highly reflective and are very bright in TRUS images, and for posterior needles the reverberation and shadowing artifacts are not troublesome. However, anterior needles and the anterior prostate border may be difficult to identify.

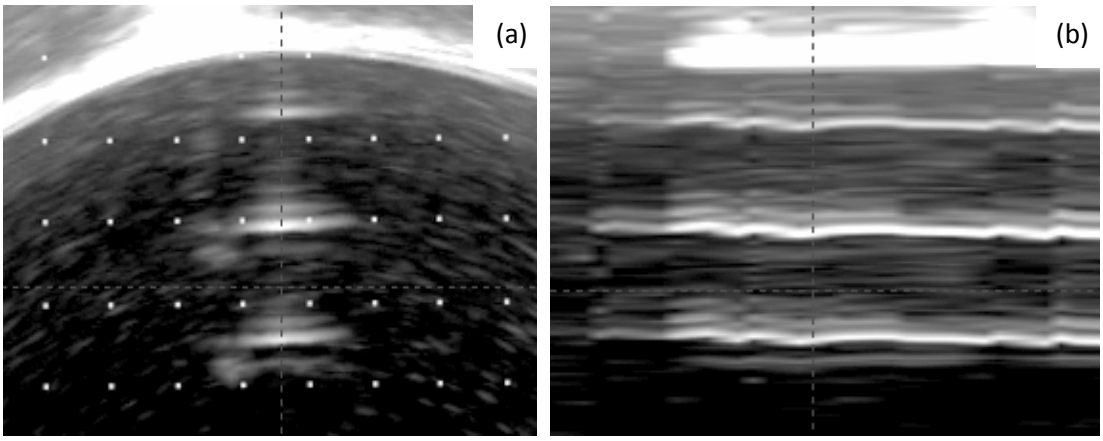

Figure 3-10: (a) Transverse view containing reverberation artifact from three steel needles in a water phantom (b) Longitudinal view of reverberation artifact from same needles. Topmost artefact is due to reflection from water surface. Transducer is at bottom of figures.

Needle identification errors. Implanted needles may not be driven to the desired location with a single insertion (Wan *et al.*, 2005), and steering techniques (unique to each urologist) may be used to achieve the desired location. Multiple insertions may be required, for example if calcifications lie in the desired path, or pelvic arch interference is encountered. The final needle location may be accompanied by several empty needle tracks fanning from a single insertion point, and tissue interfaces created by the needle

tracks may be visible as hypo-echoic (dark) lines. While not usually problematic with stainless steel needles, it can be difficult to distinguish empty tracks from plastic needles.

Speed (velocity) displacement. U/S processing software must assume a constant speed of sound in the body being scanned. However, the speed of sound in fat (for example) is about 6% slower than the speed of sound in prostate tissue. The fat layer between rectum and prostate will therefore cause an outward displacement of the prostate and implanted needle image by about 6% of the thickness of the fat layer. In all but a few patients this velocity displacement will be less than 0.5 mm, and can be ignored.

3.3.3 Magnetic Resonance Imaging.

Magnetic resonance imaging is an emission imaging technique operating in the non-ionising radiofrequency (RF) range of the electromagnetic spectrum, making it an attractive technique for imaging radiation-sensitive tissue such as the spinal cord and brain. Another significant attraction is the ability to manipulate image contrast by adjusting a range of parameters that alter the type and quality of information provided. Advantages for prostate imaging include high soft-tissue contrast, good spatial resolution, and a variety of imaging options via manipulation of T1 and T2 weighting parameters. Spatial encoding of MR signals yields spatial resolution of 0.5-1.0 mm in the transverse plane, but typically only 2-10 mm axial (slice thickness) resolution. It is believed that MR scans have no deleterious effects upon humans (Chakeres and de Vocht, 2005; Hartwig *et al.*, 2009), however recent work (Schlamann *et al.*, 2009) has shown there may be a measurable but short term effect upon cortical activity including motor responses. The ability of MR to provide excellent soft-tissue delineation has seen it become an established diagnostic and research tool in many areas of medicine. A recent publication (Webb, 2006) discussed more than 50 different applications in medical and pharmaceutical sciences, and listed more than 150 papers describing applications in chemistry, biology, and materials science.

MR exploits the magnetic properties of materials, and image contrast is derived from differences in material response to an applied RF signal in a constant external field. However, large magnetic susceptibility differences between objects in the field can cause significant artifact and unfortunately, ferromagnetic metals such as iron, cobalt, and nickel are common in hip prostheses. An endorectal coil with phased array pelvic coils can significantly improve prostate cancer images (Mullerad *et al.*, 2005; Futterer *et al.*, 2007).

MR imaging has provided new data (Turkbey *et al.*, 2009) and detail on prostate cancer but is not common for HDR treatment planning, due primarily to a lack of compatible HDR brachytherapy hardware (Atalar and Menard, 2005; Muntener *et al.*, 2008). Figure 3-11(a) shows a T2-weighted transverse image through the prostate and implanted needles in a non-prosthesis patient, obtained with an endorectal MR coil.

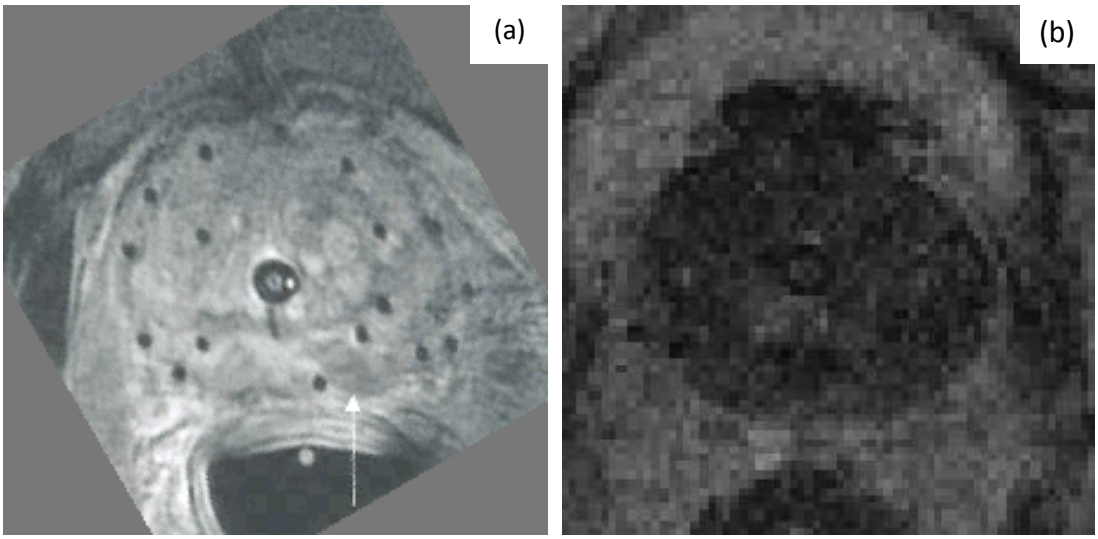

Figure 3-11: (a) Adapted from Menard *et al* 2004. T2 endorectal coil MR image in patient with natural hips. Prostate and implanted needles are well defined. (b) SCGH transverse T2 MR image in patient with bilateral prosthetic hips; poorly-visualised prostate and implanted needles not detectable. Note reduced spatial resolution and reduced contrast resolution.

At SCGH an endorectal coil was not available, and figure 3-11(b) shows a typical MR image (T2 TSE, TR 1170 msec, TE 12 msec, slice 3.0 mm) obtained with a 1.5 T Siemens Sonata MR scanner, from a patient with bilateral hip replacements. The challenge of obtaining suitable images without an endorectal coil is made clear with this comparison.

MRI in radiotherapy.

MR imaging for radiotherapy is used primarily for anatomic information, dynamic contrast enhancement of tumours, or diagnostic MR spectroscopy in the brain, breast, and prostate (Jacobs *et al.*, 2007). However compared with CT, MR for treatment planning can suffer greater geometric image distortion and artifact due to intrinsic and object-induced magnetic field effects. Importantly, MR data represent proton density and nuclear spin relaxation times which cannot be simply converted into electron density data required for EBRT dose calculations. In EBRT treatment planning, use of uniform electron density can

lead to 2-5% inaccuracies in predicted dose (Chen *et al.*, 2004; Wang *et al.*, 2008a). If necessary, electron density information can be obtained from co-registered CT data.

Challenges in MR image acquisition.

An image dataset for prostate HDR brachytherapy treatment planning must enable accurate identification of distal needle tips. The target volume should be clearly identifiable, but fiducial markers and a detailed TRUS volume study may lessen this requirement. MR imaging relies upon 2D Fourier transformation of *k*-space data (theoretical aspects of MR are discussed in Appendix 2.2) and disruption or data corruption in *k*-space leads to artifact in reconstructed images. Cross-talk, aliasing, herringbone and zip artifact, ghosting, and many others, are well documented and can affect any MR image (Porter *et al.*, 1987; Zhuo and Gullapalli, 2006). Potential sources of artifact in MR imaging are numerous (more so than in CT) and only a selection that may compromise accurate identification of the target and distal needle tips in patients with bilateral hip prostheses are discussed below:

Patient motion. Image blur and ghosting in the phase encoding direction are common artifacts of patient motion. Periodic movements cause coherent ghosts, and random motions cause blur. The acquisition of adjacent points in the frequency encoding direction occurs within a few microseconds and artifact in this direction is not usually severe, but in the phase encoding direction the time between adjacent points is the repetition time TR, and artifact can be significant. Unfortunately 1.5 T MR scans of an HDR prostate brachytherapy implant can take 15 minutes or longer, during which time the patient must remain motionless. For many, particularly the recipients of a trans-perineal prostate brachytherapy implant, this can be very challenging.

Gibbs ringing. Bright or dark lines parallel and next to abrupt signal intensity changes in MR images are due to under-sampling of high spatial frequencies (abrupt changes in material properties such as those due to the presence of a metal prosthesis) in either the phase or frequency encoding direction. Ringing can be reduced by using smaller pixel size (reduced field of view – FOV – or increased acquisition matrix dimension) but at the expense of increased acquisition time and reduced signal-to-noise ratio. Mathematical techniques such as Gegenbauer reconstruction (Huang and Chen, 2005) can also be used.

Flow artifact. In gradient recalled echo (GRE) sequences, flow produces a 'bright blood' phenomenon. In spin-echo (SE) sequences blood appears dark in the phase encoding (*y*) direction because flowing blood exposed to a 90° RF excitation pulse moved out of the imaging section before a refocusing 180° RF pulse was applied, and blood moving into the section was not exposed to the excitation pulse (Larson *et al.*, 1990). In spin-echo images of HDR prostate brachytherapy implants, the implanted needles appear as small dark spots on transverse slices and may be confused with vasculature. A saturation band (in which repeated application of RF pulses makes the net magnetisation zero) adjacent to the imaging section can reduce flow artifact. Gradient moment nulling (Ehman and Felmlee, 1990), where motion-compensating gradient pulses ensure that flowing spins with constant velocity are brought back into phase, with no effect on static spins, may be beneficial.

Gradient-related distortion. Gradient fields are non-linear away from the MR scanner isocentre, and large FOV images may be compressed and distorted at the edges, as shown in figure 3-12(a). Distortion may be particularly evident in the coronal and saggital directions, and may be problematic in EBRT treatment planning (Fransson *et al.*, 2001).

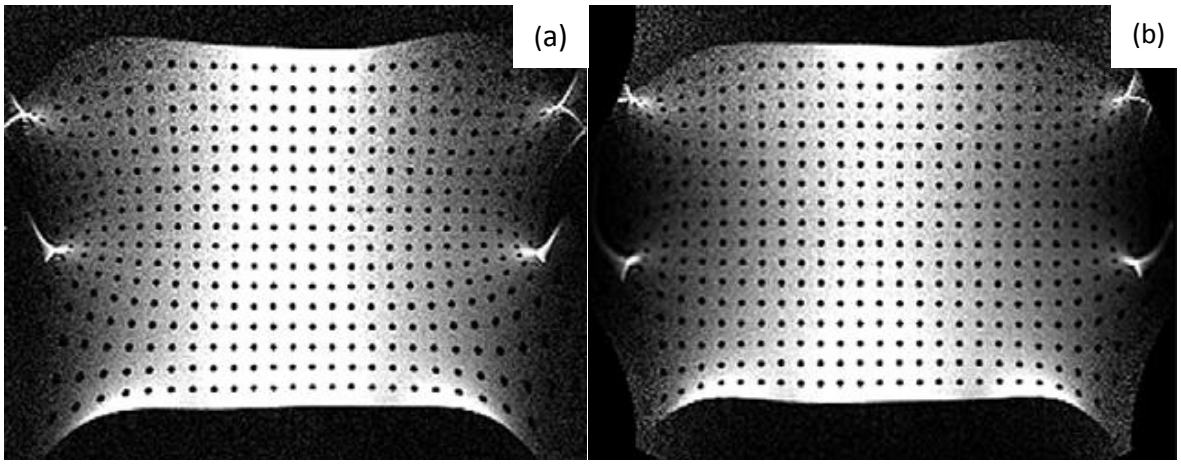

Figure 3-12: Geometric distortion of a uniform grid phantom due to gradient field non-linearity (a) before and (b) after correction (Fransson *et al* 2001).

Usually, manufacturer-supplied correction algorithms are used to compensate gradient field nonlinearities – figure 3-12(b). For HDR brachytherapy, the region of interest is usually close to the grid centre, and geometric distortion should not be problematic.

Radiofrequency (RF) heating. MR-induced heating is a known risk with implanted conductive devices such as the non-magnetic stainless steel or titanium needles used in HDR prostate brachytherapy (Yeung *et al* 2007). The needle can act as an antenna for RF

energy generated in the MR scan, or can act as a conductor of eddy currents induced in the body (Helfer *et al* 2006). While the needle temperature may not increase (Armenian *et al* 2004), resistive heating in tissues near the needle tip may cause damage-inducing temperature increases. Mattei *et al* (2008) presented a comprehensive investigation of RF heating effects, and van den Bosch *et al* (2010) specifically discussed titanium brachytherapy needles. Generally, deeper insertion of a conductive needle further from the central axis of an MR scanner leads to greater temperature increases. Ratnayaka *et al* (2010) discussed specialised marker wires to reduce RF heating, while Mattei *et al* found that an insulating sheath does not eliminate heating, suggesting metal marker wires within plastic needles may also cause tissue heating. In prostate HDR brachytherapy the needle tip is ideally not within the target volume, and tissue heating (hypothermia) is therefore undesirable.

Partial volume effects. As discussed, partial volume effects may affect accurate distal needle tip identification, increasing treatment dose uncertainty (Kim *et al.*, 2004). The relaxation time attributed to an MR voxel is the average relaxation time of the materials contained within it, and partial volume averaging can have a significant effect upon the apparent distal needle tip location. Partial volume averaging can be reduced by using the smallest acceptable FOV that contains the target and implanted needles with sufficient margin. Increased transverse spatial resolution (more samples in the phase encode direction, and increased sampling rate and/or increased gradient in the frequency encode direction), and thin slices (narrow slice-select bandwidth or increased gradient) will reduce partial volume effects, but at the expense of signal-to-noise ratio (Carmi *et al.*, 2006).

Susceptibility. The magnetic susceptibility of an object determines its magnetization in a static magnetic field, and the object's magnetization then alters the local field. Ferromagnetic objects thus cause more artifact than paramagnetic or diamagnetic objects. Susceptibility artifact may cause areas of complete signal loss as the local magnetic field is strong enough that spins are immediately de-phased, as shown in figure 3-13.

Susceptibility artifact is most difficult to avoid and potentially has greatest impact upon imaging for HDR prostate brachytherapy. When inserted into the magnetic field of an MR scanner, ferromagnetic materials in particular induce their own magnetic field and can sufficiently alter the precession frequencies of protons in nearby tissues that they do not generate useful signal.

NOTE:
This figure is included on page 33 of the print copy of the thesis held in the University of Adelaide Library.

Figure 3-13: Metal artifact depends upon material type and dimensions (a) sample with titanium alloy and stainless steel screws. Axial images obtained with (b) GRE and (c) FSE sequence. Arrow in (b) shows frequency encoding direction (adapted from Lee *et al* 2007).

As discussed in Chapter 2, the principal metals used in hip prostheses are titanium alloys, stainless steel, and alloys of cobalt and chromium. Titanium alloys are less ferromagnetic than both cobalt-chrome and stainless steel, and induce less susceptibility artifact and less image degradation (Shellock and Kanal, 1998). Artifact from metal can have varied appearance on MR scans depending upon the type of metal or its spatial orientation with respect to the field direction, but three main features can be identified:

- The magnetic moment of the object itself is poorly defined and may lead to a local signal void, often accompanied by an area of high signal intensity and modification of local gradient fields that leads to image distortion. (Eustace *et al.*, 1997).
- When the local magnetic field is disrupted, so too is the Larmor frequency of protons in the metal object and in the local surroundings. This leads to spatial mis-registration in the frequency encoding direction after the 2D Fourier reconstruction process (i.e. spatial distortion). Wide bandwidth can be beneficial, as it requires the use of stronger frequency encoding gradients, which proportionally reduces mis-registration artifacts. GRE sequences are affected more than SE or TSE sequences (Port and Pomper, 2000).
- The magnetic field gradient is steep near the edge of metal objects, and intra-voxel phase dispersion and dephasing leads to signal void near the object. Neither GRE nor SE sequences can correct the effect (Eustace *et al.*, 1997; Port and Pomper, 2000). Reduced voxel size can reduce diffusion-related signal intensity losses, and reduce the apparent size of the signal void (White *et al.*, 2000).

Field heterogeneities at tissue boundaries cause spins to de-phase more rapidly, reducing the signal intensity and causing geometric distortion, particularly in images formed by T1-weighted sequences with long echo times TE, or by GRE sequences (Czervionke *et al.*, 1988). Use of a spin-echo sequence (less affected by local field variation as the 180° refocusing pulse cancels susceptibility gradients), using gradient shims to optimise local field homogeneity, aligning the phase encoding and susceptibility gradients, or reducing the echo time TE and increasing the acquisition matrix size may reduce susceptibility artifact (Kaur *et al.*, 2007).

View angle tilting (Cho *et al.*, 1988) with fast spin-echo sequences was shown to reduce metal artifact by more than 60%, but at the expense of image blur, particularly in the *z* direction. Modified versions of view angle tilting, such as MARS (Kolind *et al.*, 2004), used increased slice-select and image bandwidths (i.e. thicker slices with reduced spatial resolution) to reduce artefact by almost 80%. Specialised pulse sequences such as SEMAC (Lu *et al.*, 2009) can reduce the blur inherent in view angle tilted images.

Different scanning techniques and sequences affect the magnitude and appearance of metal artifact. Local field inhomogeneities are reduced by SE or TSE sequences as the 180° phase reversing pulse reduces the impact of spin dispersion and dephasing. As well, the multiple echoes in a TSE sequence mean the true echo time is short compared with the effective time TE, allowing less time for dephasing (Tartaglino *et al.*, 1994). Similarly, a short overall echo time TE reduces signal loss due to intravoxel dephasing. Setting the long axis of a metal object parallel with the main field direction reduces the amount of artifact – the long axis of a hip prosthesis stem aligns naturally with the bore of an MR scanner, and responds better to sequence refinements than the obliquely-oriented neck, or the acetabulum. Unfortunately, the prostate and distal needle tips are often in line with the acetabulum. Metal artifact is more pronounced in the frequency encoding direction due to proton spin dephasing (Sofka and Potter, 2002), but changing the frequency encoding direction may shift artifact away from regions of interest.

Conventional MR imaging requires tens of milliseconds for signal acquisition following each excitation pulse, and hence fails to image solid materials because their T2 times are typically of the order of fractions of milliseconds. For example, the T2* relaxation times of PMMA materials such as those used in the acetabular cups of hip prostheses are typically of the order of 20 μsec (Horch *et al.*, 2010). Some (Ramos-Cabrer *et al.*, 2004) have

investigated a single point imaging technique (SPI) that is capable of measuring such short relaxation times, and is reportedly largely immune from susceptibility artifact. In SPI only one point of the free induction decay is acquired after each excitation, making it insensitive to distortions arising from signal intensity variation during the acquisition of multiple *k*-space data points. However, it uses point-by-point data acquisition to fill *k*-space, and can be slow. Large gradient amplitudes and rapid switching are required to obtain images with high spectral and spatial resolution, and the necessary delays that are included to maintain thermal stability (and gradient stability) mean overall imaging times can be very long.

3.3.4 Computed Tomography.

CT is the standard imaging technique for HDR brachytherapy treatment planning. Typically, images are acquired after a patient leaves theatre and is sufficiently recovered from anaesthesia. CT image contrast is produced primarily by Compton interactions and thus provides a direct measure of tissue density. This feature dramatically changed treatment planning for EBRT (Sontag and Cunningham, 1978; Jelden *et al.*, 1976a), as it enabled computational algorithms to include tissue heterogeneity when calculating dose deposition into a patient. Inclusion of CT number information in dosimetry calculations has only recently been included in HDR brachytherapy treatment planning systems. Prostate CT scans typically use a 120-140 keV x-ray source for good soft tissue contrast with good spatial resolution, minimal distortion and clinically useful image quality. The prostate can be discerned from adjacent tissues, and implanted needles and markers can be detected for treatment planning. However, figure 3-14 shows typical CT data from a bilateral hip prosthesis (Charnley *et al.*, 2005) at the time this work commenced.

Figure 3-14: circa-2005 mid-prostate transverse CT slice from patient with bilateral hip prostheses. Note signal deficit due to prostheses; prostate is not visible (Charnley *et al* 2005).

Unfortunately, high-density objects such as metal prostheses remove low-energy components of the x-ray beam and cause significant signal deficit, evident as dark and bright streaks. Typically, visualisation of the prostate, rectum, or bladder was limited.

Current CT scanners are typically multi-slice high spatial resolution tomographic x-ray devices that provide good detail for image-based medical decision-making (Pan *et al.*, 2008). Commercially available 64-slice CT scanners can obtain data simultaneously from a 40 mm-thick transverse section, with 0.625 mm section thickness in the longitudinal direction (*z*-axis). In the transverse (axial or azimuthal) plane spatial resolution is determined by pixel size in the image data array. For example if a 512x512 matrix is used with a field of view (FOV) of 25 cm, sufficient to encompass an HDR prostate brachytherapy implant, pixels in the axial image are about 0.5 mm square. Increasing the FOV to 50cm to include the hips increases pixels to 0.8 mm square.

CT in radiotherapy.

The benefits of CT body contour and anatomical data for radiotherapy treatment planning were described more than a generation ago (Chernak *et al.*, 1975; Jelden *et al.*, 1976b; Sontag *et al.*, 1977; Sontag and Cunningham, 1978). As well as providing good anatomical detail, the observed CT number in each volume element (voxel) is directly related to the x-ray linear attenuation coefficient (LAC) of material contained within it. Thus, the radiation dose deposited into a voxel can be calculated, enabling accurate determination of dose to targets and organs at risk. Until recently, CT number data were ignored in most HDR brachytherapy dose calculators, but could be used in the EBRT phase of combined treatments (Mohan *et al.*, 1981; Evans, 2008). Algorithms that ignore tissue heterogeneity, for example by setting the LAC of prostheses to that of water, tend to overestimate dose delivered distal from a prosthesis, as will commercial EBRT pencil beam or superposition algorithms (Keall *et al.*, 2003; Reft *et al.*, 2003). CT number data itself may be inaccurate unless an extended scale is applied (Coolens and Childs, 2003).

Challenges in CT image acquisition.

CT artifact is any systematic difference between observed CT numbers in a reconstructed image and true attenuation coefficients in the object. The CT reconstruction process (discussed in Appendix 2.3) assumes that each measurement is consistent, and differences

in recorded signal intensity are due only to attenuation of the projected x-ray beam in the object. As a typical CT image is reconstructed from around 1 million individual line projections recorded by hundreds of individual detectors, the potential for artifact is high.

CT artifacts are well documented (Barrett and Keat, 2004). Features such as ring artifact due to poor detector calibration, or aliasing due to under-sampling of projections, may be observed in images of any patient, but usually can be avoided with due care. As discussed earlier, the key requirement for prostate HDR brachytherapy treatment planning is the ability to accurately identify distal needle tips. The target should also be clearly identifiable, but this may be of lesser importance if surrogate markers were implanted and a TRUS volume study was acquired. For patients with bilateral hip prostheses, three unavoidable artifacts may compromise accurate target and distal needle tip identification:

Beam hardening. The incident CT x-ray beam is polychromatic, and preferentially loses the lower-energy portion as it passes through objects. The projected x-ray beam has reduced intensity at the detector (and therefore is less well separated from noise) but higher average energy than the incident beam. Beam hardening means the effective LAC of any object diminishes as the beam travels further into it, making short projection paths proportionally more attenuating than long paths. This may cause darkening (reduced CT number) towards the centre of sufficiently attenuating objects due to the longer pathlengths, and brightening near edges. This ‘cupping’ artifact can be reduced by pre-hardening the x-ray beam with a flat or ‘bow-tie’ shaped piece of copper, brass or aluminium (Glover, 1982), at the expense of reduced x-ray intensity at all energies and increased image noise unless longer acquisition times are used. As HDR prostate brachytherapy does not require accurate prosthesis detail, this is not usually problematic. However reduced CT numbers toward the FOV centre, where implanted needles are typically located, may be problematic for needle identification.

Mis-registration, blurring, shading and streaking. This group of artifacts may be due to patient motion during the CT scan. Differences in patient position are likely to be greatest between projections at the start and end of each 360° scan, and various overscanning, signal averaging and weighting procedures (Barrett and Keat, 2004) can be used to reduce patient motion effects. It is standard practice at SCGH to confirm mis-registration artifacts are not apparent before a patient is transferred from the CT couch. In this way, scans may be repeated if needed.

Partial volume averaging. The LAC, and hence CT number attributed to a CT voxel, is the weighted sum of LACs of all materials contained within it. This volume averaging of LACs can affect an observer's ability to accurately identify distal needle tips, increasing dose uncertainty in treatment delivery (Kim *et al.*, 2004). Partial volume averaging can be reduced by using the smallest acceptable FOV that will contain the target and needles with sufficient margins, by using the highest available transverse image resolution (512x512 or 1024x1024 pixels), and by using thin slice widths. To reduce image noise, thick sections can be reconstructed by concatenating several thin sections. Partial volume effects on a larger scale may cause shading and streak artifacts if an off-axis high-LAC object such as a hip prosthesis partly extends into the x-ray beam in some projections and not in others (Barrett and Keat, 2004), but this will tend to affect only the prosthesis image rather than the target region and implanted needles which usually are near the central scan axis.

Streaking and Metal Artifact Reduction (MAR). Streaking can be so pronounced in patients with high-density metal implants that reconstructed images are no longer useful. Streaking can be due to beam hardening and loss of signal as low energy x-rays in the polyenergetic beam are absorbed. It may be due to loss of incident x-ray intensity (photon starvation) distal from a prosthesis, leading to low signal to noise ratio and poor soft tissue detail, or 'over-ranging' when scanning dense prostheses that leads to incomplete attenuation profiles (Barrett and Keat, 2004). Figure 3-14 shows a good example of streak artifact in pelvis images from a patient with bilateral hip replacements. Streaking has the most deleterious effect upon an observer's ability to identify the prostate, and can also make identification of implanted surrogate markers difficult. Even with a comprehensive TRUS volume study dataset and accurate marker identification, the accuracy of patient dosimetry is no longer assured, as the prostate shape may differ between TRUS and CT image acquisition (Seppenwoolde *et al.*, 2008a).

Numerous approaches to reduce artifact from metal implants are proposed, including the use of higher mAs and kVp settings to lessen the impact of photon starvation and beam hardening (at the expense of increased patient dose). Simple but sometimes impractical solutions include using different materials in implanted components, and aligning the long axis of devices with the scanner's z-axis (Stradiotti *et al.*, 2009). Fortunately, the long axis of a prosthetic hip lies naturally along the z-axis in standard pelvic scans. The use of soft tissue reconstruction filters with strong high-frequency roll-off characteristics assists to

reduce streak artifact, at the expense of spatial resolution. An extended CT number scale is also recommended (Link *et al.*, 2000), at the expense of contrast resolution.

Many approaches to artifact reduction aim to improve the ability of image reconstruction algorithms to remove streak artifacts. Some (Hara *et al.*, 2009) have focussed upon iterative reconstruction methods that ignore missing data and reconstruct images using computationally intensive maximum likelihood techniques. Others use techniques such as adaptive filtering in combination with tissue segmentation to interpolate data from nearby areas to replace missing data (Yazdi *et al.*, 2005). As an example of projection interpolation techniques, Mahnken *et al* (2003) described removal of metal objects from a conventionally reconstructed image, forward-projection of data back into the sinogram, then segmentation and replacement of missing signal in raw projection data with estimated data, before conventional filtered back-projection reconstruction of a corrected image, and re-insertion of the metal objects in an adaptive mixing process. However, depending upon the type of filtration applied, this may introduce significant image blur (Liu *et al.*, 2009).

Often, interpolation techniques average data from two points along either rows or columns in the sinogram, but Oehler *et al* (2008) reported that by interpolating data along lines perpendicular to the sinusoidal path of objects in the sinogram, an improved image was reconstructed. The practice of interpolating data from nearest neighbour points to fill in missing data has the disadvantage that sharp edges are smoothed, potentially affecting the perceived quality of filtered images. Unfortunately, many techniques described in the literature are not commercially available – the now widely-used extended CT scale was first reported in 1990 by Klotz *et al*, but was not commercially implemented until nearly 10 years later (Link *et al* 2000). In any case, clinical CT users are bound to use the artifact reduction technique supplied by their scanner's manufacturer.

3.4 Treatment planning software.

Treatment planning for HDR prostate brachytherapy at SCGH was undertaken using Brachyvision software (Varian Medical Systems, Palo Alto CA, USA). Versions 6.5 and 7.3 were used during this study. Neither version of Brachyvision accounted for tissue heterogeneity, treating the entire patient as water-equivalent. However, given the amount of artefact observed in CT data from prosthesis patients and the challenges therefore associated with obtaining accurate electron density information from the CT images, a

model that treats the body as water equivalent and therefore ignores areas of signal enhancement and deficit that will erroneously affect calculated electron densities will be acceptable, and indeed, preferred.

In comparison, Oncentra Prostate treatment planning software (Nucletron B.V. Veenendaal, Netherlands) was used at Royal Adelaide Hospital for some of the work reported in Chapter 4.3. This software used ultrasound image data, which contains no easily-decipherable tissue electron density information, which is the key requirement for heterogeneity-based radiation dose deposition calculations. The target and surrounding tissues are therefore also treated as water-equivalent. Treating the body as water-equivalent also offers an excellent opportunity to make use of MR data, which like ultrasound images contains no easily-determined electron density information.

3.5 Summary.

As demonstrated in this chapter, each imaging modality has a number of obstacles that must be overcome to acquire clinically useful images for HDR brachytherapy treatment planning in the presence of bilateral hip prostheses:

- ***Ultrasound.*** The most significant disadvantage of U/S is hyper-echoicity of implanted needles that reduces image quality, particularly for anatomy and implanted needles anterior to other needles. Unfortunately, rectal gas close to the transducer is highly reflective and may cause troublesome shadowing artifact, and reverberation artifact may affect an observer's ability to accurately identify some needles. Reflections from multiple needle tracks may also make accurate identification difficult.

- ***Magnetic Resonance Imaging*.** The ability of MR to provide excellent soft-tissue detail makes it attractive for prostate imaging. However, artifact such as image blur and ghosting due to patient motion are common, and under-sampling of high spatial frequencies can be problematic with hip prostheses and potentially with implanted needles. RF-induced heating is a known risk with conductive devices such as the needles and marker wires used in brachytherapy. The principal metals in hip prostheses all produce significant susceptibility artifact, and may make clinically useful image acquisition for prostate HDR brachytherapy treatment planning particularly challenging.

- ***Computed Tomography.*** Despite being the modality of choice at most centres, CT demonstrates significant challenges when used for patients with bilateral hip prostheses. Beam hardening may cause darkening towards the centre of sufficiently attenuating objects due to the longer pathlengths. Mis-registration, blurring, shading and streaking may be due to patient motion during the CT scan, and partial volume averaging may reduce the accuracy of distal needle tip identification. Streak and signal deficit may be so pronounced in patients with high-density metal implants that reconstructed images are no longer useful.

With respect to the criteria described earlier in this chapter, each modality offers the following possibilities for successful image acquisition in bilateral hip prosthesis patients:

- *Accurate visualisation of implanted HDR brachytherapy needles, with no loss of detail particularly at the needle tips* is perhaps most likely with CT, as partial volume effects are typically more significant in U/S and MR due to their less good spatial resolution in the z-direction (typically the axial slice thickness direction).

- *In the case of fractionated HDR treatment, clear visualisation of implanted fiducial markers for prostate and needle localisation at each fraction* is again perhaps more likely with CT as it relies upon electron density, or ultrasound which also relies upon material density differences to generate image data. Typical markers are made from gold or silver, and have significantly higher electron density than tissue and bone.

- *Distortionless images for accurate volume definition and accurate needle separation, ensuring accurate dose calculation* are most likely to be obtained from CT since it is a comparatively straightforward projection imaging technique. Ultrasound may also fare well in this respect, but MR imaging in the presence of bilateral hip prostheses may suffer significant distortion.

- *Clear detail of prostate anatomy – at least, sufficient detail to enable accurate definition of the target volume for radiotherapy treatment planning* is most likely with MR imaging, which is known for its ability to resolve soft tissue detail. CT will not perform as well in this respect as its soft tissue contrast resolution is not as good as MR, and streak artifact is a known problem.

The summary above demonstrates that an optimum HDR prostate brachytherapy imaging modality for bilateral hip prosthesis patients is not obvious. Ultrasound, MR and CT all have advantages and disadvantages for the reliable acquisition of clinically useful images for treatment planning. For each modality, the detailed clinical studies undertaken here are reported and discussed in Chapter 4.

Chapter 4 . Clinically useful image acquisition.

As noted in Chapter 3, imaging modalities share common artifacts such as partial volume averaging, and unique artifacts that can at times (at least in a clinical setting) present an insurmountable challenge with busy patient workloads without state-of-the-art imaging equipment. The approaches taken here to minimise the impact of artifact in each imaging modality (Ultrasound, MR, and CT) to enable reliable acquisition of clinically useful images for prostate HDR brachytherapy treatment planning are discussed in this chapter.

4.1 BiLateral Implant Prostate (BLIP) phantom.

It is essential in many cases to use a phantom rather than with a real patient when working towards optimised image parameterisation. Clearly, a phantom can only approximate what may be observed in an actual patient. However, a phantom is compact and easily transportable, and a variety of prostheses and brachytherapy needle 'modules' can be interchanged. A useful comparison showing the loss of information in patient images compared with phantom images was provided by Hellebust *et al* (2010), and is reproduced in figure 4-1. To this end, a bilateral hip prosthesis implant prostate (BLIP) phantom (figure 4-2), described in more detail in Appendix 3, was developed to enable investigations without patient subjects.

Figure 4-1: Coronal (top row) and transverse (bottom row) appearance of titanium needles in CT and MR images in a phantom and in a real patient (from Hellebust *et al* 2010).

Briefly, the phantom ‘body’ was made from wax and contained three PVC tubes into which prosthesis and implant ‘modules’ were inserted (figure 4-2). Several modules were constructed with acetabular cups and femoral stems in typical implant geometry.

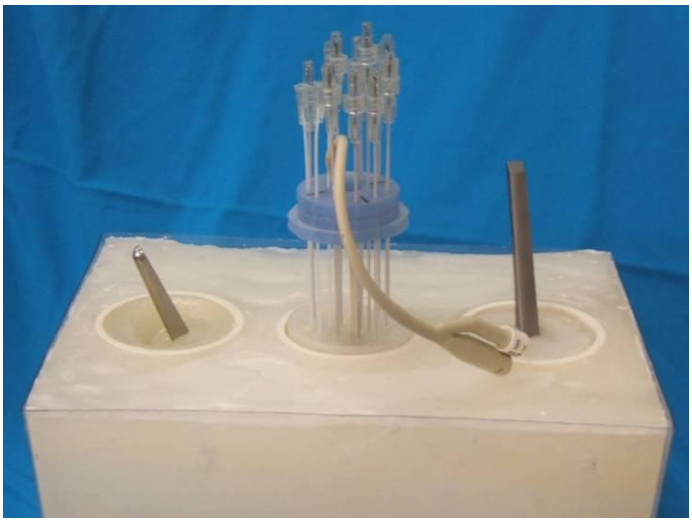

Figure 4-2: Original SCGH Bilateral Implant Prostate (BLIP) phantom, constructed from wax with PVC inserts to accept hip prosthesis and brachytherapy needle ‘modules’.

Acetabular cups were all titanium, while stainless steel, cobalt-chrome and titanium femoral stems and heads were installed into the modules. Brachytherapy needle implant modules (plastic and stainless steel) replicated the implants used at SCGH, 15 needles in an AOS (Alpha Omega Services, Bellflower, CA, USA) 17-gauge Syed-Neblet prostate brachytherapy kit. A Foley catheter and balloon were included to represent the urethra.

4.2 Flexible marker wires.

Given the quality of CT data from bilateral hip prosthesis patients who had received EBRT, it was apparent that an alternative modality was needed. When this work commenced, ultrasound-based treatment planning for HDR brachytherapy was not available at SCGH, but evaluation of an early commercial system had concluded that the longitudinal array in the available biplanar transrectal transducers had insufficient length to capture the entire prostate and distal tips of implanted needles in a single scan. At that time it was not possible to concatenate image data sets in the TPS. MR imaging was proposed, but it was not obvious that MRI would provide sufficiently clear and undistorted images of the prostate and implanted needles, neither was it certain that metal needles and obturators would be unaffected by the high magnetic fields in an MR scanner.

MR-compatible plastic needles were in regular use at SCGH in each HDR implant. However, the steel obturators used to stiffen the plastic needles to assist implantation were not MR compatible. As well, when removed, the needles flexed (figure 4-3), and the geometry was different from that recorded in the treatment plan. Tests with the BLIP phantom showed that suitable obturators would assist plastic needle identification, in particular the distal needle tips in MR images.

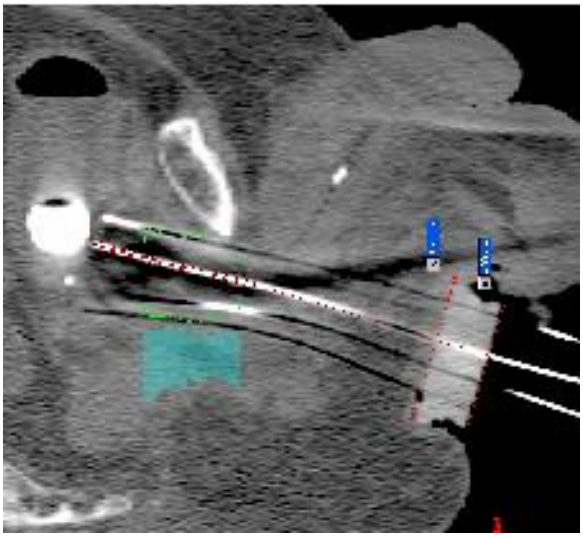

Figure 4-3: Saggital image of plastic needle flex after metal obturators removed.

Figure 4-4 shows a modified obturator constructed from a discarded ‘dummy’ wire used in the HDR afterloader. The nitinol metal wires were non-ferrous, and replicated the active source wire flexibility. The distal end of a discarded wire was cut to length (like the active source wire, the distal end was annealed for flexibility), and one end was passed through a drilled plastic Leur cap fitted with a Teflon plastic sleeve. The Leur cap was fitted to a mating coupling on a plastic needle, and the wire was pushed until it reached the distal needle tip, then locked into position with a brass clamp. The wire obturator ensured needle flex in treatment planning images would closely match treatment geometry.

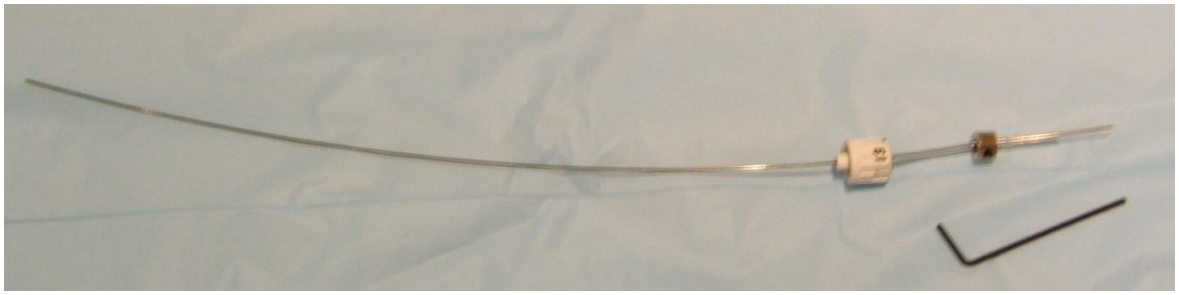

Figure 4-4: Flexible MRI-compatible metal obturator for plastic needles. Length fixed via Leur cap (white) with locking nut on brass clamp tightened onto Teflon tube using allen key.

If a distal needle tip could not be accurately identified in treatment planning images, a secondary technique to determine needle tip location was required. As shown in figure 4-5, the needle template sewn to the patients' perineum served as a reference point from which each distal needle tip could be physically measured and compared with the length measured in images. Differences were corrected by redefining the needle tip in the TPS.

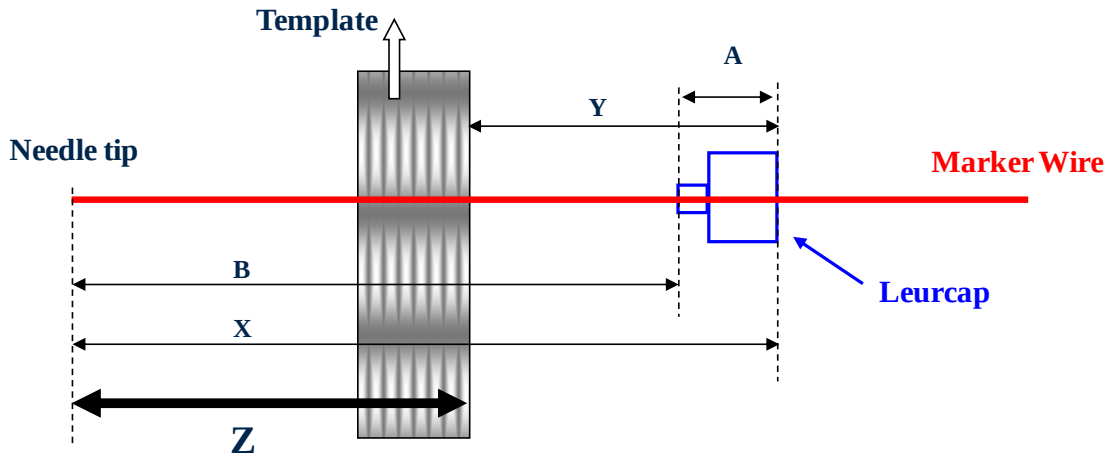

Figure 4-5: Determining Z, distance from the proximal needle template surface to the distal wire tip, for comparison with treatment planning image data.

Figure 4-5 shows how the distance *Z* between the proximal face of the needle template and the distal wire tip is determined by physical measurement: the length *A* of the Leur cap is known, the distance *Y* between the proximal surface of the Leur cap and the needle template is measured at completion of the implant procedure in theatre. Length *Y* is checked immediately prior to CT or MR dataset acquisition, and again afterwards. The wire is then removed from the needle and distance B is measured. The distance *X* from the proximal end of the Leur cap to the distal wire tip is $X = A + B$, and from the proximal surface of the needle template to the distal wire tip is $Z = X - Y$. Tests showed the length *Z* was typically determined to within ± 0.3 mm.

Table 4-1 shows an implant worksheet used with SCGH wire obturators. The 'Difference' column indicates the difference between the physically measured length Z and the length determined from treatment planning image data. If the difference was greater than 0.5 mm, the tip location was adjusted accordingly in the treatment plan before radiation dose planning commenced.

BI-LAT HIP REPLACEMENT- MODIFIED MARKER WIRE LENGTH CHECK SHEET									
Needle Number	A	B	(A+B)	THEATRE	(X-Y)	CT	MRI	Difference	Catheter
	(mm)	(mm)	X (mm)	Y (mm)	Z (mm)	Z (mm)	Z (mm)	(mm)	length(cm
1	12.5	208	220.5	83.12	137.38	136.05		-1.33	
2	12.5	207	219.5	81.96	137.54	136.92		-0.62	
3	12.5	208	220.5	81.56	138.94	137.92		-1.02	
4	12.5	209	221.5	81.31	140.19	138.5		-1.69	
5	12.5	207	219.5	77.46	142.04	141.95		-0.09	
6	12.5	208	220.5	77.22	143.28	142.6		-0.68	
7	12.5	207	219.5	74.3	145.2	145.3		0.1	
8	12.5	206	218.5	77.46	141.04	140.93		-0.11	
9	12.5	210	222.5	76.18	146.32	145.5		-0.82	
10	12.5	208	220.5	74.33	146.17	145.68		-0.49	
11	12.5	206	218.5	78.33	140.17	139.58		-0.59	
12	12.5	207	219.5	74.71	144.79	142.48		-2.31	
13	12.5	208	220.5	79.45	141.05	140.71		-0.34	
14	12.5	206	218.5	70.15	148.35	148.2		-0.15	
15	12.5	207	219.5	75.25	144.25	144.41		0.16	
16									
17									

Table 4-1: Implant worksheet to determine Z, distance from proximal needle template surface to distal wire tip, for comparison with treatment planning image data.

Importantly, to enable length comparisons between physical measurement and image data, the CT (or MR) dataset for bilateral hip prostheses patients was extended to include the proximal face of the needle template on the patient's perineum, For non-prosthesis patients, scans typically terminated about 20 mm below the apex. This approach significantly reduced the likelihood an entire dataset would need to be re-acquired due to uncertain needle tip definition.

4.3 Trans-Rectal Ultrasound (TRUS).

TRUS has a long-established role in image-guidance for low dose-rate (LDR) brachytherapy (Cesaretti, 2007), both for treatment planning (Rivard *et al.*, 2009) and for image-guided needle and radioactive seed placement (Thomadsen *et al.*, 2008). Accurate visualisation of tumour is not of primary importance for LDR image-guidance, although growing interest in focal therapy techniques (Turpen and Rosser, 2009) may see increased use of contrast-enhanced colour Doppler techniques to deliberately apply higher dose in areas likely to contain tumour, and/or dose reduction in areas containing normal tissue. In LDR, TRUS images conventionally are acquired in a pre-implant 'volume study' to assess the suitability of the prostate for LDR seed implantation, and for treatment planning.

4.3.1 TRUS volume studies for HDR brachytherapy.

As in LDR brachytherapy, at SCGH and in many other centres, a TRUS volume study is acquired immediately prior to HDR needle implantation, and serves three main functions:

- Prostate base and apex, and the lateral and anterior-posterior extent of the target volume are visualised. The surgeon, in consultation with radiation oncologist and physicist, determines a needle template alignment that potentially will provide optimal dosimetric coverage (one aim is to reduce 'loading' needles with long dwell times to achieve desired dosimetry statistics).
- TRUS images, in combination with coronal fluoroscopy images, guide marker seed implantation at the prostate base and apex.
- A TRUS volume study provides the radiation oncologist with a useful visualisation of the target volume, in case subsequent treatment planning images acquired with all implanted needles in place provide inadequate visualisation of the target volume.

A TRUS volume study at SCGH uses a model 8848 (B-K Medical, Herlev, Denmark) biplanar transrectal ultrasound transducer with signal frequencies in the range 5-9 MHz, to give a useful imaging range of about 6 cm in tissue. The transducer is connected to a control console and is mounted into a 'stepper' (Civco Medical Solutions, Iowa USA) that allows calibrated steps in the axial direction and that enables freely-adjustable transducer orientation with precise and stable fixation. A calibrated grid (commercial plastic or in-house stainless steel re-useable) is attached to the stepper to assist needle placement. The transducer is inserted into a water- or gel-filled sleeve to improve image quality.

In volume studies at SCGH, patients are anaesthetised, placed in the lithotomy position and a Foley catheter filled with contrast is inserted to improve visibility of the urethra. The ultrasound transducer is introduced and advanced until the prostate base is identified. The physician endeavours to ensure the urethra is aligned with the central grid column along the prostate's full length, and reduces or eliminates pubic arch interference for needle access. Prostate images are acquired in 5 mm steps, from 5 mm superior of the base to 5 mm inferior of the apex (figure 4-6). The posterior and lateral prostate borders are generally clearly identified, and the anterior border is clear in most images. The transition and peripheral zones of the prostate can be identified, and the urethra is visible in each transverse slice. Towards the apex the pelvic arch is visible anteriorly. If necessary, the transducer (or patient) can be moved to assist clear access.

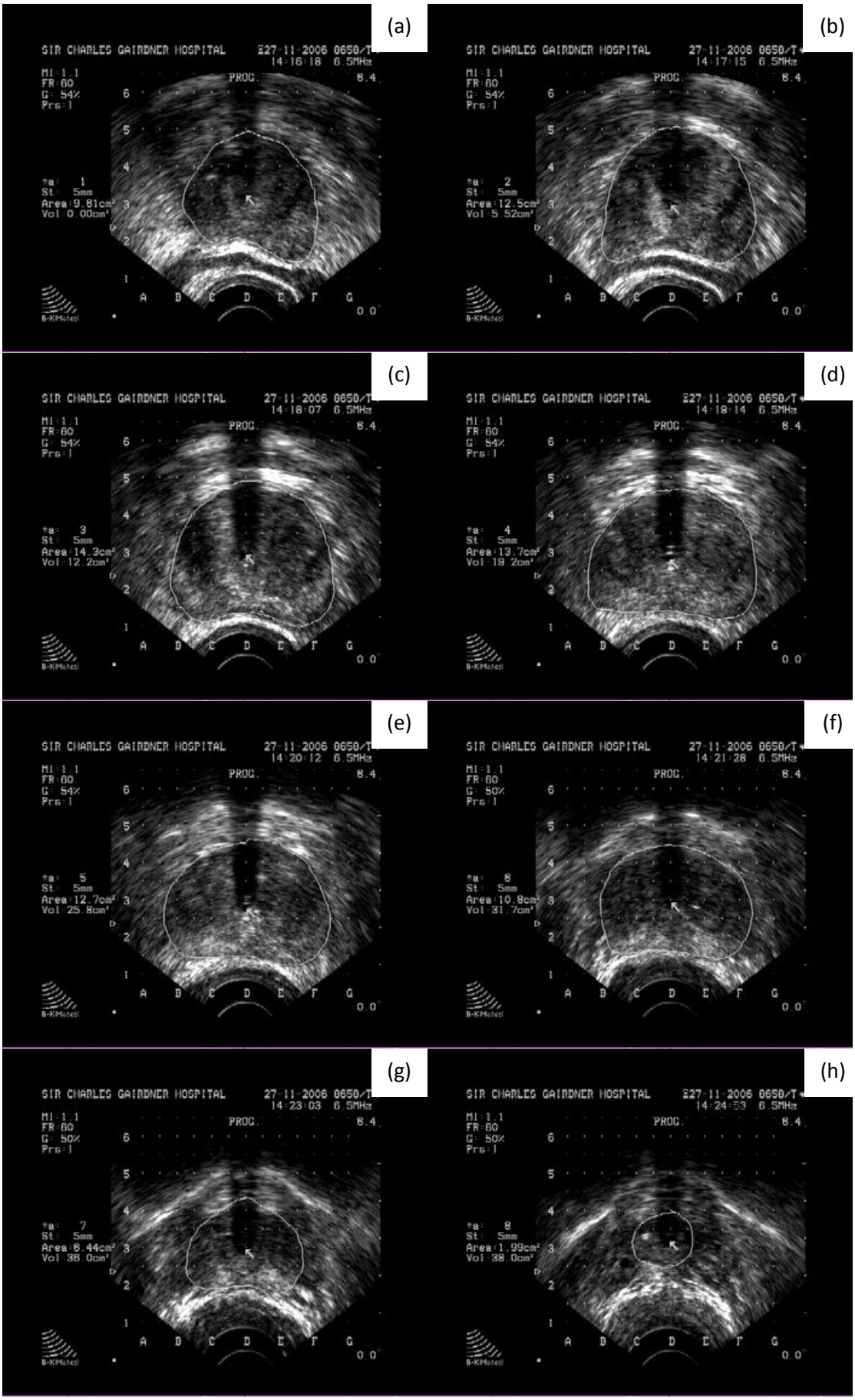

Figure 4-6: Ultrasound volume study from prostate base (a) to apex (h).

For HDR prostate brachytherapy, TRUS enables real-time guidance for needle placement, and is routinely used to obtain prostate volume study information prior to or after needle insertion. Some centres also use TRUS prostate images for 'real time' treatment planning: the dosimetry plan for the first treatment fraction is based upon TRUS images, and radiation dose is delivered while the patient is still anaesthetised. One incentive is the potential to reduce the amount of time a patient has needles implanted.

For a patient with bilateral prosthetic hips, the attraction of TRUS-based treatment planning is clear: prostate images are acquired without the need for signal to traverse the prostheses, and the limited penetration depth of around 6 cm for a 6.5 MHz signal means that acoustic reflections from the prostheses are unlikely to be problematic. However, accurate needle tip identification can be difficult especially for anterior needles. The most significant disadvantage of U/S for HDR brachytherapy is hyper-echoicity of the implanted needles that reduces image quality, particularly for anatomy and implanted needles anterior to other needles. Another disadvantage is that visualisation of objects above gas can be very poor, and this can be troublesome for TRUS in patients with poor bowel preparation.

4.3.2 TRUS-based treatment planning for HDR prostate brachytherapy.

Sir Charles Gairdner Hospital does not use TRUS images for HDR treatment planning, however, Royal Adelaide Hospital (RAH) in South Australia is amongst the centres that do. Several site visits were undertaken to participate in the TRUS image acquisition and planning procedures at RAH to assess the potential of TRUS-based HDR treatment planning for bilateral hip prosthesis patients. RAH patient data was not used in any subsequent analysis in this study Patients selected for prostate HDR brachytherapy at RAH satisfy at least two of three criteria: Cancer stage T2b-T3b, PSA 10-20 $ngml^{-1}$, and Gleason score 7-8. The dose prescription was 19.0 Gy delivered in two fractions a minimum of 10 hours apart. Patients also attended for a course of EBRT, with 46.0 Gy prescribed dose. The EBRT component was delivered before or after HDR brachytherapy, with a minimum 14 days between modalities. Patient preparation included steps to ensure the rectum was clear of faecal matter and gas that may obstruct TRUS images.

Implant procedure. The anaesthetised patient was placed in lithotomy position and the TRUS transducer was inserted. Four anchor needles were inserted trans-perineally into the prostate to reduce movement when subsequent needles were implanted (see figure 4-7a).

Volume study images were acquired from 20 mm superior of the base to 20 mm inferior of the apex, in 1 mm steps typically spanning 80 mm. TRUS images were exported to the TPS and prostate, urethra, and rectum were outlined, and an 'implant roadmap' was constructed. Treatment volumes were determined at this point since the prostate position did not alter by more than 1 or 2 mm when subsequent needles were inserted, and with only four anchor needles present, artifact was reduced (compare figure 4-7a and 4-7b).

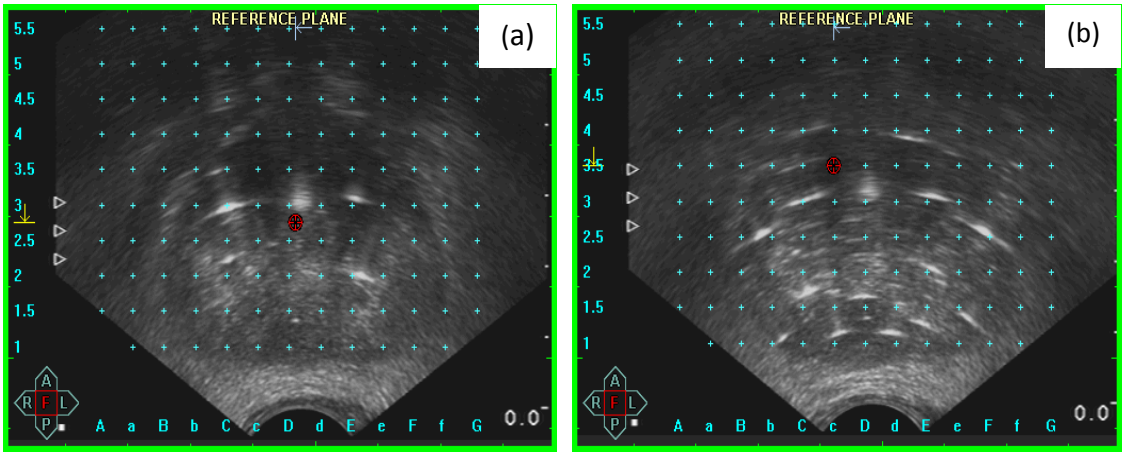

Figure 4-7: (a) Transverse TRUS image near mid-gland in prostate with four 'anchor' needles implanted. Gel-filled Foley catheter is visible at D3.0 (b) TRUS image at same location after all 19 needles were implanted. Note loss of detail towards anterior prostate.

Remaining needles were implanted to match a pre-determined template plan. Flexible cystoscopy was used to ensure that all needles penetrated the prostate and tented the inferior bladder wall. Posterior needles may be advanced into the seminal vesicles. The guidance template was locked and sutured to the perineum to secure needles in position.

The prostate volume study was repeated and imported into the TPS; needle locations in the treatment plan were adjusted to match the measured locations and prostate, urethra, and rectum outlines could be modified to match volume study images. A baseline fluoroscopic image of the implanted needles was acquired. The radiation dose treatment plan was optimised using a set of dose constraints and dose-volume-histogram data, and once approved for use, needles were connected to an HDR after-loader, radiation dose was delivered, and the patient was transferred for overnight care. The patient's legs were separated with a Charnley pillow to reduce the risk of needle or template movement.

Using figure 4-8, the needle '*free length*' was physically measured and checked against treatment planning images to ensure accurate distal tip identification. The total needle

length *L* was known, and the needle depth is *L – free length*. In the TPS the separation of between reference point and transverse U/S crystal is known, and grid location relative to reference point was monitored. The needle depth is the separation between guidance grid and transverse crystal centre. RAH found tips could be identified with ±1 mm accuracy in phantom studies, however, ±3 mm tolerance was applied in patient treatment due to increased artifact and reduced image quality.

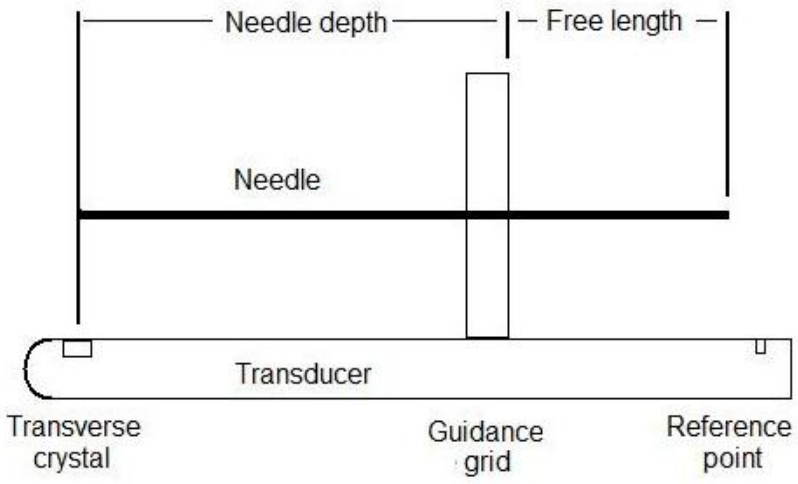

Figure 4-8: Length definitions used at RAH for distal needle tip location. The 'free length' is determined computationally by the treatment planning system, and is physically measured for comparison. If necessary, the distal needle tip location is adjusted in the treatment plan.

Treating more than one fraction. At RAH a patient's HDR brachytherapy treatment was delivered in two fractions. For the second fraction, the patient returned to the treatment room and his legs were raised to match the implant geometry. A fluoroscopic image of implanted needles and marker seeds was acquired and compared with the baseline image. If required, needles were adjusted individually under TRUS or cystoscopic guidance to match the first treatment fraction with acceptable accuracy (within 3 mm). The second fraction was delivered, needles were removed, and the patient returned to the ward.

For brachytherapy treatments involving more than a single fraction the question arises as to what imaging modality should be used for second and subsequent fractions. Some centres claim it is *not* possible to use TRUS image-based treatment planning for second and subsequent fractions (Seppenwoolde *et al.*, 2008b), citing the deleterious effects of reduced target dose and increased dose to organs at risk such as the urethra. In Seppenwoolde's study, significant dosimetric changes (up to 30% dose increase to the urethra, and up to 30% decrease to the target) were due to variable and significant prostate deformation

stemming from differences in patient posture between first and subsequent fractions, combined with absence of the transducer in the rectum. To address these issues, the patient's lithotomy position used for needle implantation should be accurately reproduced in the setup for subsequent treatment fractions, and a TRUS transducer or dummy device could be re-inserted to better match the TRUS treatment planning images (absence of the transducer in the first treatment fraction could also be problematic).

Time required for first fraction. At RAH the time from initial patient anaesthesia to completion of the first treatment fraction with real time TRUS treatment planning averaged 5.5 hours (range 4-8 hours). In comparison, at SCGH where real-time TRUS planning was not used, an operating theatre was occupied by each patient for an average of 90 minutes, and the total time for a first fraction at SCGH was similar, typically 5 to 6 hours. The potential for reduced treatment time is often cited as a benefit of TRUS-based treatment planning. However, it is a potential benefit with many caveats: (1) a theatre is occupied for the entire duration of the first fraction procedure. Where demand for access is high, CT or MR imaging modalities that remove patients from theatre once the implant is completed may be more attractive. (2) radiation barriers in the theatre must either be incorporated into the building itself, or provided via portable shields. (3) radiation safety procedures often must involve a greater number of staff than might be required with a dedicated brachytherapy treatment room. (4) a patient is anaesthetised for several hours longer than in procedures where he recovers before images are acquired.

Needle template – electronic grid alignment. Brachytherapy ultrasound consoles include an electronic grid that is superimposed over TRUS images to provide a spatial reference frame for needle localisation (figure 4-9). Most allow mechanical adjustment of the physical grid and software adjustment of the electronic grid to ensure an optimised match.

Alignment checks were made in a salt water (43 g/litre) phantom to reduce velocity-related distance errors (Pfeiffer *et al* 2008) by better matching the velocity of sound in tissue. A map indicating the alignment of electronic and physical grids (figure 4-9) was recorded. At SCGH, three stainless steel re-useable grids were each calibrated to one of three TRUS transducers. Individual lateral, axial and rotational adjustments were required due to transducer and grid construction variations. Alignment of electronic and physical grids was better than 2 mm in axial and lateral directions.

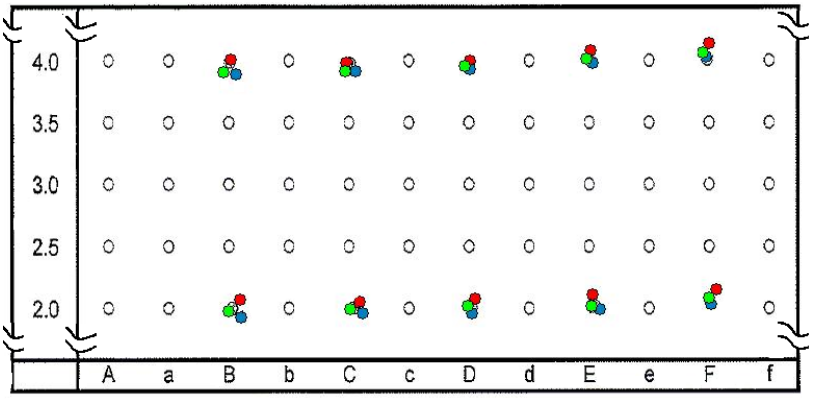

Figure 4-9: Portion of U/S needle template alignment grid. Results from measurements using three different transducer – grid combinations are shown (red, blue and green dots). Grid spacing 5 mm. Needle visualisation typically within 2 mm of true location.

Distal needle tip image accuracy. Brachytherapy needles are about 1.5 mm in diameter with blunt tips – like hollow knitting needles. Siebert *et al* (2009) reported exhaustive tests of needle tip identification accuracy using ultrasound. They tested several systems including the type used at SCGH, a range of transducer frequencies, and the inter-operator dependence of results. In transverse images distal needle tips were located (by different users) an average of -2.6 mm of the actual tip. Tips were located more accurately in longitudinal (saggital) images, with average error of -1.8 mm, but operator dependence was more pronounced. No dependence upon transmitted frequency was found. As the apparent location of the tip was more proximal than the actual tip, this may be due to partial volume averaging in the image planes, since the elevational resolution of transverse and longitudinal transducer arrays is of the order of several millimetres.

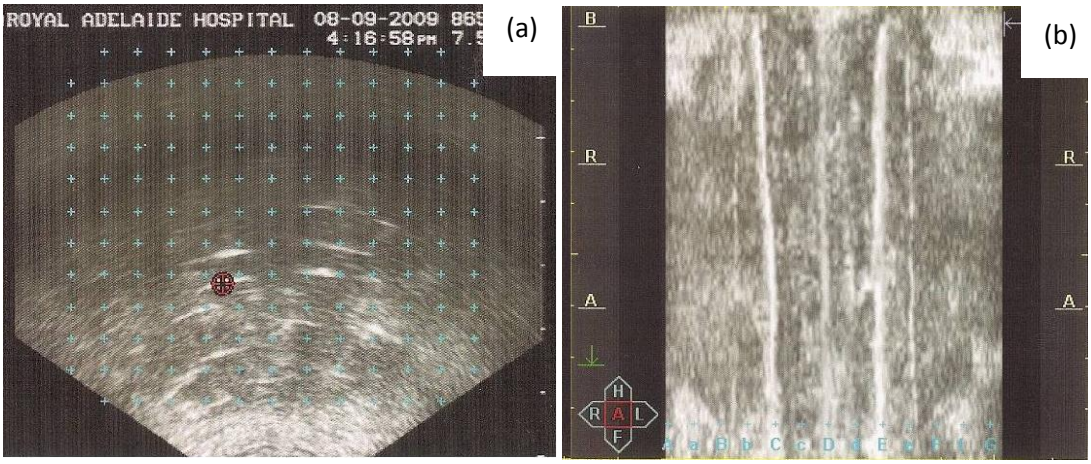

Figure 4-10: (a) Transverse view showing multiple implanted steel HDR needles in the prostate. Note faint prostate outline is visible. (b) Coronal view of implanted needles reconstructed from transverse image slice data acquired in 1 mm steps.

Ultrasound images for brachytherapy treatment planning. A typical transverse image from a prostate containing implanted needles is shown in figure 4-10(a) above. Needles are located at the midpoint of each bright flash. The low brightness of anterior needles is apparent when compared with posterior needles. The anterior prostate border is difficult to identify, and lateral borders are unclear. Figure 4-10(b) shows a typical coronal ultrasound image reconstructed in the TPS from transverse image data. Needles in the selected coronal plane are clearly visible (wide bright vertical lines), as are needles in deeper posterior planes (narrow vertical lines). The needle tip at patient left is well defined, but the needle tip at patient right is less well defined in the hyper-echoic area at the top of the image.

Figure 4-11(a) below demonstrates the potential difficulty of needle tip identification, and the reason for physical needle measurement during implant procedures. Just above the red marker the needle track is fragmented – the apparent tip may be just below the dark band, or it may extend to include the bright 'spot' above. The difference is approximately 6 mm.

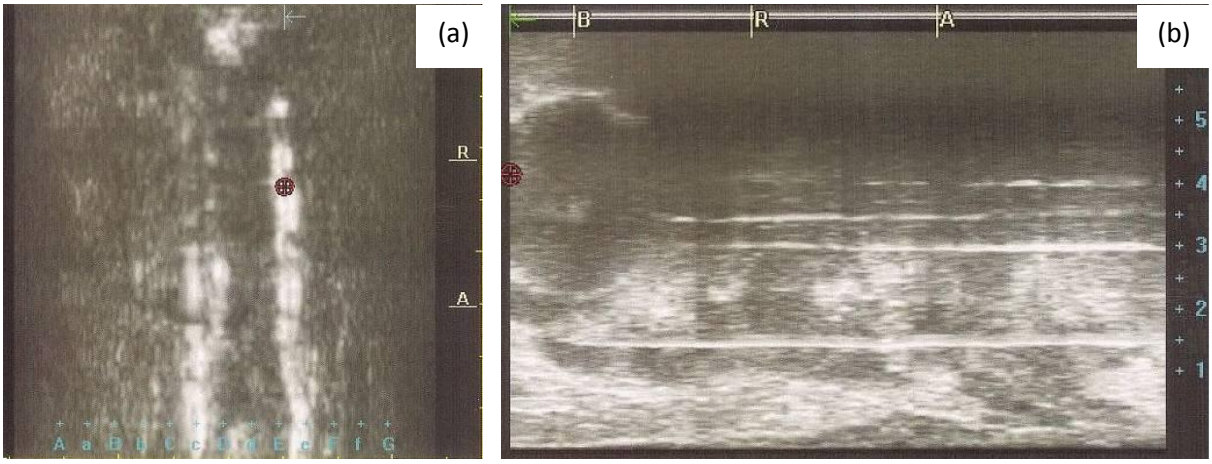

Figure 4-11: (a) Coronal view of implanted needles. (b) Saggital view of implanted needles. Images demonstrate potential uncertainty in distal needle tip identification.

Inaccurate needle tip definition leads to inaccurate dose deposition, or physical contact between the Ir-192 source and tip. At RAH, the computed 'free length' was compared with physical measurement at the time of implant, and the apparent needle tip was adjusted in the TPS to match the measured 'free lengths'. Figure 4-11(b) shows a longitudinal/saggital image of implanted needles. The round object at left is a Foley catheter balloon in the bladder. Needles are easily identified in figure 4-11(b), and tips are generally clear. A hypo-echoic band is visible in the image close to the relatively faint tip of one needle, and several needle tips are close to the balloon. Some tips are difficult to identify in hyper-echoic areas adjacent to the balloon and near the seminal vesicles.

Bilateral hip prosthesis patients. Essentially, the discussion above is unaltered for patients presenting with bilateral hip prostheses. While great care is taken to position all patients in the lithotomy position for needle implantation and subsequent treatment fractions, and during transfers between ward beds and treatment couches, perhaps more care must be taken to limit the bilateral prosthesis patient's hip flexure during these stages.

4.4 Magnetic Resonance Imaging.

Conventional MR imaging with a 1.5 T scanner proved particularly challenging – investigations and findings are described below.

4.4.1 MRI BLIP phantom study.

The BLIP phantom was MR scanned with a range of scan parameters to gain an appreciation of the influence of hip prostheses upon image quality. Several different prostheses were used in different pairings to simulate the combinations found in real patients. A suitable image was defined as having adequate detail to visualise implanted needles and fiducial markers, and containing minimal distortion in the target volume. However, the BLIP phantom was a highly simplified approximation to a real patient, and what worked well for the phantom may not work well for a real patient. Figure 4-12, a coronal image acquired from the BLIP phantom using a 1.5 T Siemens Sonata scanner illustrates many of the challenges facing MR imaging in the presence of hip prostheses.

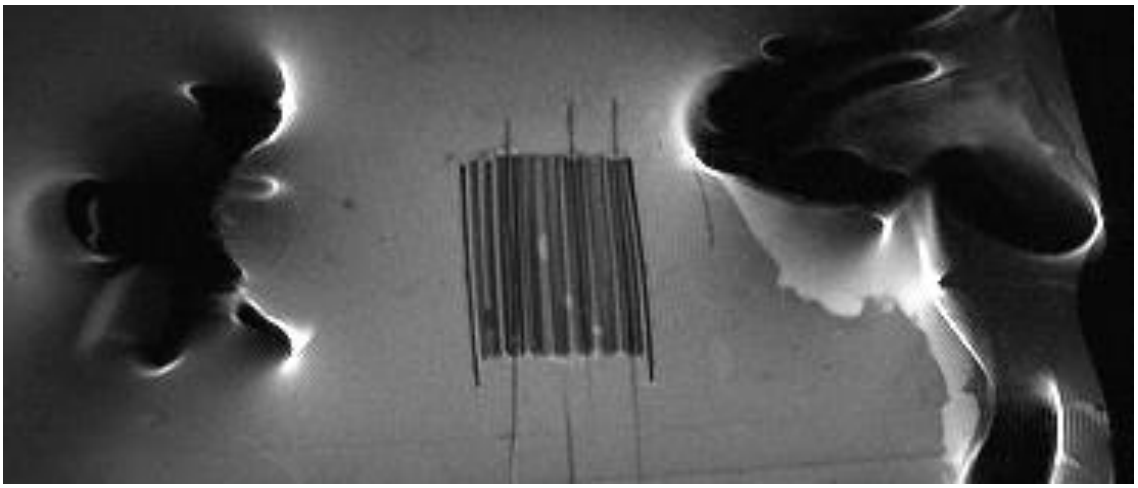

Figure 4-12: Coronal MR image from BLIP phantom containing bilateral hip prostheses (titanium acetabular cups, cobalt-chrome stems) with plastic grid containing air-filled plastic needles at centre. T2 TSE, 904 ms TR, 102 ms TE, COL phase encoding direction, 150° flip angle, 3 mm slice thickness. Bandwidth 515 kHz.

In figure 4-12, metal susceptibility-induced signal void with adjacent high signal intensity artifact around the prostheses is obvious, and has made the prostheses unidentifiable. Gibbs ringing is clear at bottom right, and was present in numerous locations in many image slices. Gradient-related distortion of the implanted air-filled plastic grid (a block of 6 mm x 50 mm plastic wall plugs) has caused non-physical lateral curvature of up to 3 mm in the plastic grid that represented the volume that would contain prostate tissue in a real patient. The implications for accurate target delineation and radiation dose calculation are clear.

4.4.2 Patient data from SCGH.

SCGH patients were imaged using a Siemens Sonata 1.5 T MR scanner. Each of the patients considered for MR imaging was implanted with plastic needles and transferred from the surgical recovery area to a waiting area adjacent to the MR facility, then back to a ward, and then to the HDR brachytherapy treatment area. Co-ordination of services and facilities relied upon the goodwill and understanding of several area supervisors, as arrival and departure times from each facility were usually not predictable. Once at the MR facility patients were transferred to an MR table, obturators were removed or replaced with nitinol markers, and the patient was prepared. Once set up, scans required 12-15 minutes to complete. Patients invariably found the experience long, uncomfortable, and disorienting – image blur due to patient movement was an inevitable artifact in almost all cases.

Several of the initial patients are discussed below. Selected MR scan protocols and the clinical utility of images subsequently obtained for HDR treatment planning are discussed. For the first few patients, prior CT scans had shown excessive streak artifact and signal deficit. Lack of anatomical detail and an inability to accurately identify the distal needle tips made those CT images unsuitable for treatment planning. At this point, MR imaging was an untested last resort for the HDR prostate brachytherapy patients.

Patient #1. This patient had a cobalt-chrome stems and cobalt-chrome shell UHWMPE acetabular cups. Stainless steel obturators were removed immediately prior to imaging and needles contained only air. Images were remarkably free of artifact and distortion, with high contrast resolution, and HDR treatment planning proceeded successfully. A short T1, TSE sequence was selected by attending MR staff to reduce susceptibility artifact. Ideally, shorter relaxation time TR than the selected 904 msec should further reduce susceptibility artifact. Figure 4-13(a) shows little blurring and the prostate was clearly visible.

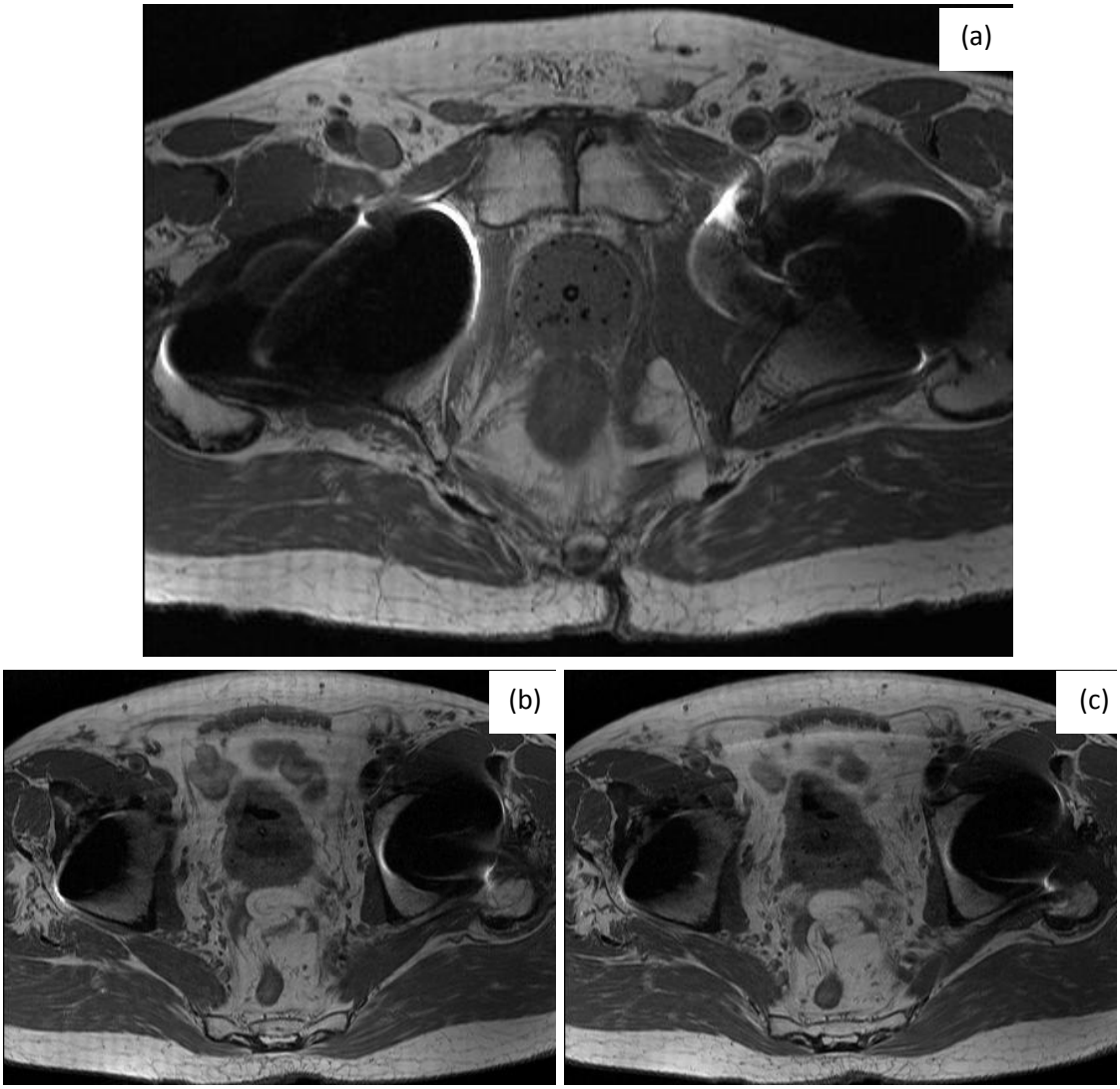

Figure 4-13: MR images from patient #1 (a) near centre of prostate, (b) and (c) towards distal ends of implanted plastic needles. The prostate is near the centre of each image. Implanted needles are visible as small black dots in the prostate. T1 TSE, 904 ms TR, 11 ms TE, COL phase encoding direction, 150° flip angle, 3 mm slice thickness, bandwidth 150 kHz.

Large areas of signal void (susceptibility artifact) bounded by arcs of high signal intensity characterise the implanted prostheses, of which very little detail can be discerned. Fortunately, this was inconsequential for treatment planning. Artifact and gradient-related distortion appeared to be minimal near the prostate in the image centre. The implanted plastic needles appeared as signal void (black dots), and the urethral catheter was visible as a larger black dot near the image centre. Localised signal void in the prostate is evident in figure 4-13(a), where dark patches towards the posterior prostate edge align with several needle voids. Figures 4-13(b) and 4-13(c) show transverse slices from the same patient at locations corresponding to the distal needle tips, and show the tips were not difficult to distinguish from surrounding tissue.

Patient #2. This patient had a cobalt-chrome stem in each femur, a cobalt-chrome shell UHWMPE acetabular cup in the left hip and a titanium shell UHWMPE cup in the right hip. Plastic needles were implanted, the stainless steel obturators were removed and needles contained plain air. The patient was of similar build as Patient #1, but identical scan parameters produced images of reduced quality. Significant distortion was observed near the needle tips, and despite much advice and assistance from attending MR staff, and three separate attempts with a range of T1 and T2 sequences, needle tips could not be accurately or reliably identified in any image dataset, and treatment was abandoned.

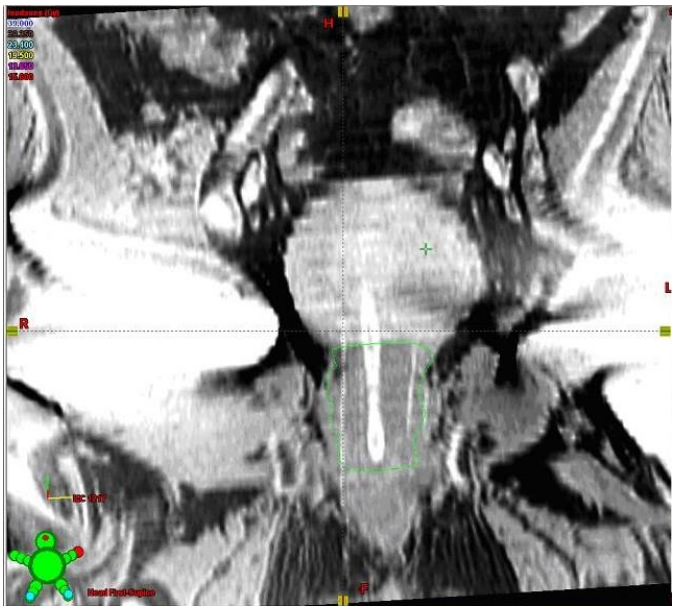

Figure 4-14: Coronal MR image from Patient #2. Image greyscale inverted and window adjusted to maximise visualisation of air-filled needles. T1 TSE, 1170 ms TR, 12 ms TE, COL phase encoding direction, 150° flip angle, 3 mm slice thickness.

Figure 4-14 shows the T1-weighted TSE sequence with TE = 12 msec, TR = 1170 msec, and 3 mm slice thickness, which provided the least fragmented needle images (fragmentation makes tip definition unreliable) with least distortion and least artifact. The greyscale was inverted to improve needle visualisation (thin near-vertical white lines towards centre). The urethral catheter appears as a thick vertical white line. Partial volume averaging was evident in the 'stepped' bladder edge superior to the prostate. Differences in susceptibility artifact between left and right prostheses appeared minimal. Implanted fiducial markers were difficult to identify – given their small dimension (0.8 mm diameter x 4.5 mm length), the signal was essentially 'absorbed' in the MR image voxels (1x1x3 mm). As well, use of 12-bit display monitors at the MR facility made it difficult to predict how much detail would be lost on the 8-bit monitors of the brachytherapy TPS.

Failure to successfully obtain clinically useful MR images from this patient underlined the relevance of this investigation. Ideally,

- A reliable MR sequence would provide acceptable images for brachytherapy treatment planning in patients with any combination of prosthesis types.
- MR images would be distortionless to ensure accurate volume definition and spatially accurate needle location data to ensure accurate dose calculation.
- Given the uncertainty of needle tip identification due to partial volume averaging, a technique to independently verify the distal needle tips was required.
- A 'backup' modality was essential for cases where MR images were unacceptable.

Patient #3. This patient had a titanium stem and ceramic shell in his left hip, and a cobalt-chrome stem and shell in his right hip, each with UHMWPE acetabular cup. As the coronal CT scout image in figure 4-15 shows, the prostheses types can be easily distinguished. The more electron-dense cobalt-chrome prosthesis at patient right appears more white.

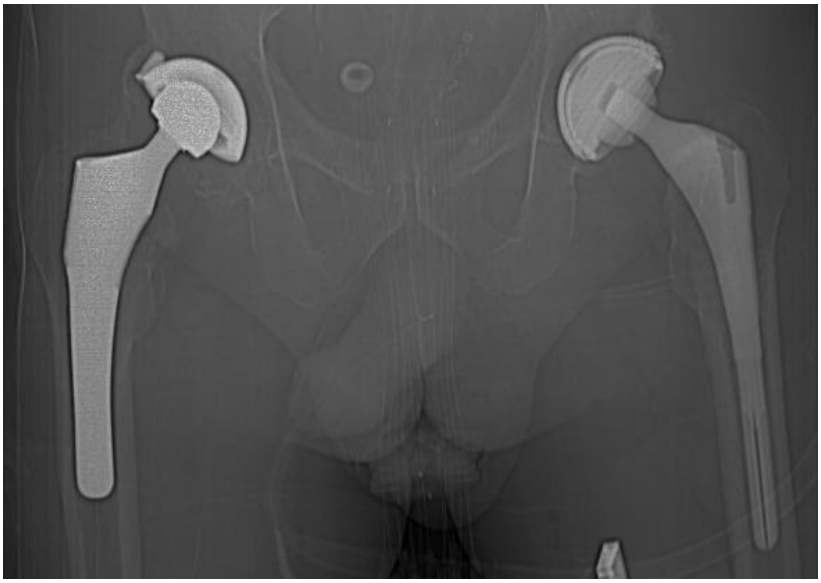

Figure 4-15: CT scout image from Patient #3. Titanium-ceramic (patient Left) and cobalt-chrome prosthesis (patient Right). Implanted plastic needles are easily visualised.

From this patient onwards, non-magnetic nitinol marker wires were used in the plastic needles to reduce the risk of needle kinks during patient transfer and to provide a means of independently identifying needle tips. Scans were extended to include the implant template, enabling measurement of needle lengths observed in treatment planning images for comparison with physically measured lengths as described in Chapter 3. In some cases the apparent and physically measured lengths differed by 10 mm or more.

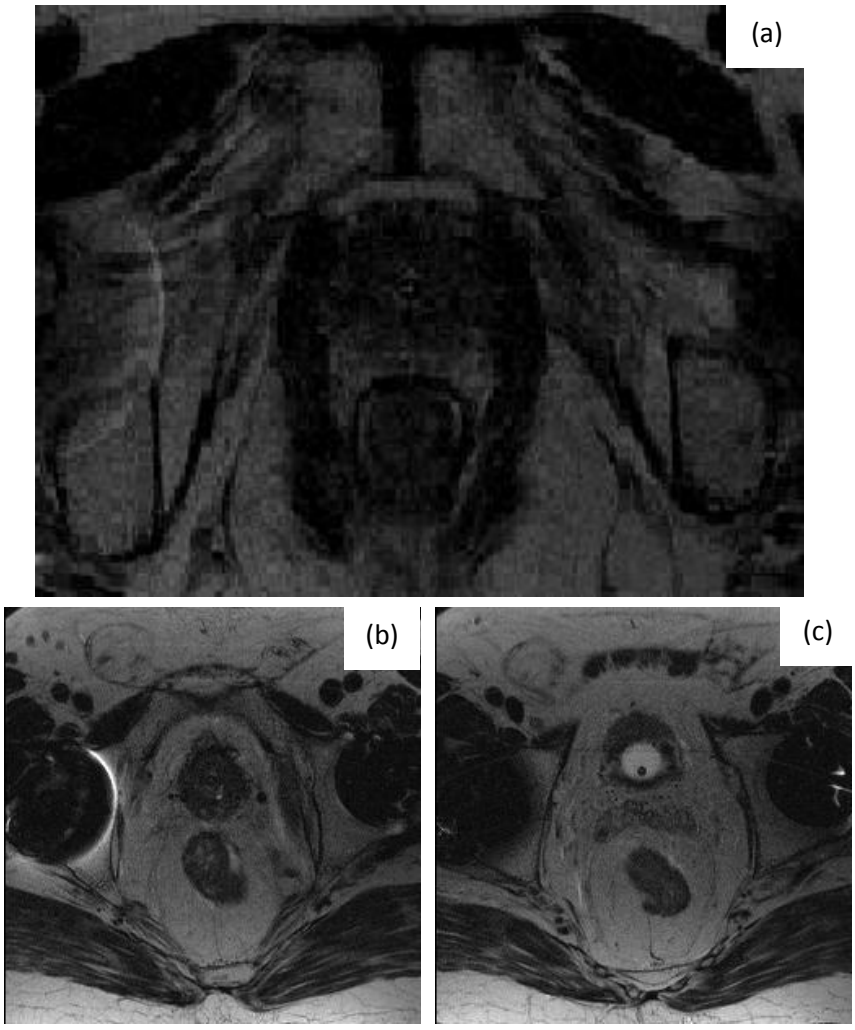

Figure 4-16: MR images from patient #3 (a) transverse plane towards prostate base, (b) and (c) towards distal end of plastic needles. Prostate near image centre. Needles visible as small black dots (signal void) in prostate. T2 TSE, 904 ms TR, 102 ms TE, COL phase encoding direction, 150° flip angle, 3 mm slice thickness. Bandwidth 515 kHz.

Figure 4-16 shows MR images from patient #3, acquired with a wide bandwidth T2 TSE sequence similar to that successfully applied by others (Menard *et al.*, 2004). Despite our hope that the sequence would optimise needle visibility without compromising prostate detail, the images were grainy, with poor contrast, and lacked detail. Window and level adjustments did not improve contrast resolution. While not necessarily disadvantageous for treatment planning because the soft tissue detail was sufficiently good to enable target outlining, the inability in these images to identify any of the reference markers removed the possibility of needle shift checks prior to treatment fractions (see Chapter 5), and the images were therefore declared unacceptable. Fortunately, acceptable CT data (Figure 4-17), in which the needles and markers were clearly defined, were acquired and used for treatment planning in combination with TRUS volume study data.

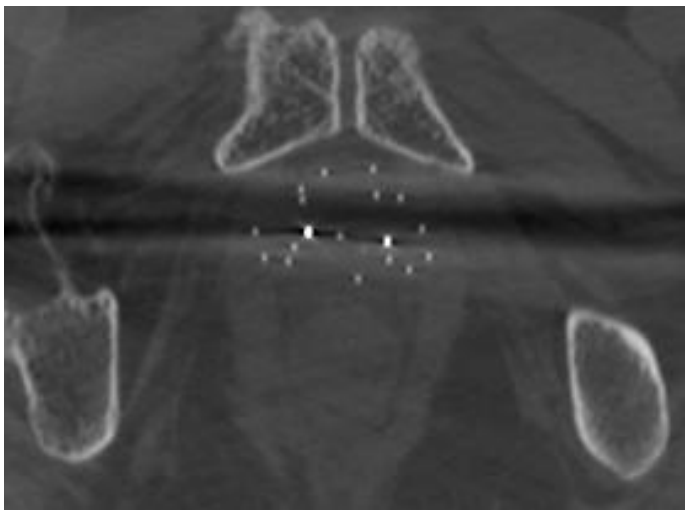

Figure 4-17: Transverse CT slice from Patient #3 demonstrating clear visualisation of prostate tissue and nitinol marker wires in plastic needles. Two gold fiducial markers are easily distinguished from the needles. Note minimal streak and signal deficit.

Patient #5. This patient had cobalt-chrome stems and titanium shells with UHMWPE acetabular cups. Figure 4-18 shows that for this MR sequence, despite improved spatial resolution in the transverse plane, wide bandwidth, long TR, and long TE, the fiducial markers were undetectable, and the distal needle tips were again poorly defined.

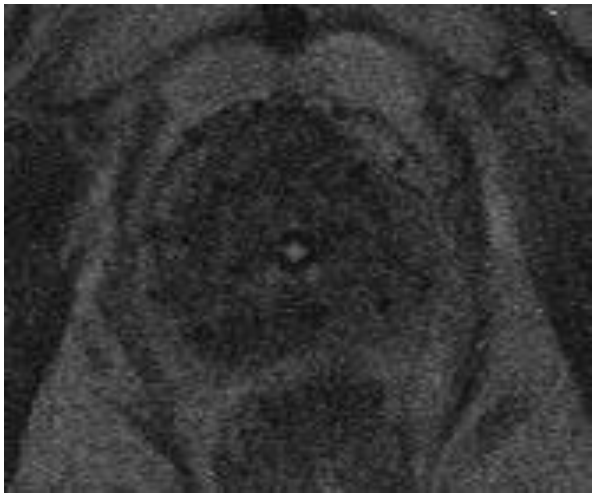

Figure 4-18: MR image from patient #5 in transverse plane towards prostate base. T2 TSE, 9670 ms TR, 104 ms TE, COL phase encoding direction, 150° flip angle, 3 mm slice thickness. Bandwidth 435 kHz.

For each of the following seven patients the most successful MR sequences from previous patients were repeated, however, none would consistently provide acceptable data for HDR prostate brachytherapy treatment planning. An updated multi-slice CT scanner was used to

acquire ‘backup’ images that usually were of acceptable quality and indeed were used for treatment planning in many of the first 10 patients. A clinical decision was therefore made to discontinue MR scans of bilateral-hip prosthesis patients.

4.4.3 Endorectal coil.

While the useful imaging range of an endorectal coil is only a few centimetres (Kim *et al.*, 2008), it is well-suited to prostate imaging. Previously, Kim *et al* (2005) noted that a rigid coil minimised prostate distortion, an important consideration for treatment planning as treatment delivery was typically done with the coil removed. Futterer *et al* (2007) compared the staging accuracy that could be achieved for prostate tumour using images obtained with a 1.5 T MR scanner with T2-weighted FSE sequences and a pelvic phased array body coil, and images acquired using a T2-weighted FSE sequence and an endorectal coil. They found the coil significantly improved visualisation of anatomic detail. The difference is demonstrated in figure 4-19, adapted from Heijmink *et al* (2007), where the improved spatial and contrast resolution afforded by an endorectal coil are clear.

NOTE:
This figure is included on page 63 of the print copy of the thesis held in the University of Adelaide Library.

Figure 4-19: (a) axial pelvic phased array T2-weighted FSE MR image and (b) corresponding axial endorectal pelvic phased array T2-weighted FSE MR image. Note enlarged rectum due to in-situ endorectal coil. From Heijmink *et al* 2007.

Improved image quality from endorectal coils increased the accuracy and specificity for extra-capsular extension, and reduced over-staging compared with body coil images. Heijmink *et al*’s study used a pelvic phased array body coil and an endorectal coil with a 3 T MR scanner. More motion artifact was observed in images acquired with an endorectal coil, but image quality and localisation were improved compared with body array coil data. The clarity and detail that may be obtained with an endorectal coil was convincingly demonstrated for prostate HDR brachytherapy by Menard *et al* (2004). In their procedures the patient was anaesthetised and needles were inserted under MR image guidance.

Treatment planning images were acquired without moving the patient, who remained anaesthetised throughout the procedure. MR images were used for needles identification and treatment planning, after manual manipulation of DICOM image data headers to ensure reconstructed image planes were normal to the implanted needles (Citrin *et al.*, 2005). Alignment of image planes in this way assisted the accuracy of needle tip detection.

Unfortunately at SCGH, an endorectal coil was not available at any stage of this study. As well, there is one key difference between procedures undertaken at SCGH and those done by Menard *et al*; at SCGH needles were inserted under general anaesthesia in a standard theatre, and the patient when sufficiently recovered was transferred to an MR facility for treatment planning image acquisition. Given that patients at SCGH were conscious and already experienced difficulty remaining immobile during the 12-15 minute MR image acquisition, we may speculate that for a conscious patient the added discomfort of an in-situ endorectal coil may negate potential benefits.

4.5 Computed Tomography.

Two aspects of CT imaging were of greatest concern for this study. Investigations focused on the metal artefact reduction techniques applied to reduce streak and artifact in images from bilateral hip prosthesis patients, and the ability of images to simultaneously provide adequate soft tissue detail for accurate target delineation. Investigations also focused on the impact of partial volume effects, and window and levelling techniques, on the accuracy of needle tip definition in the treatment planning system.

4.5.1 BLIP phantom study.

To test the metal artifact reduction techniques of different CT manufacturers, in July 2008 the BLIP phantom was taken to three different radiotherapy centres in Australia. The phantom was fitted with a ‘worst case’ combination of stainless steel prostheses and plastic needles. A GE Lightspeed RT16, Siemens Sensation 16 Open, and Toshiba Aquilion LB were tested. The manufacturer’s applications specialists kindly provided advice on the optimum settings for metal artefact reduction for their particular scanner.

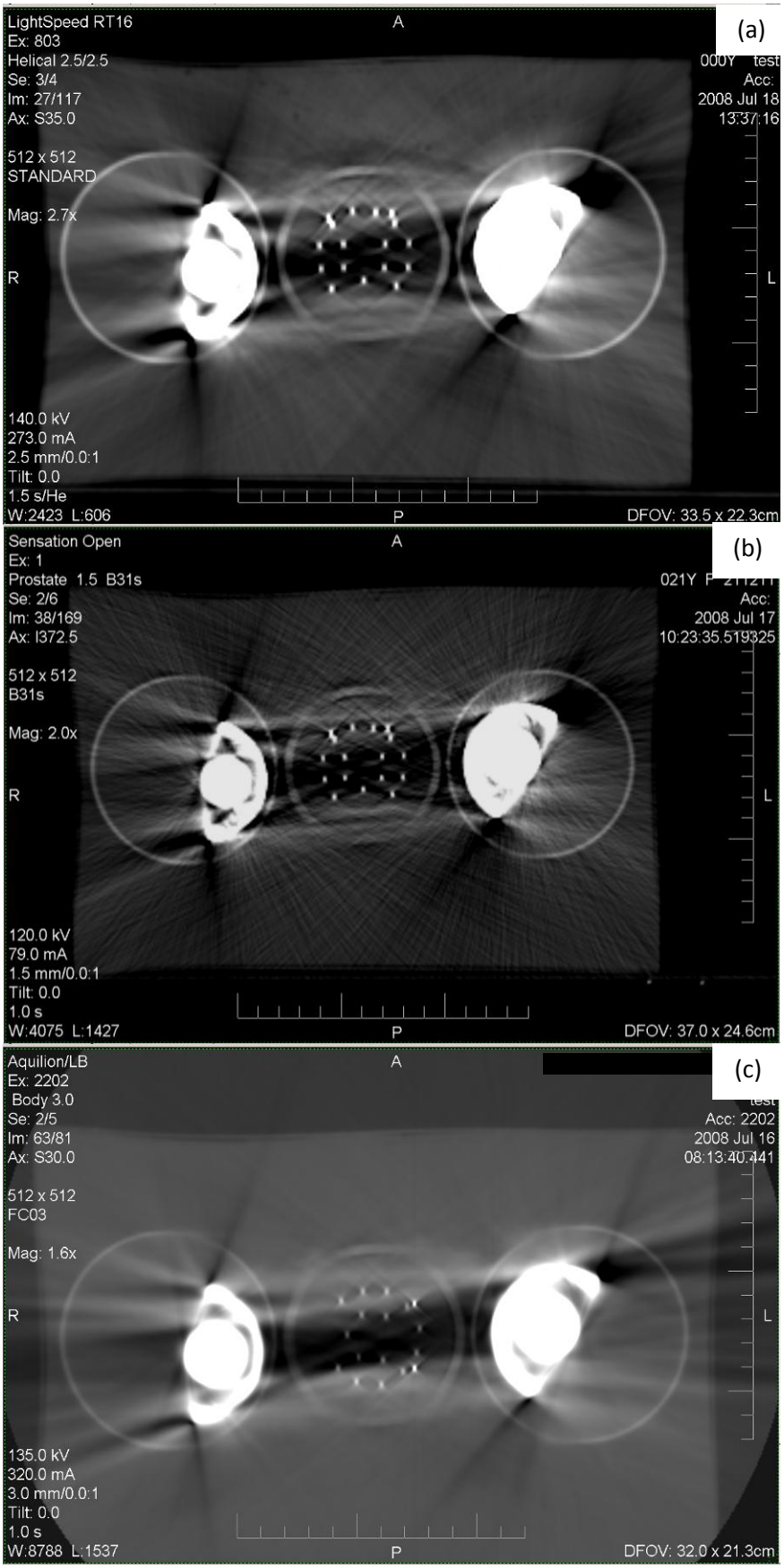

Figure 4-20: Reconstructed transverse CT slices though BLIP phantom showing femoral heads, acetabular cup, and needle implant. Implanted marker seeds are also visible (a) GE Lightspeed RT16, filter = standard, 2.5 mm slicewidth (b) Siemens Sensation Open, filter = B31s (c) Toshiba Aquilion/LB filter = FC03.

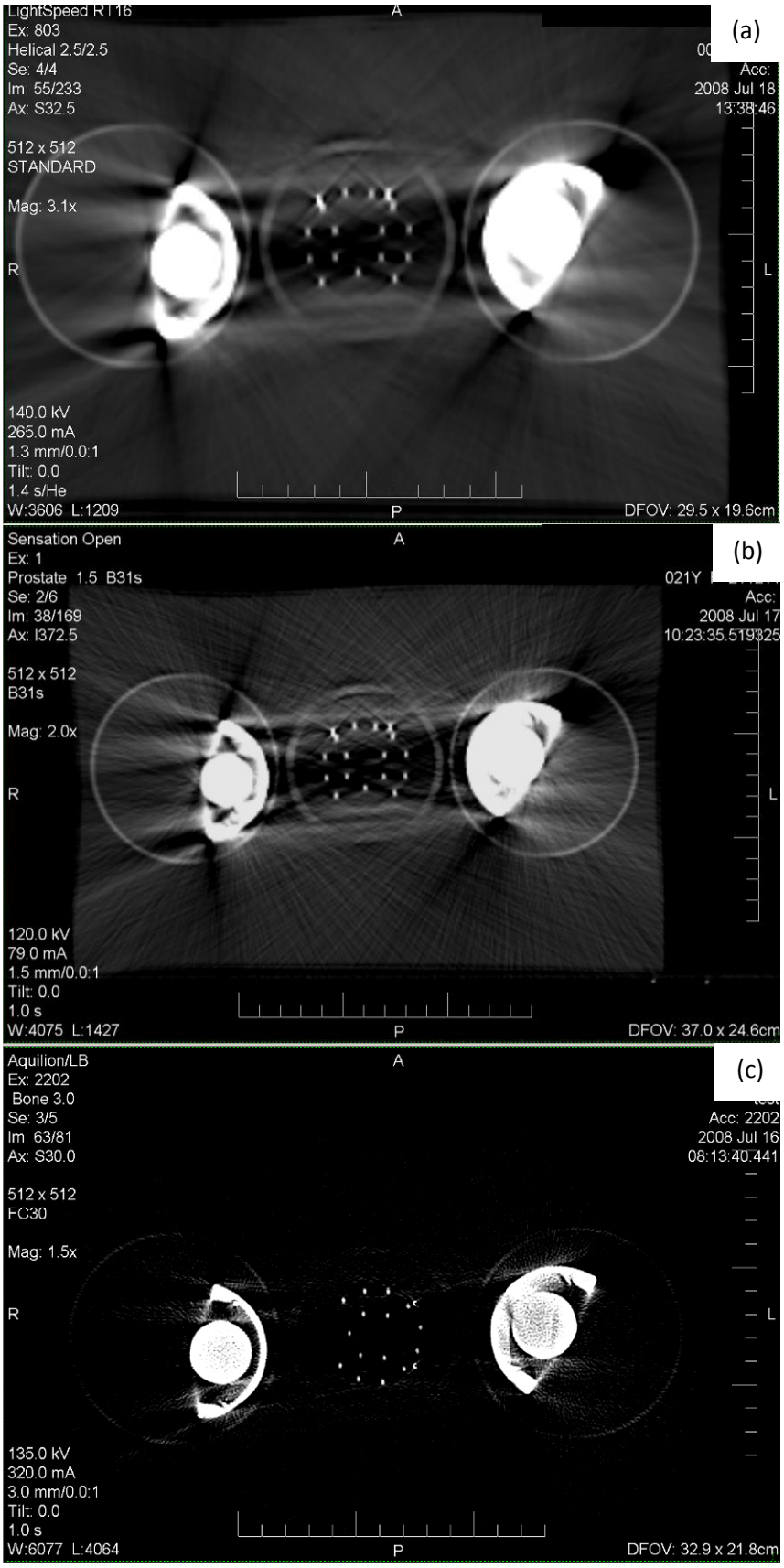

Figure 4-21**:** Reconstructed transverse CT slices though BLIP phantom showing femoral heads, acetabular cup, and needle implant. Implanted marker seeds are also visible (a) GE Lightspeed RT16, filter = standard, 1.3 mm slicewidth (b) Siemens Sensation Open, filter = B31s (c) Toshiba Aquilion/LB filter = FC03.

Using the manufacturer's recommended kVp, mAs, slice thickness and filter settings, shown in table 4-2, independent experienced observers at each centre subjectively rated images for clarity and detail. Images were later imported into the brachytherapy treatment planning system at SCGH and assessed by two experienced brachytherapy practitioners.

	GE	Siemens	Toshiba
kV	140	120	135
mA	Variable (up to 260)	Variable (up to 120)	Variable (up to 320)
Exposure time (s)	1.4	1	1
Slice thickness (mm)	1.3	1.5	2 and 3
SFOV	500	500	330
Filters - clinical	Standard	B31s	FC03

Table 4-2: CT kV, mAs, slice thickness and filter settings recommended by manufacturers to optimise metal artefact reduction in acquired images. SFOV = Scan Field Of View.

Images in figures 4-20 and 4-21 were selected to show the fiducial markers that typically would identify the prostate base, usually medial of the acetabular cups and femoral heads of hip prostheses. Distal needle tips were 15-20 mm superior of the markers, but still between the prostheses. The differing amount of streak artifact in the images acquired with each scanner's recommended settings is immediately apparent. In figure 4-20, the central needles in (c) are less well-defined than in (a) or (b), and accurate tip identification may be more challenging. In 4-20(c), gold fiducial markers also appear 'brighter' and with more streak artifact than needles. Slices in 4-20(c) were reconstructed by combining thinner slices, which can reduce streak artefact and improve signal to noise ratios and image contrast, but at the expense of spatial resolution. It appears that 4-20(b) yields greatest detail in the prostheses, but the image is grainy compared with (c), and less soft-tissue detail may be observed in a real patient. Poor soft tissue detail may reduce the accuracy of target definition in the brachytherapy treatment planning system and compromise the overall treatment efficacy. It is of note that 4-20(b) was obtained with the lowest kVp, mAs, and slice thickness, which may explain the increased graininess compared with (a) and (c). The Foley catheter is not visible in any of the images due to lack of contrast material in the catheter. Figure 4-20 suggests that none of the three manufacturers have significantly better metal artifact reduction techniques.

In figure 4-21, only the slice width was changed in (a), which has slightly improved the high contrast (spatial) resolution and has improved edge definition which is useful for

accurate needle identification, but less good for soft tissue definition. Thinner slices also reduce partial volume effects, which may be beneficial for accurate needle tip definition, to be discussed later. The disadvantage of thinner slices is that image noise is increased, and images may have reduced low contrast resolution (detrimental for soft tissue definition). In 4-21(b), no settings were changed; the settings were the 'standard' settings recommended by the manufacturer's applications specialist and used to obtain 4-20(b). Consequently, no improvement in image quality was observed for this scanner. In 4-21(c) a different filter, or kernel, was applied to the scan data. In general with all manufacturers, a higher number in the filter label (e.g. FC30 versus FC03) indicates reduced high-frequency attenuation in the filter, resulting in more noise in the image but with sharper edge detection because more high frequency components are left in the Fourier back-projection (see Appendix 2.3). The FC30 filter may be called a 'bone' filter, while the FC03 filter can be called a 'body' filter.

Considering figures 4-20 and 4-21, it may be observed that using any of the metal artefact reduction filters appears to reduce the low contrast soft tissue resolution and hence to reduce visualisation of the prostate itself. This may make it difficult to define an accurate target volume for treatment planning. The artefact reduction routines did generally perform well at improving detail within and very close to the prostheses – which, it could be claimed, is the true aim of metal artefact reduction filters.

However, the HDR brachytherapy practitioner requires as much detail as possible on high-density implanted markers and needles and the soft tissue brachytherapy target, and figures 4-20 and 4-21 make the imaging conundrum quite apparent: the question of how to reduce high-density material artifacts and simultaneously retain adequate soft tissue detail is not yet successfully addressed in many commercially available CT scanning systems. Given that even state-of-the-art techniques may only achieve a 20 – 40% reduction in metal artifact (Yu *et al.*, 2007), and that artifact reduction techniques may themselves introduce additional artifact into the image (Muller and Buzug, 2009) it may be advisable, for now, to avoid metal artifact filtration altogether.

4.5.2 Patient data from SCGH.

As noted in the discussion on MR scans, the BLIP phantom could only indicate what might be observed in actual patient images. Tissue inhomogeneities in patients and the added uncertainty of patient motion contribute to image differences when compared with a

simplistic and immobile phantom. However, phantom data do provide good insight into which scan settings may provide useful images in real patients. As well, a phantom could be scanned numerous times to optimise settings without concern for patient radiation dose, or comfort. Nevertheless, in many instances there is no substitute for real patient data.

GE HiSpeed LX/i. When HDR brachytherapy was first suggested for bilateral hip prosthesis patients at SCGH, the only available scanner was a single-slice GE HiSpeed LX/i, which had a minimum slice width of 1.0 mm and limited options for metal artifact reduction. Sample images acquired for EBRT treatment planning (figure 4-22) clearly showed a loss of soft tissue detail near the prostate. Significant streak artifact and signal deficit suggested the images may not be clinically useful for brachytherapy treatment planning. A 'bone' filter emphasised prostheses and worsened streak artifact at the expense of soft tissue detail, and a soft tissue filter did little to improve images. For this reason, in the first two bilateral hip patients only MR data were used and CT data were not acquired.

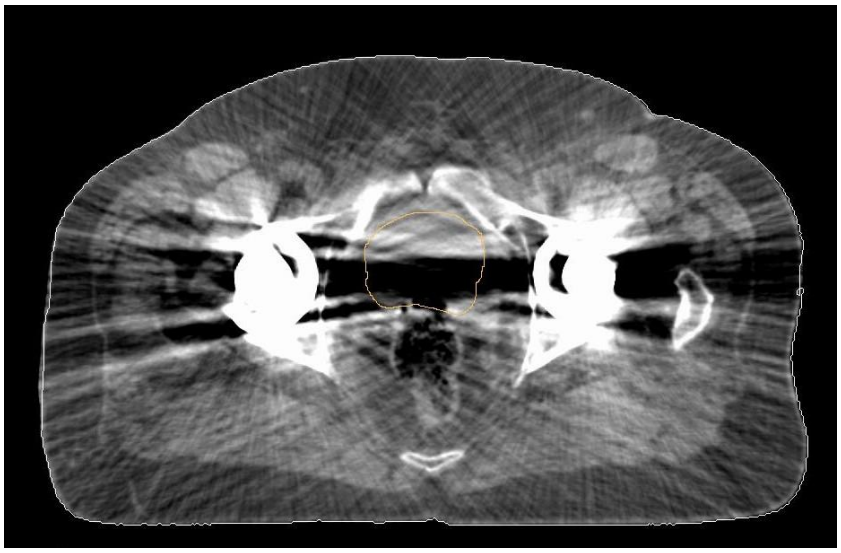

Figure 4-22: Bilateral hip EBRT patient (GE HiSpeed LX/i, 140 keV, auto mAs. FOV 502x502 mm, 512x512 array, 16 bit grey-scale. Target volume outlined in orange at centre.

GE Lightspeed VCT. After abandonment of the second bilateral hip patient's treatment due to poor MR image quality, a 64-slice GE Lightspeed VCT CT at SCGH was made available. Initially, the CT images were intended to be used to assist MR image interpretation, and it was a logistical challenge to co-ordinate and transport patients between theatre, 64-slice CT scanner, MR scanner, and brachytherapy treatment area while at the same time ensuring minimal interference with implanted needles. However, it was

expected the minimum slice width of 0.625 mm and more recent metal artifact reduction algorithms would improve implanted needle and target volume images.

The first bilateral hip prosthesis HDR prostate brachytherapy patient scanned in the GE Lightspeed VCT 64-slice scanner had a titanium stem in his left prosthesis and a cobalt-chrome stem in his right. Both cups were titanium. As discussed in Chapter 3, plastic needles were implanted and MR-compatible nitinol markers were used. CT datasets were extended to include the needle template's proximal face on the patient's perineum to enable confirmation of needle tip definitions by physical needle length measurement.

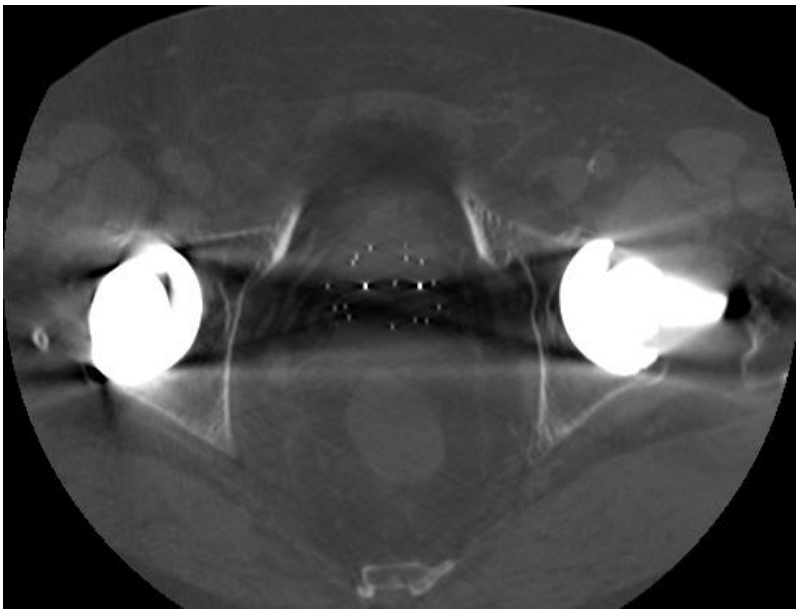

Figure 4-23: CT slice from bilateral hip HDR prostate brachytherapy patient at SCGH (GE Lightspeed VCT, 140 keV, auto mAs. FOV 302x302 mm, 512x512 array, 16 bit grey-scale, 0.625 mm slice, 'soft tissue' filter). Slice shows hip prostheses and associated artifact, and implanted needle markers. Fiducial markers visible as brighter spots near image centre.

As shown in figure 4-23, there was little difference in the amount of streak artifact from titanium (left hip) and cobalt-chrome (right hip) stems, although the titanium cups were perhaps the dominant feature. All of the 15 implanted plastic needles were clearly identifiable, and sufficient soft-tissue detail enabled target definition. The FOV dimension is limited by the need to include prostate, rectum, and needle template in an image dataset for treatment planning. With hindsight, a smaller FOV would have increased spatial resolution and may have assisted more accurate needle-tip identification by reducing partial volume effects. The patient was transferred to an MR scanner and the MR data were subsequently used for treatment planning. From the third patient onwards, the implanted

needle detail in CT images was deemed superior to MR images for treatment planning. As well, CT images were acquired comparatively quickly, an important consideration when patients were uncomfortable and recently recovered from general anaesthetic.

Only one treated patient presented with two stainless steel prosthetic hips. Stainless steel provides the greatest challenge for CT image quality as it has the highest linear attenuation coefficient of the three common prosthesis materials. A typical CT image slice obtained with the GE Lightspeed VCT 64-slice scanner is shown in figure 4-24 below:

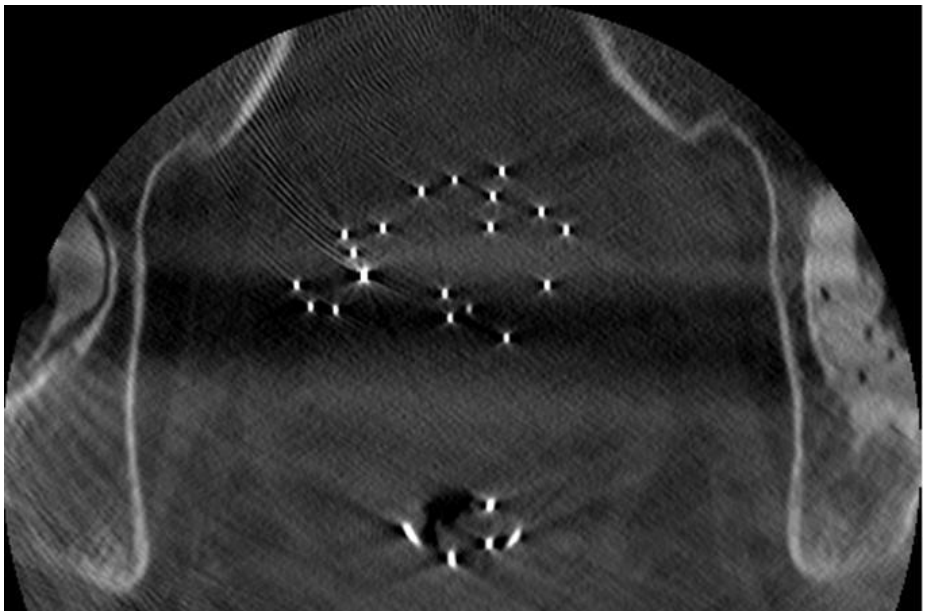

Figure 4-24: CT slice from 7th bilateral hip patient at SCGH (GE Lightspeed VCT, 140 keV, auto mAs. FOV 150x150 mm, 512x512 array, 16 bit grey-scale, 0.625 mm slice thickness, 'bone' filter). Needle markers and wire ribbon in rectal packing are visible. One implanted fiducial marker shows as brighter spot near image centre.

In figure 4-24 the prostate was not symmetric and needles were directed laterally on the patients right (our left) to ensure sufficient dosimetric coverage. Seventeen plastic needles were implanted. Images were acquired with a small FOV (150 x 150 mm) to reduce artifact from prostheses. Streak artifact from individual needle marker wires and an implanted gold fiducial marker was clearly visible. In contrast with images acquired from patient #3 (figure 4-23), a 'bone' rather than 'soft tissue' convolution filter was used. Unfortunately, loss of soft tissue detail was immediately apparent. The slice in figure 4-24 shows one implanted gold fiducial marker located approximately 5 mm inferior of the prostate base, but the prostate itself cannot be identified. Additional guidance to assist target delineation was obtained from the ultrasound volume study acquired in theatre.

By mid-2008 plastic needles were no longer available, and stainless steel needles were used for bilateral hip prosthesis HDR prostate brachytherapy patients. Tests with the BLIP phantom indicated the Lightspeed VCT 64-slice CT should still provide acceptable images for treatment planning, provided that a suitable ultrasound volume study was acquired for soft tissue detail. A sample CT slice that includes gold fiducial markers near the prostate base in patient #15, the first to be implanted with stainless steel needles, is shown below:

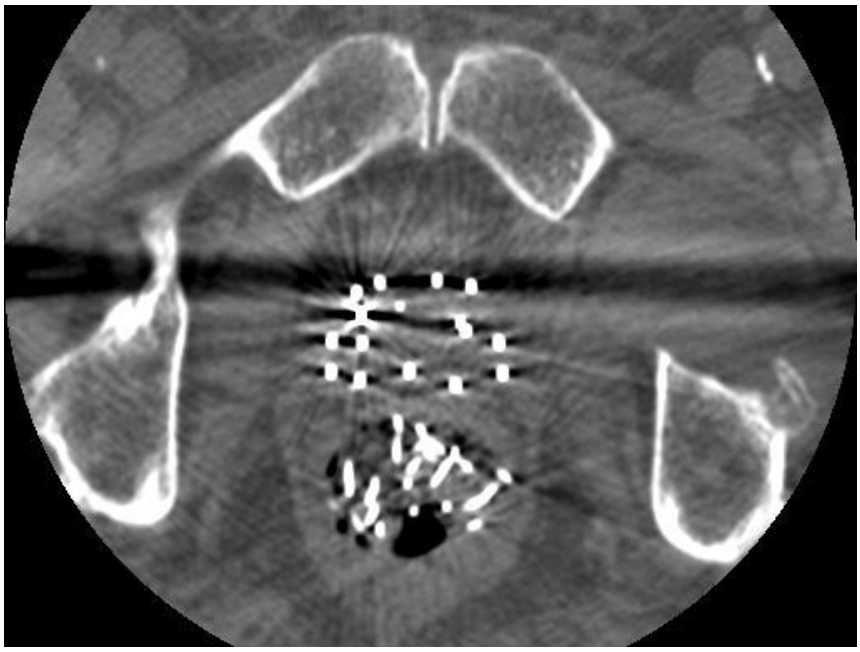

Figure 4-25: CT slice from 15th patient at SCGH (GE Lightspeed VCT, 140 keV, auto mAs. FOV 181x181 mm, 512x512 array, 16 bit grey-scale, 0.625 mm slice thickness, 'soft tissue' filter). Slice shows implanted needles, fiducial markers, and wire ribbon in rectal packing.

Figure 4-25 shows that with hip prostheses essentially excluded from the FOV, artifact was significantly reduced. However, increased artifact from stainless steel needles was immediately apparent compared with images of nitinol marker wires in plastic needles (see figure 4-24), and gold fiducial markers were less clearly distinguishable from needles. However, image windowing and levelling could be adjusted to accentuate soft tissue detail, and for target delineation the attending Radiation Oncologist placed more reliance upon the ultrasound volume study and fiducial marker locations.

Toshiba Aquilion LB. The original single slice GE HiSpeed LX/i in the Radiotherapy Department at SCGH was replaced in 2009 with a Toshiba Aquilion LB 16-slice scanner that provided 0.5 mm minimum slice width, 70 cm FOV, and helical scanning capabilities. Results from the phantom study described earlier were a contributing factor to machine

selection. By now, plastic needles and nitinol marker wires that were used to ensure MR imaging compatibility were no longer in use for bilateral hip prosthesis patients, and only stainless steel needles were used. Figure 4-26 shows a typical slice from this scanner.

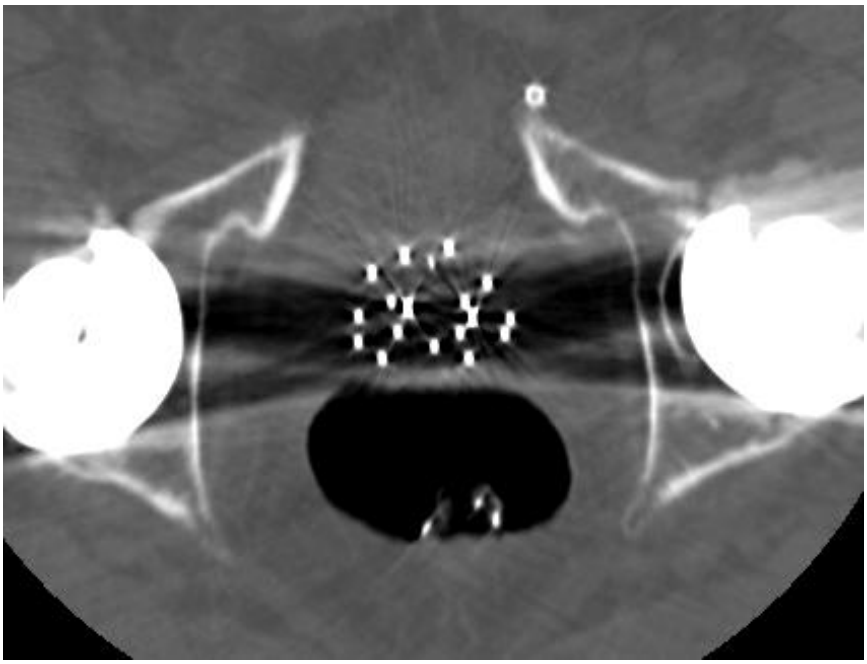

Figure 4-26: CT slice from 15th patient at SCGH (Toshiba Aquilion LB, 135 keV, 400 mAs. FOV 250x250 mm, 512x512 array, 16 bit grey-scale, 0.5 mm slice thickness, 'soft tissue' filter). Slice shows implanted needles, fiducial markers, and wire ribbon in rectal packing.

This patient's implanted prostheses were unfortunately included in the FOV, and artifact was significant. However, artifact from the stainless steel needles was reduced, and gold fiducial markers were more clearly distinguishable from needles when compared with the GE Lightspeed VCT image in figure 4-25. Note the large volume of gas in the rectum. As before, for target delineation the attending physician relied more upon accompanying ultrasound volume study data and fiducial marker locations.

Summary. Plastic needles are recommended wherever possible, due to significantly reduced artifact and image degradation. Many centres already use plastic needles for all prostate HDR brachytherapy procedures. However, a clear preference for plastic needle implants is difficult to establish, since stainless steel needles are typically less flexible and less prone to bending (straighter needle paths may also be less difficult to identify in treatment planning images). As shown in figure 4-25, comparatively recent CT scanners can provide acceptable images for treatment planning purposes even with stainless steel needles, particularly when used in combination with trans-rectal ultrasound volume study

data. Some manufacturers supply titanium implant needles, which may cause less image artifact. However, for the SCGH afterloading system at least, concern for potential tissue injury due to prolonged insertion and 'micro-motion' of sharp trocar point tips has discouraged use of the titanium needles for standard fractionated treatments.

4.5.3 Windows and levels for needle and fiducial marker identification.

A study of 10 randomly selected SCGH patients undergoing HDR brachytherapy treatment with stainless steel needle implants established appropriate CT window levels and widths to reduce uncertainty in needle tip identification and to aid accurate location of implanted fiducial gold markers.

For each patient, the average CT number in a region of interest within an HDR needle or a fiducial marker was recorded. Needles were randomly selected and the average CT number was recorded along each needle in randomly selected CT slices. Marker seeds were physically smaller (4.5 mm long), and typically were visible in only two or three slices; CT numbers in all seeds in each patient were recorded. The average CT number for needles was determined, and the standard deviation σ was calculated. Table 4-3 shows the results:

Needle HU			Gold seed HU		
Patient	Average	Std Dev	Patient	Average	Std Dev
1	3407	242	1	15336	1336
2	3740	461	2	12102	1315
3	3666	622	3	12894	1743
4	3928	336	4	12987	1040
5	3722	348	5	11783	224
6	3590	289	6	14782	1863
7	4485	429	7	16608	1776
8	3547	732	8	13527	1427
9	3310	291	9	9756	1084
10	3655	454	10	10564	810
Average	3705	420	Average	13034	1262

Table 4-3: CT HU data from 10 patients with implanted stainless steel needles and gold seed fiducial markers. Average needle and gold seed HU, and standard deviations.

As described in chapter 3, optimum detection sensitivity is afforded by setting the window level to the average CT number of the object of interest. Assuming that CT numbers are distributed normally about a mean value, 99.7% of needles will be visible in a window of

width 6σ. Table 4-3 shows that stainless steel needles are easily separable from normal tissue, and that gold fiducial markers can be highlighted by selecting a level and window to match the marker's CT numbers. Implanted plastic needles have a reduced average CT number compared with stainless steel needles – the main contributor was the custom-made nitinol wire marker that provided sufficient contrast for detection in fluoroscopic images.

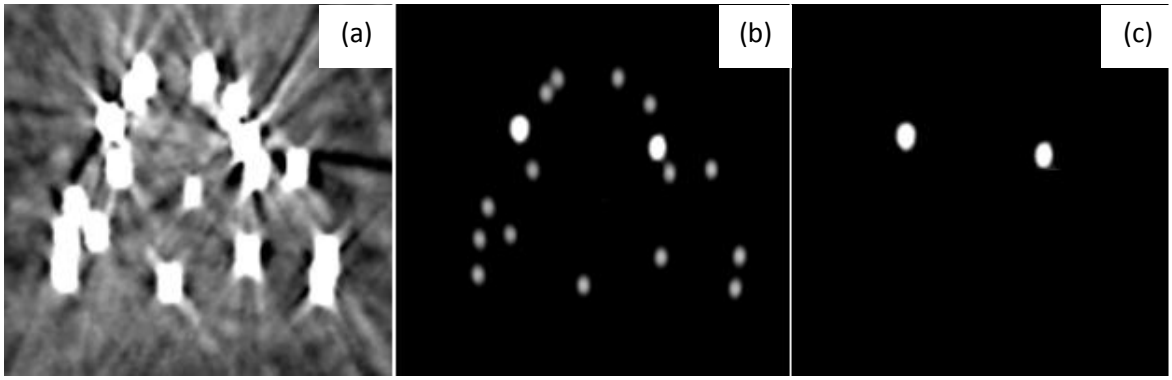

Figure 4-27: CT level and window settings to emphasise different features in acquired data (a) default, level 40, window -200 – 1600 HU, (b) steel needle, level 3700, window 2000 – 5400 HU, (c) gold seeds, level 13000, window 5000 – 21000 HU.

Figure 4-27 demonstrates how different features in a CT slice were highlighted by appropriate window level and width selections; figure 4-27(a) shows the 'default' window level and width displayed in a TPS. The image shows prostate tissue, 15 implanted stainless steel needles, and two gold fiducial markers. The catheterised urethra is visible via a mild contrast agent. In figure 4-27(b), implanted needles were emphasised by setting the level near 3700 HU, and was useful when tracking needles that converged or crossed, and particularly to identify needle tips with high accuracy. By setting the level to 13000 HU as in figure 4-27(c), implanted fiducial markers were easily separated from needles.

4.5.4 Distal needle tip image accuracy.

Accurate distal needle tip identification is essential for HDR prostate brachytherapy treatment planning and subsequent delivery, as the distal needle tip is the reference point from which all Ir-192 source dwell positions are located. Others (Kim *et al.*, 2004) investigated the dosimetric impact of CT slice thickness in HDR prostate brachytherapy treatment. In a typical implant containing 16-18 needles, when needle tips were randomly distributed in a 2 mm CT slice the dosimetric error was approximately 0.7% compared with dose delivered with all needle tips at the distal end of the 2 mm CT slice. They found

a 3 mm slice thickness increased the dosimetric error to 1.1%. Kim *et al* concluded the greatest dose error and variability occurred at the prostate base and apex. However, in suggesting the use of 3 mm CT slice thickness, Kim *et al* recognised the trade-off between dosimetric accuracy and the impact of increased accuracy on clinical workload (particularly the requirement to outline targets and organs at risk on multiple slices).

In any given voxel (pixel element with depth *z*) the observed CT number is

$$HU = 1000\ (\mu_{pixel} - \mu_{water}) / \mu_{water} \qquad (3.1)$$

where μ_{pixel} is the linear attenuation coefficient (LAC) of the material contained within the voxel. When a voxel contains several different materials, the LAC is the mass-weighted average of constituent material LACs:

$$\frac{\mu}{\rho} = \sum_i w_i \left(\frac{\mu}{\rho}\right)_i \qquad (3.2)$$

where w_i is the fraction by weight of element *i* contained within the voxel. To estimate the CT number in voxels along a brachytherapy needle, a simplified model was developed in which a square CT pixel with sides matching the nominal needle diameter was used. Slice thicknesses of 0.6, 1, 2, and 3 mm were simulated. The needle tip was advanced through a voxel and the effective LAC and CT number were calculated. The effective LAC, and therefore the observed CT number, depends upon the effective CT energy. Using a CIRS Model 062 Electron Density Reference Phantom (CIRS, 2007), the effective energy in keV is given by

$$keV_{effective} = a.CTU^{-1} + b + c.CTU + d.CTU^2 \qquad (3.3)$$

where CTU is the observed CT number for the standard CIRS Dense Bone Insert, and coefficients a = 134785.7, b = -177.545, c = 0.151804, and d = -3.78317×10^{-5}. For the nominal 135 kVp energy routinely used for prostate HDR brachytherapy patients at SCGH, the calculated effective energy was 66 ± 4 keV.

Stainless steel needles. Needles used for later patients at SCGH were 17-gauge (1.47 mm OD, 0.203 mm wall thickness) stainless steel, with a 2.3 mm pencil tip. Using the effective CT energy, and typical stainless steel composition data from the NIST XCOM database (*http://physics.nist.gov/PhysRefData/Xcom/Text/intro.html*), the LAC of stainless steel was estimated to be 1.01 ± 0.12 cm^{-1}. Surrounding tissue was assumed to be water-equivalent, with LAC set to 0.199 ± 0.004 cm^{-1}. Calculations were complicated by the tapered needle tip, the presence of a stainless steel obturator, and air gaps in the needle (the LAC of air is essentially 0). All of these factors were included in the model, and the expected CT number versus distal needle tip location within a voxel is plotted in figure 4-28.

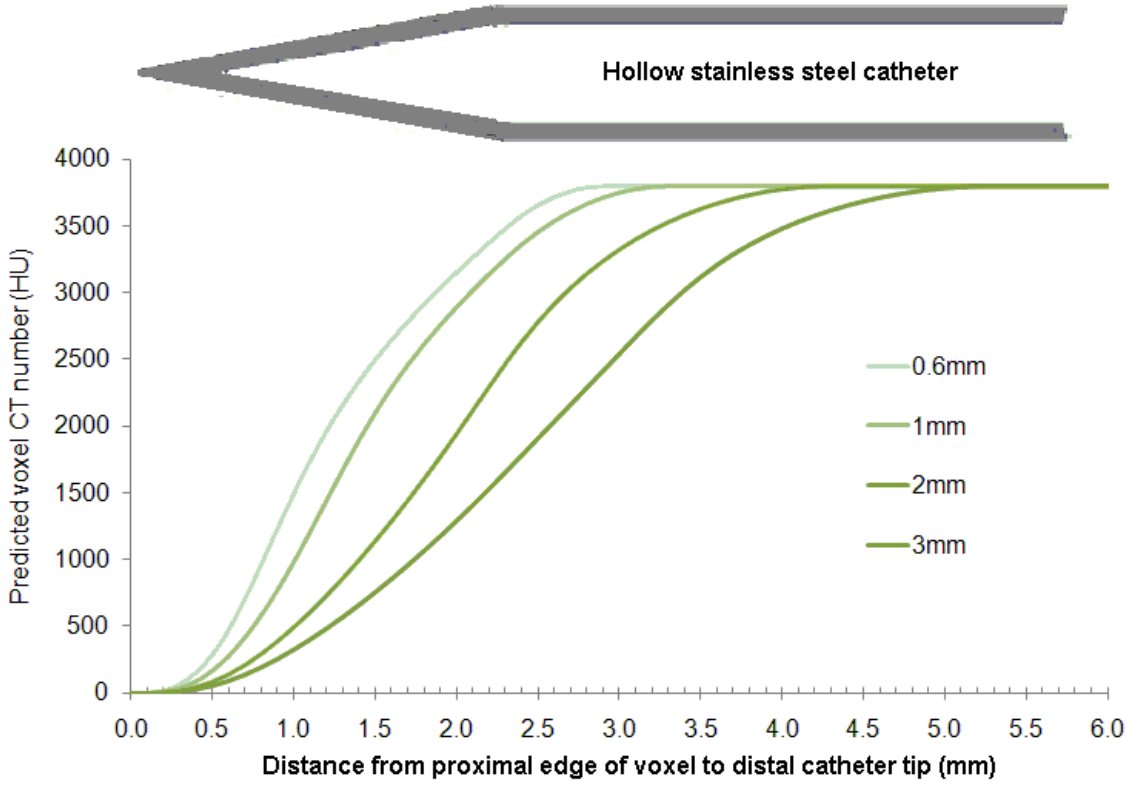

Figure 4-28: Calculated CT number (Hounsfield Units) as a function of distal needle tip location within CT voxels of thickness 0.6, 1, 2, and 3 mm, for a hollow needle.

In figure 4-28, when the proximal edge of a voxel was at 0.0, the needle tip was just outside the voxel. The predicted CT number for a solid stainless steel needle was approximately 3939 HU, and for a hollow needle was 3799 HU, indicating the dominant contribution of stainless steel to the voxel LAC. The predicted range of HU values (3799 ± 478 HU) takes into account the uncertainty in effective CT energy, and compares remarkably well with the clinically observed value in table 4-3 (3705 ± 420 HU).

Measurements of the needle's internal length were made with a 0.64 mm diameter wire that matched the source wire diameter. The wire was advanced to the distal end of the needle, a plastic hub was clamped to the proximal end of the wire where it emerged, and the tip – hub length was measured. The internal distal tip was -1.5 ± 0.2 mm from the external distal tip. This internal point is the reference point from which the Ir-192 source location is measured. For 2 mm CT slice thickness with minimum CT window set to 2000 HU, the point at which the image became black corresponded approximately to the physically measured needle tip. For all tested slice thicknesses, with minimum CT number set to 2000 HU, the apparent distal tip matched the actual internal distal tip to within ± 0.7 mm. According to Kim *et al*, this ensures dosimetric accuracy better than 0.7%.

Comparison with CT-imaged needles. Tests of an appropriate CT HU number level and window were made with a custom-made phantom shown in figure 4-29. It contained 5 needles set onto laminated graph paper with the tips 40.0 mm from one marker wire, and 100.0 mm from a second wire (the separation between wires assisted to confirm dimensionally accurate image reconstruction). The graph paper was glued to a slab of 'solid water', and a polystyrene border was glued to the slab. Needles were plugged to prevent water ingress, and then covered with water. A slab of solid water was placed on top of the polystyrene, taking care to exclude air bubbles. The entire assembly was placed onto 2 cm of solid water, and 2 cm of solid water was added on top.

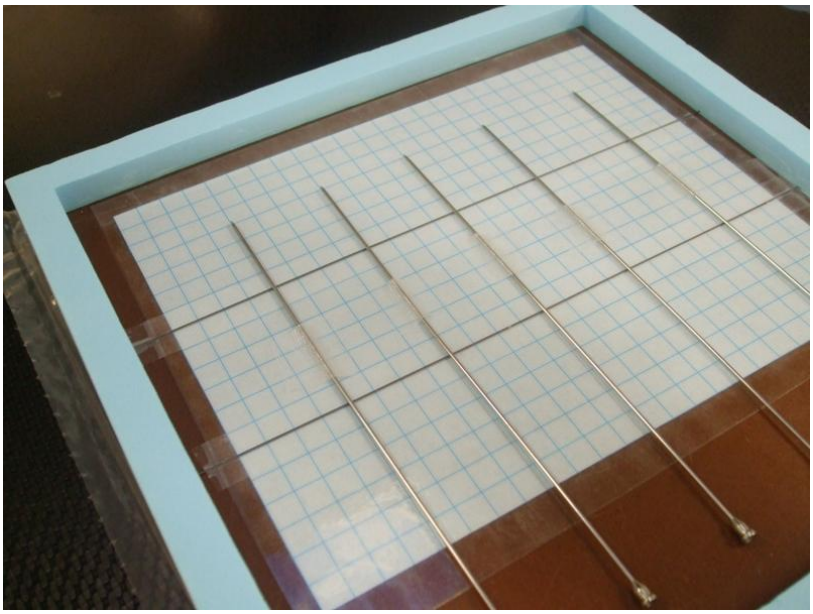

Figure 4-29 Needle tip phantom containing five stainless steel needles. Plugged needles are aligned with graph paper, and covered with water. See text for detail.

The phantom was placed on the CT table with marker wires aligned to CT lasers, and needles aligned along the CT bore. The phantom was then rotated so that the five needle tips spanned 2mm in the axial direction in 0.5 mm steps. The FOV was similar to that used in patient scans and images were acquired with typical patient scan settings (135 kV, auto mA, 2 mm slice thickness). When the CT window was set to visualise soft tissue (-200 to +400 HU), the apparent needle length was 1.7 ± 0.2 mm longer than the physical needle length. In laterally-placed needles, the average CT number in the phantom was slightly higher than that observed in patient measurements. In patients the x-ray beam penetrates more tissue than modelled in the 5 cm-thick phantom, and the CT beam is hardened, the effective linear attenuation coefficient is reduced, and observed CT numbers are slightly reduced in a patient compared with the phantom.

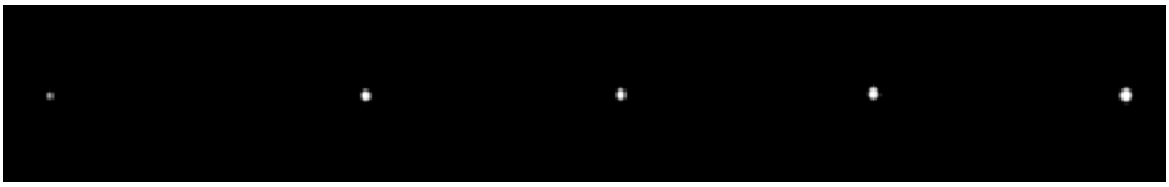

Figure 4-30: CT slice containing all needle tips, from near-zero penetration (left) to 2.0 mm penetration (right) into slice.

Figure 4-30 shows a CT slice that contains all five needle tips. As demonstrated by the increasing visibility, tips penetrated further into the slice from left to right. The central needle tip was at the mid-point of the CT slice. Observed CT numbers for each needle tip were compared with calculated CT numbers. As shown in figure 4-31, agreement between predicted and observed CT numbers is satisfactory.

The minimum CT number window value was then adjusted until the measured distance between a reference wire and the needle tip matched the physical distance on the phantom (40.0 mm). Best agreement was achieved with a minimum CT number of 2000 ± 100 HU. The recommended CT window for accurate needle tip identification therefore spans approximately 2000 – 5600 HU. In practice, it was the minimum CT number value that had greatest impact upon the visualised needle tip location. It was found that the maximum CT number made little difference to observed needle tip locations.

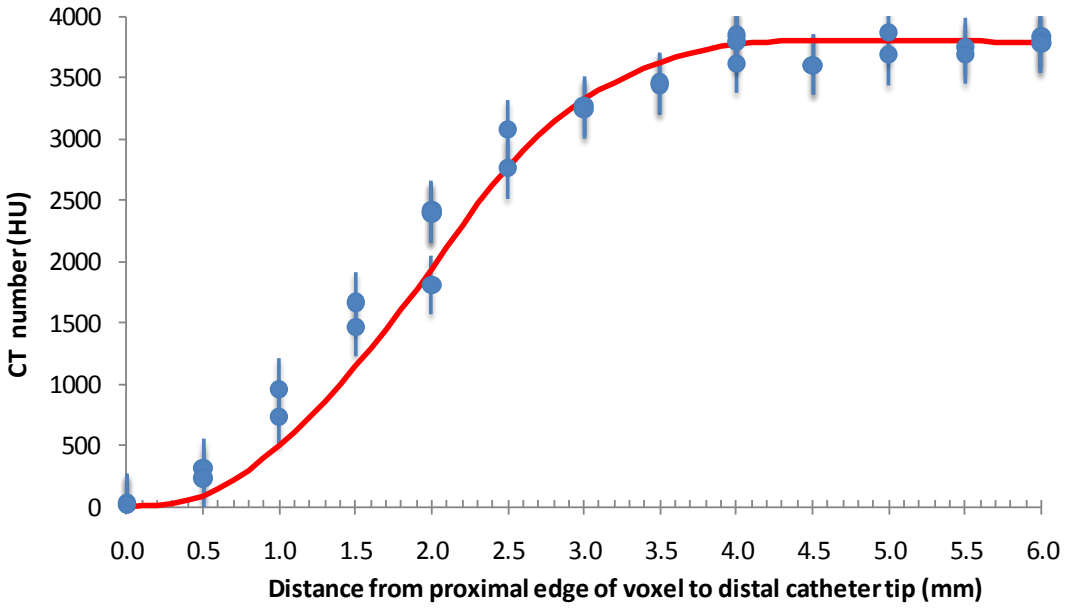

Figure 4-31: Calculated (red solid line) and measured (blue circles) CT number (HU) as a function of distal needle tip location within CT voxels 2 mm thick. Hollow needle.

Chapter 5 . Inter-fraction needle displacement.

In HDR prostate brachytherapy treatments, needle locations recorded in treatment planning images form a baseline dataset for treatment planning and subsequent treatment. At each treatment fraction, observed needle locations can be compared with baseline locations and can be modified to correct observed displacements.

The potential for needle movement was recognised some time ago, when Damore *et al* (2000) showed that by virtue of the implant geometry, needles tended to move caudally, i.e. out of the patient. They observed the greatest movement occurred between second and third fractions in their 4-fraction treatment course, and at their institution nearly 40% of treated patients required either manual adjustment (needles were manually pushed into the patient) or treatment plan modification to ensure adequate dosimetric coverage of the target volume. Damore *et al* did not measure needle displacement between acquisition of treatment planning CT images and first treatment fraction (SCGH do). Kiffer *et al* (2003) later demonstrated that needle displacement in the lateral and anterior-posterior directions was within ±0.3 mm, and that dosimetric changes due to this displacement were negligible.

Typically the template devices used to guide needle implantation remain in place after surgery, and hold needles sufficiently securely during subsequent treatment fractions that the needles do not move relative to each other (Hoskin *et al.*, 2003). Usually templates were stitched to the perineum. As needles often protrude 50-60 mm from the perineal surface, patients usually – but not always (Yoshida *et al.*, 2006; Yoshida *et al.*, 2010) – were confined to bed for the duration of treatment to avoid injury or needle damage.

Various methods were proposed to compensate for needle movement, including CT imaging before each fraction to check displacement (Mullokandov and Gejerman, 2004), or advancing needles 10 mm beyond the prostate during implantation (Hoskin *et al.*, 2003), and replanning treatments when needles were displaced (Damore *et al.*, 2000). Each method, including that used at SCGH, has advantages and disadvantages. Adding a margin around the treatment volume means small displacements can be tolerated and adjustments may not be required as often. However, more normal tissue may be treated. Advancing needles 10 mm beyond the prostate and adjusting the source train origin when needles displace inferiorly is a relatively simple but potentially time consuming procedure. Care

should be taken when selecting an acceptable displacement before source positions are adjusted. However, the amount of acceptable needle movement is not well established.

5.1 Needle-shift in HDR prostate brachytherapy.

At SCGH, needle movement was quantified in every treatment fraction delivered to every patient since the first treatment in 2002. In our own study (Tiong *et al.*, 2009) we observed that in a total of 273 delivered treatment fractions, only 19 fractions exhibited caudal needle movement of 1 mm or less. As discussed earlier, a shift of 1 mm in HDR source location can cause a significant difference between expected and actually delivered dose. Needle displacement was visualised via fluoroscopy, compared with baseline data, and corrected by advancing implanted needles and template as a unit, with adjustments stabilised by a fixation device. Our method is quick and simple and can be used to verify needle locations before each fraction. We sought to identify an acceptable tolerance for needle movement using Tumour Control Probability modelling, and were then able to identify in a population of patients treated at SCGH, the number with needle displacements that exceeded this tolerance. We established a range of needle motion that could be tolerated before needles should be re-positioned.

5.1.1 SCGH needle movement study - stainless steel needle implants.

Needle movement data from all patients with prostate cancer treated using brachytherapy at our centre with stainless steel HDR brachytherapy needle implants from January 1 to December 31, 2007, were audited. Patients were selected for HDR brachytherapy if they had high-grade localized disease and were medically fit to receive, and benefit, from treatment. The HDR brachytherapy needle implant was undertaken in theatre by appropriately trained clinicians, and treatment was delivered in three fractions. The silicone Syed-Neblet templates were supplied by AOS and were the same type as used by Damore *et al* (2000) and Kiffer *et al* (2003). Similarly, stainless steel 17 gauge needles were supplied by AOS, as were plastic needles used for bilateral hip prosthesis patients. Damore *et al* used stainless steel needles from AOS, while Kiffer *et al* used plastic needles reportedly supplied by Best Industries (Springfield, VA, USA). Given that SCGH used implant kits from the same suppliers as the groups of Damore and Kiffer, it is reasonable to anticipate similar experiences with the kits in this study.

Needle adjustment. Needle displacement was examined and corrected before each treatment fraction. A digitally reconstructed anterior-posterior (AP) baseline image was produced from treatment planning CT images (rotated to approximate the needle orientation observed at treatment). Before each treatment, with the patient in treatment position, plane AP radiographs were acquired with a C-arm fluoroscopy unit.

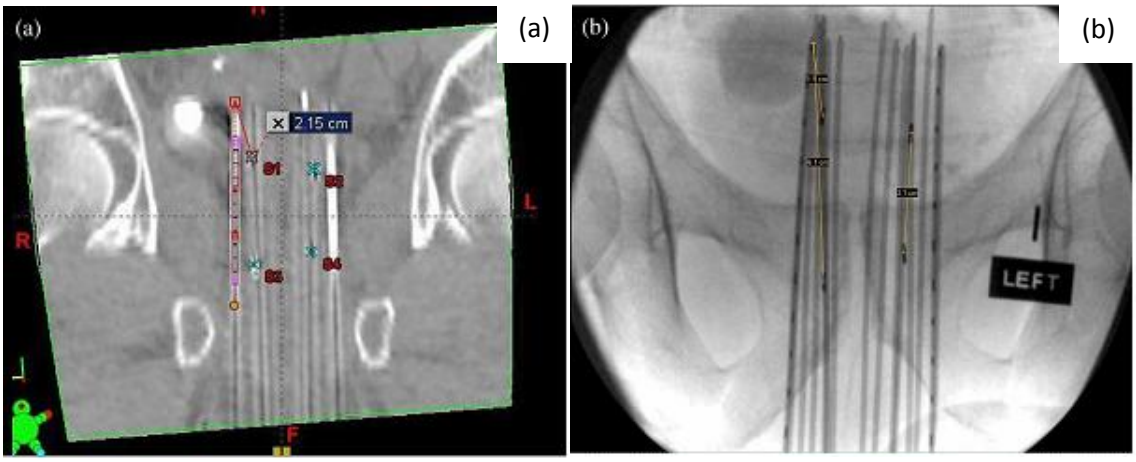

Figure 5-1: (a) Baseline distance between needle tips and implanted markers on reconstructed CT images oriented to match needles in patient and (b) on AP radiographs before treatment.

At SCGH we found that implanted needles did not move within the silicone template, in agreement with the findings of Hoskin *et al* (2003). Given this stability, the distance between two needle tips located on either side of the urethra, to four implanted markers, was measured (figure 5-1). Unacceptable differences between baseline and pre-treatment data were corrected. A holding device fixed needles and template in position (figure 5-2).

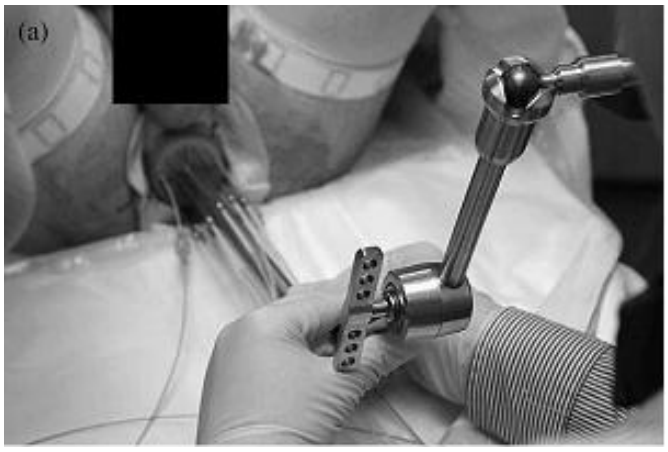

Figure 5-2: Needle displacement correction in a patient undergoing treatment, with manual adjustment of the template and needles being fixed in place by holding device.

Adjusted needle positions were re-checked with a plane radiograph and readjusted if necessary. This check was repeated before each treatment fraction. Actual measurements from needle tips to fiducial markers for all fractions were prospectively collected for all patients treated in 2007. The coordinates of needle tips and fiducial markers on treatment planning CT images were stored in the TPS. The caudal needle displacement was calculated before each treatment (figure 5-3).

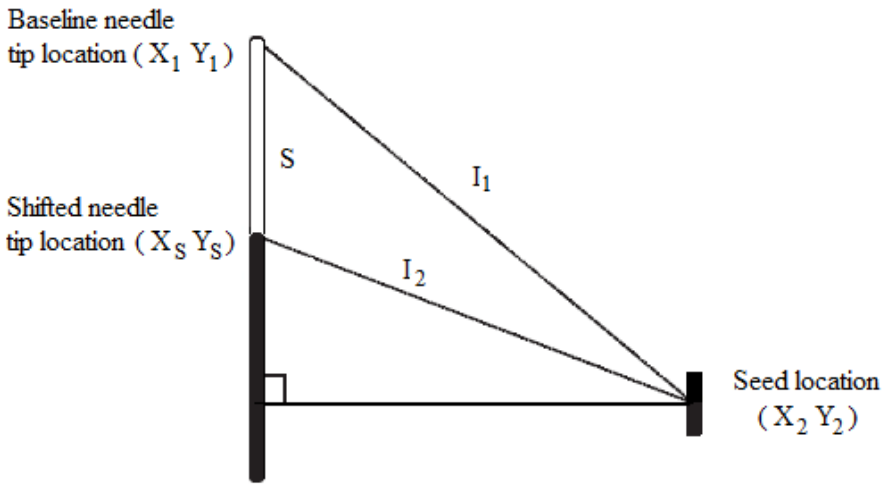

Figure 5-3: Method of deriving caudal needle shift (*S*) from data measured in high–dose rate needle implants of prostate gland. Note (X_S,Y_S) is unknown, I_1 and I_2 are measured.

With reference to figure 5-3, the observed caudal shift *S* was

$$S = (Y_1 - Y_2) - \sqrt{I_2^2 - (X_1 - X_2)^2} \qquad (5.1)$$

where I_1 is the baseline distance from needle tip to seed midpoint; I_2 is the distance from needle tip to seed midpoint measured before treatment, (X_1,Y_1) is the baseline needle tip coordinate and (X_2,Y_2) is the marker seed coordinate recorded in the TPS. The expression in eqn 5.1 is accurate for caudally aligned needles with zero rotation in the AP plane. Clinically, rotation corresponds to an apparent shortening of distances due to inaccurate replication of the patient lithotomy position at implant. Maximum rotation (approximately 15°) introduced a distance error of about 1 mm, but in clinical practice, rotation was corrected to within a few degrees and distance error was less than 0.3 mm.

From January 1 to December 31, 2007, 91 patients with prostate cancer were treated with stainless steel needle implants, and 273 fractions were delivered. The maximum observed caudal shifts were 13 mm in the first fraction, 22 mm in the second fraction and 27 mm in

the third fraction, all in different patients. As summarised in table 1, the mean caudal displacement before adjustment in all fractions was 5.4 mm (SD 3.3 mm). Greatest average displacement was measured before the third fraction (mean 6.4 mm; SD 4.2 mm), suggesting needles become progressively less stable as treatment progresses. After adjustment, the mean caudal displacement was reduced (mean 1.2 mm; SD 1.7 mm). Craniocaudal stretching of the prostate, which mainly affected the relative location of fiducial markers at the base, can be problematic. This error can be lessened by measuring distances between markers to quantify stretch, and exercising judgment when interpreting measured displacements against fiducial markers at the base.

Statistical comparisons in this analysis were made using SPSS for Windows (v11.5.0, SPSS, Chicago, IL). A two-tailed t test was used to compare means, chi-square test to compare proportions, and Wilcoxon rank sum test to compare medians. The level of significance chosen was 0.05.

	Caudal displacement (mm)			
Timing	Fraction 1	Fraction 2	Fraction 3	All fractions
Before adjustment				
Mean	4.5	5.6	6.4	5.4
SD	1.7	3.6	4.2	3.3
After adjustment				
Mean	1.7	1.1	0.8	1.2
SD	1.3	1.9	1.7	1.7

Table 5-1: Caudal catheter shifts relative to marker seeds implanted into prostate, before and after adjustment each treatment fraction.

It may be observed in table 5-1 that the ‘after adjustment’ mean for first fractions was larger than for subsequent fractions. This may be due to a tendency to accept needle displacements in the first treatment fraction that were close to tolerance, due to the lengthy duration of preparation and patient set-up for first treatment fractions. Of 91 patients treated, without needle adjustment 82.3% of fractions had displacements greater than 3 mm, compared with 12.2% of fractions after manual adjustment.

An average of 1.2 adjustments (range 0–3 adjustments) per fraction was required to reduce needle displacements before treatment. This may be due to uncertainty in the amount of pressure on the needle template required to advance needles sufficiently far into the

prostate. Anecdotal evidence suggested that over-insertion due to excessive pressure was more difficult to correct than re-application of pressure to advance needles slightly further into the patient. A conservative approach ensured that over-insertion was less likely to occur, but dictated that more adjustments were required.

Clinically determined needle displacements. It was standard practice at SCGH to estimate caudal needle shifts by analysing the difference (I_2-I_1) for each needle tip – fiducial marker distance in baseline versus treatment images, as shown in figure 5-3. By analysing needle and marker locations in each of the 91 patients treated at SCGH in 2007, average baseline separations between needle tips and markers were determined, and compared with the more accurate calculation given in eqn 5.1. Figure 5-4 shows a reference needle and four fiducial markers, labelled *Adjacent Base*, *Adjacent Apex*, *Far Base* and *Far Apex*. Seed labels relative to right-side needles mirror those shown.

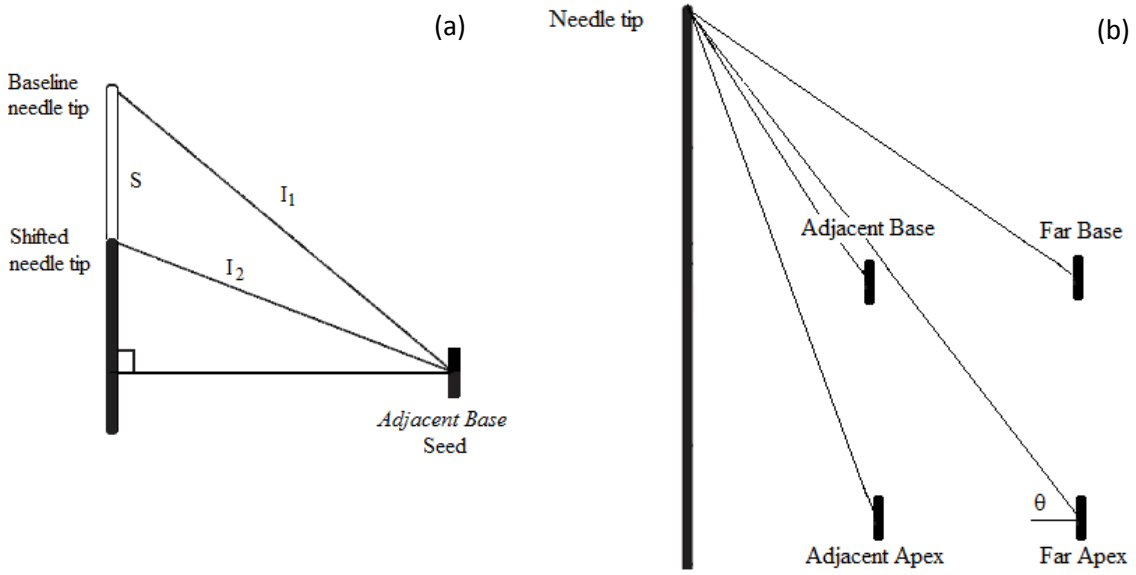

Figure 5-4: (a) method of deriving caudal needle shift, *S*, for an *Adjacent Base* seed (b) labelling of markers for reference needle. Right-side needle definitions mirror those shown.

From figure 5-4(b), it can be deduced that the difference (I_2-I_1) is least sensitive to caudal shift *S* measured to *Far Base* markers, as the needle and hence the caudal shift *S* acts like the shorter side in a Pythagorean triangle. Similarly, the difference (I_2-I_1) is most accurate for caudal shifts measured to the *Adjacent Apex* marker, as the needle acts as the longer side of the triangle. Table 5-2 lists average distances and standard deviations from needle tip to each fiducial marker for the 91 patients treated in 2007. It lists the average angle

subtended by each marker to the reference needle, and also lists differences between the (I_2-I_1) approximation and the more accurate equation given earlier.

	Fiducial Marker location			
	Adjacent Base	Far Base	Adjacent Apex	Far Apex
Baseline values				
Average Length I_1 (mm)	22	35	50	57
SD (mm)	8	6	10	10
Average Angle (degrees)	72	51	82	61
Fraction 1				
Caudal shift (mm)	4.5			
Mean shift (I_2-I_1)	4.4	3.4	4.5	4.0
SD	0.2	0.2	0.1	0.1
(I_2-I_1)/sin(θ)	4.6	4.4	4.5	4.6
SD	0.2	0.3	0.1	0.2
Fraction 2				
Caudal shift (mm)	5.6			
Mean shift (I_2-I_1)	5.4	4.2	5.5	5.0
SD	0.1	0.3	0.1	0.2
(I_2-I_1)/sin(θ)	5.7	5.4	5.6	5.7
SD	0.2	0.4	0.1	0.2
Fraction 3				
Caudal shift (mm)	6.4			
Mean shift (I_2-I_1)	6.2	4.8	6.3	5.7
SD	0.2	0.3	0.1	0.2
(I_2-I_1)/sin(θ)	6.5	6.2	6.4	6.5
SD	0.1	0.3	0.1	0.2

Table 5-2: Caudal needle shift relative to marker seeds. I_1 is baseline distance to marker, I_2 is distance measured after caudal shift included. Also shown is caudal shift $S = (I_2\text{-}I_1)/sin(\theta)$, where θ is average angle between fiducial marker and needle tip. Eqn 5.1was used to determine the calculated Caudal shift.

For an average patient, the simple (I_2-I_1) approximation was within 0.2 mm of the caudal shift calculated using eqn 5.1 for *Adjacent* markers in all treatment fractions, but was in error by up to 1.6 mm for *Far* markers, indicating that experience is required and

judgement must be exercised when declaring a required shift. Using the average angle θ subtended by needle tips to each fiducial marker, a correction factor $1/sin(\theta)$ was applied to the measured difference (I_2-I_1). The correction improved average agreement between calculated and measured caudal shifts to within 0.2 mm for all markers in all treatment fractions. SCGH recently implemented the more accurate expression $S = (I_2-I_1)/sin(\theta)$ to assess needle shifts in a spreadsheet application on a PDA device in the treatment room. Anecdotally, the application also reduced inter-observer variation in declared needle shifts.

In summary, the simple $S = (I_2-I_1)$ approximation had sufficient accuracy if *Adjacent* marker shifts were more heavily weighted in the assessment of caudal displacement to determine the necessity, and magnitude, of subsequent corrective actions. However, the more accurate $S = (I_2-I_1)/sin(\theta)$ model is preferred if implemented efficiently, for example on a spreadsheet application on a PDA (personal digital assistant) in the treatment room.

5.1.2 SCGH needle movement study - bilateral hip patients with plastic needles.

Needle movement data from all bilateral hip prosthesis patients with prostate cancer treated at SCGH using brachytherapy with plastic needle implants were audited. As for stainless steel implants, needle displacement was examined and corrected before each treatment fraction. As before, standard procedure at SCGH was to measure the distance between needle tips, one either side of the urethra, to each of four implanted fiducial markers. A total of 14 bilateral hip patients were treated with plastic needle implants, and 42 fractions were delivered. The maximum observed caudal shifts were 8 mm in the first fraction, 11 mm in the second fraction and 10 mm in the third fraction, all in different patients. As table 5-3 shows, the mean caudal displacement before adjustment was 1.6 mm (SD 3.1 mm).

	Caudal displacement (mm)			
Timing	Fraction 1	Fraction 2	Fraction 3	All fractions
Before adjustment				
Mean	1.0	1.5	2.3	1.6
SD	2.5	3.8	3.1	3.1
After adjustment				
Mean	0.1	-0.4	0.1	0.0
SD	2.7	2.6	2.9	2.8

Table 5-3: Caudal needle shifts for plastic needles relative to marker seeds implanted into prostate, before and after adjustment in each treatment fraction.

Greatest displacement was measured before the third fraction (mean 2.3 mm; SD 3.1 mm). After adjustment, mean caudal displacement was less (mean 0.0 mm; SD 2.8 mm). In the 14 patients treated, without adjustment 38% of fractions had displacement greater than 3 mm, compared with 0% of fractions after manual adjustment.

On average, 0.5 adjustments (range 0–1 adjustments) per fraction were made before treatment. This figure includes 6 fractions where needle displacement was close to, but within, tolerance. From a patient perspective, pushing needles to correct displacements can be very uncomfortable. It appears that using plastic needles may reduce the need for needle adjustment. The standard deviation of plastic needle displacements was greater than for stainless steel needles, but analysis suggested this may not be significant due to the small number of patients examined. However, the average displacements in 62% of plastic needle displacements were within our 3 mm tolerance for correction, and were not adjusted, whereas for stainless steel needles only 18% of fractions were within the 3 mm tolerance and would have remained unadjusted. This may explain the larger standard deviations in plastic needle displacements when compared with stainless steel needles.

The obturators supplied with plastic needles were about 1 mm in diameter, and were stiff enough that needles would remain relatively straight during implantation. However, plastic needles were still more flexible than stainless steel needles. When the steel obturator was removed, plastic needles would bend as shown in figure 5-5 below.

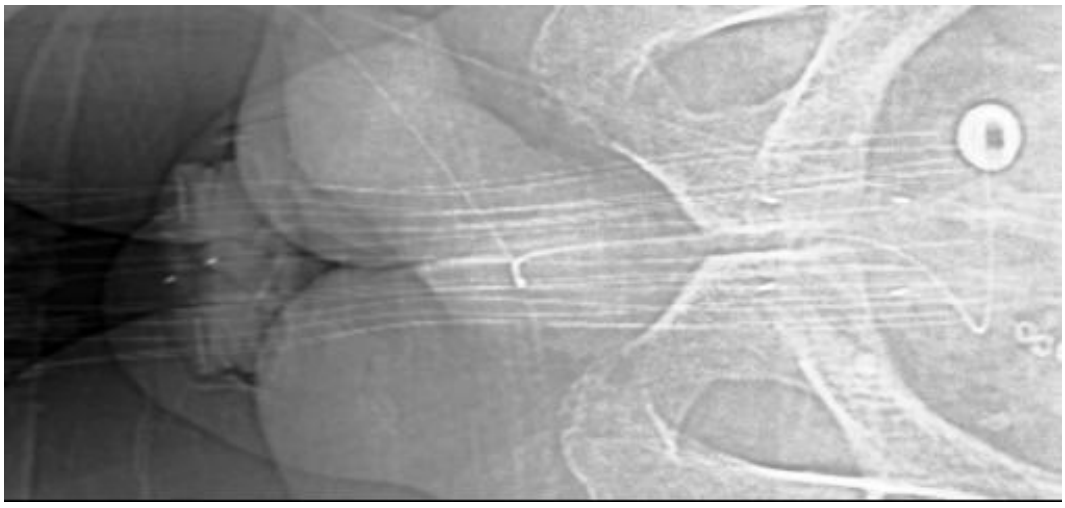

Figure 5-5: Coronal CT reconstruction showing deformation of implanted plastic needles after metal obturators were replaced with custom-made flexible wires. See text for details.

For treatment planning image acquisition with plastic needles the steel obturators were replaced with wires, described in Chapter 4, that matched the source wire flexibility. In this way, needle locations recorded in treatment planning images more accurately reflected locations at each treatment fraction, and planned dose more accurately reflected delivered dose. We can only speculate that increased flexibility reduced displacements when compared with stainless steel needles, as in all other respects the procedures were identical.

Contributors to needle displacement.

A range of parameters were tested to assess their impact upon needle displacement (Langham *et al.*, 2006). Patient age, time on hormone reduction treatment, time between EBRT and HDR treatments, ward location during hospitalisation were analysed, as were bowel preparation, time between theatre procedure and CT treatment planning image acquisition, time to first treatment fraction and between treatment fractions, the amount of time required for treatment setup, type of patient pain control (spinal epidural or patient controlled analgesia), the time taken to implant needles, and the number of needles. Each parameter was recorded and tested for significance in 69 patients treated with a total of 207 fractions. In this study, displacements were corrected in 120 fractions (58%), and in 21 (10%) fractions displacements between 3 and 4 mm were not corrected. The average displacement before adjustment in each fraction is shown in table 5-4.

	Caudal displacement (mm)			
Timing	Fraction 1	Fraction 2	Fraction 3	All fractions
Before adjustment				
Mean	3.7	4.9	5.4	4.7
SD	2.1	3.2	3.5	3.1

Table 5-4: Caudal needle shifts relative to marker seeds implanted into prostate, before adjustment each treatment fraction in patients treated at SCGH in 2005.

In this study, needle displacement was estimated by subtracting I_2, the needle tip to seed distance at treatment, from the baseline distance I_1. This tended to underestimate displacement, as shown by comparing *Before Adjustment* means in table 5-4 and table 5-3.

From these data, no significant contributor to needle displacement was found, except for a correlation between urological surgeon and displacement magnitude. Each surgeon used

the same patient care practices and implantation technique. However, the surgeon for whom patient needle displacements were greater typically implanted needles more quickly (28 ± 9 minutes versus 39 ± 13 minutes), and needles were more likely to be withdrawn and reinserted rather than 'steered' into position. We can only speculate that needle tracks in prostate tissue may increase the tendency for needles to move caudally, perhaps due to increased tissue injury and increased oedema. Unfortunately, data on tissue oedema and number of needle re-insertions were not recorded.

Recent studies (Yoshida *et al.*, 2010) found a significant link between needle displacement and overall treatment time, patient height, and use of anticoagulants. However, Yoshida *et al* employed an ambulatory technique in which patients were free to move around between treatment fractions. We do not expect patient height will influence our immobile patients. One may speculate that patient height may reflect general anatomical dimensions, and a taller patient may have a broader perineum so that less pressure is exerted on needles as the patient moves. In agreement with Yoshida *et al*, our data show an increasing average needle displacement at the first, second and third fractions, suggesting that the longer needles were implanted, the greater their displacement, despite readjustment towards baseline locations after each fraction. As well, Hoskin *et al* (2003) identified template movement, internal prostate motion, and tissue oedema as contributors to needle displacement relative to the prostate. All of these factors may affect needle displacements observed at SCGH. Irrespective of the cause of needle movement, it should be corrected before treatment to ensure the delivered dose matches the planned treatment dose.

5.2 Tumour Control Probability (TCP) modelling.

In the second part of the SCGH study (Tiong *et al.*, 2009), simulated plans were performed on 20 consecutive patients treated in 2007 and dose data were used to calculate tumour control probabilities (TCPs). The characteristics of the 91 patients and the last 20 replanned patients were similar. Calculated TCP values are between 0.0, indicating zero tumour cell kill, and 1.0, indicating complete tumour cell kill and hence tumour control. Dose to the original CTV for caudal needle displacements of 3, 6, 9, and 12 mm along the longitudinal axis was calculated using the computerised TPS. It was assumed that all needles in an implant were displaced by the same amount, since negligible relative movement of needles in the template was observed.

Dose–volume histograms for the CTV were exported in each case and data were used to calculate changes in TCP relative to the original plan. The method for calculating the TCP is outlined elsewhere (Wang and Li, 2003). In addition, the ability to sample the α radiosensitivity parameter, normally distributed across a patient population, was added (Nahum *et al.*, 2003). Physical parameters used for calculations included the following: three fractions, 0.33 days between fractions, EBRT dose of 46 Gy in 23 fractions, 35 days between EBRT and HDR, and 7.5 minutes for duration of HDR brachytherapy. Biological parameters from three different publications, summarized in table 5-5, were selected. We used the assumptions and parameter values of Wang *et al* (2003) because these were calculated from patients who had disease and treatment similar to our population. As there is a lack of consensus on the biological parameters for prostate cancers, we also calculated the TCP using other derived parameters, including the low α:β data reported by Brenner *et al* (2002), which necessarily incorporated low cell numbers (any α:β ratio must be used with an appropriate clonogenic cell density function - see (Haworth *et al.*, 2004b, a).

Parameter	Wang *et al* (2003)	Brenner *et al* (2002)	Nahum *et al* (2003)*
Cell potential doubling time (days)	42	42	42
Cell repair time (mins)	16	16	16
Mean α (Gy^{-1})	0.150	0.026	0.260
SD α	0	0	0.06
$\alpha:\beta$ (Gy)	3.1	1.2	8.3
Cell density (cm^{-3}) †	5×10^5	10	5×10^5

Table 5-5: Biological parameters used to calculate TCP in HDR prostate brachytherapy patients. A TCP calculation included 105 α values sampled from a normal distribution with stated mean and SD, and a lower cut-off of 0.01 Gy^{-1}. * include hypoxia effects. † Clonogen numbers were calculated by multiplying cell density by measured prostate volume.

We also used parameters from Nahum *et al* (2003), with hypoxia contributions, because our population of patients mostly had high risk disease (>T2b, PSA > 20 ng/ml, Gleason > 8). Parameters calculated by Nahum *et al* were based on cell cultures, and explained the observed response rates of prostate cancers by the contribution of tumour hypoxia.

Table 5-6 shows for 0 mm displacement the median dose was 16.7 Gy. A baseline TCP value for zero displacement was calculated and normalised to 1.000 in all models. Needle movement relative to the prostate gland was assumed to be along the longitudinal needle

axis, and lateral movement due to prostate gland oedema was assumed to be negligible. In the 20 replanned patients, for each 3 mm of caudal needle displacement the minimum dose to the CTV decreased, mainly at the prostate base. The effect of caudal displacement on median dose and on calculated TCP values is shown in table 5-6.

Displacement (mm)	0	3	6	9	12
Median dose (Gy)	16.7	16.1	13.3	10.6	8.4
TCP median (Wang model)	1.000	0.998	0.964	0.797	0.265
% patients with more than 5% reduction		0	25	90	100
TCP median (Brenner model)	1.000	0.973	0.853	0.548	0.206
% patients with more than 5% reduction		20	95	100	100
TCP median (Nahum model)	1.000	1.000	0.964	0.902	0.806
% patients with more than 5% reduction		0	50	80	100

Table 5-6: Target volume TCP changes in three models for increasing caudal needle displacement. The percentage of patients with more than 5% reduction in calculated TCP values is indicated for each model at each displacement.

As noted earlier, the model of Wang *et al* used parameters derived from patients who had disease and treatment similar to our population. On the basis of those assumptions the reduced dose translated into a significant drop in median relative TCP ($p < 0.01$ when all medians were compared), as shown in table 5-6. The pattern of decline in TCP as needles moved caudally was consistent in each model. The percentage of patients with a relative TCP decrease of more than 5% was also determined for each model, and all three models produced similar results. Each showed a consistent TCP reduction as needle displacement increased. In the model of Brenner *et al*, which used a lower α:β than that of Wang *et al*, TCP declined even more rapidly, whereas in the model of Nahum *et al* the decline was less rapid. In each model, a 3 mm displacement resulted in most patients having TCP close to or greater than 95% of the original. At 6 mm displacement, many (25% to 95%) patients were predicted to have a TCP decline greater than 5% of the original value.

A relatively stringent criterion was set for an unacceptable TCP decrease due to needle movement. Wang *et al* (2003) found the 4-year biochemical relapse free survival rate in patients with cancer grade and treatment schedule similar to ours was 75%. A 5% decrease in TCP translates into a relapse-free survival rate of 71.2%. This decrease may not be large

in absolute terms, but we believe that correctable treatment errors should not be allowed to impact on patient outcomes.

Others (Hoskin *et al.*, 2003; Pellizzon *et al.*, 2003) made adjustments when needle displacement was greater than 5 mm. It was unclear from the report of Hoskin *et al* whether a margin around the CTV was added to give a treatment volume, whereas Pellizon *et al* specified the minimum dose was 4 to 6 mm outside peripheral needles. The margin for acceptable needle displacement will depend upon prostate shape, needle arrangement, and planned dose distribution; our data suggest the margin should be smaller than 5 mm, and that it is feasible to maintain displacements less than 3 mm.

Chapter 6 . Summary of Findings.

As discussed in Chapter 2, the therapeutic advantage of prostate HDR brachytherapy treatment as a boost to EBRT is clear. Prostate HDR brachytherapy offers accelerated treatment schedules and highly conformal dose distributions that spare large volumes of healthy tissue from radiation, while EBRT provides highly uniform dose throughout the target volume. Avoidance of critical structures using IMRT, and dose reduction to healthy tissue using HDR brachytherapy, offers a beneficial combination for the recipient patient. Given the advantages of prostate HDR brachytherapy, this work set out to determine an optimal and clinically practical protocol for reliable acquisition of clinically useful image data for HDR prostate brachytherapy treatment planning in patients with bilateral hip prostheses. Specific questions addressed in this work were:

- Is there an optimal imaging technique for patients with bilateral hip prostheses?
- Are inter-fraction needle movements different?
- What needle types are better?

This work assessed ultrasound (U/S), magnetic resonance (MR or MRI) and computed tomography (CT) imaging modalities. Findings are summarised below.

6.1 Optimal imaging technique.

The physical properties of hip prostheses – high physical and electron density, and magnetic susceptibility characteristics – made this aim a challenging prospect with CT, MR, and ultrasound. Each investigated modality offered unique advantages and disadvantages for prostate imaging between hip prostheses, however, in many cases the acquired images either could not reliably provide clinically uselful prostate detail, or could not provide spatially accurate detail on the implanted HDR brachytherapy needles, or both. In Chapter 3, criteria were established for ‘clinically useful’ images to provide:

- Accurate visualisation of implanted HDR brachytherapy needles, with no loss of detail particularly at the needle tips.
- In the case of fractionated HDR treatment, clear visualisation of implanted fiducial markers for prostate and needle localisation at each fraction.

- Distortionless images for accurate volume definition and accurate needle separation, ensuring accurate dose calculation.
- Clear detail of prostate anatomy – at least, sufficient detail to enable accurate definition of the target volume for radiotherapy treatment planning.

Given these criteria, findings for each of the modalities investigated in greater detail in Chapter 4 were:

6.1.1 Ultrasound.

Perhaps the modality least affected by the presence of bilateral hip prostheses, due in part to the conventional use of trans-rectal transducers for prostate imaging. Prostate images are acquired without the need for signal to traverse the prostheses, and the limited penetration depth of around 6 cm for a 6.5 MHz signal means that acoustic reflections from prostheses are unlikely to be problematic. However, in conventional B-mode grey-scale ultrasound images used routinely for image guidance in brachytherapy procedures, artifact such as shadowing, reverberation, and to a lesser extent velocity displacement are confounding factors for accurate HDR brachytherapy treatment planning and delivery.

For HDR prostate brachytherapy, TRUS enables real-time guidance for needle placement, and some centres such as RAH in South Australia use TRUS data for 'real time' treatment planning. One incentive for this approach was the potential to reduce the amount of time a patient had needles implanted. However, from a pragmatic clinical viewpoint, in a centre where theatre access is in high demand the comparatively long times required for needle insertion followed by 'real time' treatment planning and delivery may be a disincentive for real-time TRUS treatment planning. As well, uncertainty in needle tip definition could be alleviated using an external reference point from which the length of each needle was physically measured and checked against treatment planning images to ensure accurate distal tip identification. RAH found that tips could be identified with ±1 mm accuracy in phantom studies, however, ±3 mm tolerance was applied in patient treatment due to increased artifact and reduced image quality.

For HDR as in LDR brachytherapy at SCGH and many other centres, a TRUS volume study was routinely acquired immediately prior to HDR needle implantation. The volume study assisted to visualise the prostate base and apex, and the lateral and anterior-posterior

extent of the target. It also guided marker seed implantation at the prostate base and apex, and assisted visualisation of the target volume for guidance if subsequent treatment planning images provided inadequate visualisation of the target volume.

6.1.2 Magnetic Resonance Imaging.

While offering possibly unparalleled detail with appropriate settings of the many parameters that can affect MR image contrast and spatial resolution, the potential sources of artifact in MR imaging are numerous, and the acquisition of clinically useful images for HDR prostate brachytherapy treatment planning in the presence of bilateral hip prostheses was particularly challenging. Patient motion, Gibbs ringing, flow artifact, RF heating, gradient-related distortion, and magnetic susceptibility artifact all acted to confound the acquisition of clinically useful treatment planning images for HDR prostate brachytherapy.

As discussed in Chapter 4, MR-compatible plastic needles were in regular use at SCGH in each HDR implant. However, the steel obturators used to stiffen the plastic needles to assist implantation were not MR compatible, and modified obturators made from discarded 'dummy' wires from the HDR afterloader were developed. The nitinol metal wires were non-ferrous, and replicated the active source wire flexibility, so that the needle flex recorded in treatment planning images more closely matched the treatment geometry. MR scans were extended to include the needle template sewn to the patients' perineum which served as a reference point from which each distal needle tip could be physically measured and compared with the length measured on images. Differences were corrected by redefining needle tips in the TPS, however, in some cases the apparent and physically measured lengths differed by more than 10 mm.

Metal artifact in MR images was a limiting factor for image utility in HDR prostate brachytherapy treatment planning. Spatial distortion due to local magnetic field disruption, local signal void within prostheses, and localised areas of high signal intensity near the prostheses all complicated interpretation of images acquired for treatment planning. The SCGH BLIP phantom was MR scanned with a range of scan parameters to gain an appreciation of the influence of hip prostheses upon image quality. A suitable image was defined as having adequate detail to visualise implanted needles and fiducial markers, and containing minimal distortion in the target volume. Studies concluded a T1 TSE sequence may provide the greatest theoretical possibility of reducing susceptibility artifacts.

Clinically, reliable acquisition of acceptable images for treatment planning proved elusive. Despite a promising start with our first patient, and attempts on subsequent patients with previously successful sequences and then often two or three potentially useful sequences along with much advice and assistance from local MR technology specialists, we could not consistently acquire acceptable data for HDR prostate brachytherapy treatment planning. No patient in this study was remarkable in terms of weight or size, and we can only speculate that image blur due to patient motion was fortuitously absent in the first patient. Patient movement perhaps was a significant contributor to the poor image quality observed in other patients. Unfortunately, each acquired scan took 12-15 minutes to complete, and patients invariably found the experience long, uncomfortable, and disorienting – image blur was an inevitable artifact in almost all cases. Given that the acquisition of clinically useful MR images for treatment planning was not guaranteed, a multi-slice CT scanner was used to acquire 'backup' images that usually were of acceptable quality and indeed were used for treatment planning in many of the first 10 patients. A clinical decision was therefore made to discontinue MR scans of bilateral-hip prosthesis patients.

6.1.3 Computed Tomography.

Filtered back-projection (FBP) of x-ray projection data remains the backbone of CT image reconstruction techniques, and the reconstruction process (discussed in Appendix 2.3) assumes that differences in recorded signal intensity are due only to attenuation of the projected x-ray beam in the object. CT artifacts may be observed in images of any patient, but for patients with bilateral hip prostheses metal artifact (streaking and beam hardening) due to projections traversing the high-density prostheses, and partial volume averaging are unavoidable, and may compromise accurate target and distal needle tip identification

To examine the effectiveness of commercially available metal artifact reduction algorithms, CT scanners supplied by three manufacturers were tested with the SCGH BLIP phantom. The HDR brachytherapy practitioner requires as much detail as possible on the high-density implanted markers and needles and the soft tissue brachytherapy target. Our tests made the imaging conundrum quite apparent: the question of how to reduce high-density material artifacts and simultaneously retain adequate soft tissue detail does not yet appear to be successfully addressed in the tested CT systems. Given that artifact reduction techniques may themselves introduce additional artifact into the image it may be advisable, for now, to avoid metal artifact filtration altogether.

Computed tomography, like other digital imaging techniques, offers a significant advantage over film: image brightness and contrast can be altered without re-imaging the patient. Suitable selection of the CT number greyscale level and window (range) can optimise contrast for an object of interest when the level is set to the object's average CT number. In HDR brachytherapy images, implanted needles, marker seeds, and the target volume of soft tissue can be separated by the CT number ranges that characterise each material's electron density. In view of the uncertain availability of plastic implant needles for the SCGH afterloader (SCGH have since obtained TGA approval to import applicator kits from the original equipment manufacturer after their supplier withdrew supply), investigations focussed upon steel implant needles. With the nominal 135kVp energy routinely used for prostate HDR brachytherapy imaging on a Toshiba Aquilion LB scanner, on an extended CT number scale the optimum windows and levels for stainless steel needle detection were 3700 ± 1700 HU, and for prostate tissue were 40 ± 40 HU. For gold seed markers, the optimum HU level and window was found to be 13000 ± 5000 HU.

CT imaging was generally free from distortion and was spatially accurate, within the limitations imposed by pixel size in the field of view and voxel volume determined by slice thickness. The impact of volume averaging on the accuracy of needle tip determination was studied with models of steel implant needles. The predicted CT number in a voxel containing a stainless steel needle with a stainless steel obturator was 3799 ± 478 HU which compared well with the clinically observed value of 3705 ± 420 HU. For all tested slice thicknesses it was observed that with minimum CT number set to 2000 HU, the apparent distal tip matched the actual internal distal tip to within ± 0.7 mm, ensuring dosimetric accuracy of better than 0.7%.

6.1.4 Conclusion.

The recommended imaging modality to obtain clinically useful images for prostate HDR brachytherapy treatment planning in patients with bilateral hip prostheses is CT, with concurrent acquisition of an ultrasound volume study to aid soft tissue delineation in the TPS. If using flexible plastic needles, marker wires with similar flex properties as the Ir-192 source wire should be used. For 135kVp scan energy, the recommended CT number window and level settings to ensure needle tip definition to within ±0.7 mm (ensuring dosimetric accuracy of better than 0.7%), was 3700 ± 1700 HU. Users should confirm these values on their own CT scanner before adoption into clinical practice.

6.2 Inter-fraction needle movement.

A concurrent aim in this work was to ensure that bilateral hip prosthesis patients receiving prostate HDR brachytherapy achieved similar dosimetry outcomes as non-prosthesis patients. This work investigated differences in movement between stainless steel and plastic needles, and used calculated TCP with needle movement in the target volume to indicate the radiobiological efficacy of radiation dose delivery to the target volume.

As discussed in Chapter 5, at each treatment fraction in HDR prostate brachytherapy, needle displacement was visualised via fluoroscopy, compared with baseline data, and corrected by advancing implanted needles and template as a unit, with adjustments stabilised by a fixation device. Caudal needle shifts were determined by analysing the needle tip – fiducial marker distance in baseline versus treatment images. For an average patient, a simple (I_2-I_1) approximation had sufficient accuracy, but was in error by up to 1.6 mm for some markers. Experience is required and judgement must be exercised when declaring a required shift. Using the average angle θ subtended by needle tips to each fiducial marker, a correction factor $1/\sin(\theta)$ was applied to the measured difference (I_2-I_1) to improve the average agreement to within 0.2 mm for all markers in all treatment fractions. SCGH has recently implemented the more accurate $S = (I_2\text{-}I_1)/\sin(\theta)$ expression to assess needle shifts in the treatment room.

When stainless steel needles were implanted, the mean caudal displacement before adjustment in all fractions was 5.4 mm (SD 3.3 mm). Greatest displacement was measured before the third fraction (mean 6.4 mm; SD 4.2 mm), suggesting needles become less stable as treatment progresses. After adjustment, the mean caudal displacement was reduced (mean 1.2 mm; SD 1.7 mm). Plastic needle displacement in patients with bilateral hip prostheses was also examined, and the mean caudal displacement before adjustment in all fractions was 1.6 mm (SD 3.1 mm). The greatest displacement was again measured before the third fraction (mean 2.3 mm; SD 3.1 mm). After adjustment, mean caudal displacement was less (mean 0.0 mm; SD 2.8 mm). On average, with plastic needles only 0.5 adjustments (range 0–1) per fraction were required, compared with an average 1.2 adjustments (range 0–3) per fraction to reduce steel needle displacements before treatment. Errors due to cranio-caudal stretching of the prostate were lessened by measuring the distances between markers to quantify stretch, and exercising judgment when interpreting measured displacements against fiducial markers at the base.

From a patient perspective, pushing needles to correct displacements can be very uncomfortable, and it appears that plastic needles reduce the need for adjustments when compared with stainless steel needles. Matching the geometry of plastic needles in CT treatment planning images was made possible with the development in this work of nitinol marker wires. The wires, manufactured from discarded afterloader dummy wires, precisely match the source wire flexibility, and therefore provide an excellent match to replicate the actual treatment geometry.

The second part of the SCGH study investigated the effect of needle movement on delivered dose and tumour control probabilities (Tiong *et al.*, 2009). Simulated plans were performed and dose data were used to calculate TCPs. Dose to the original CTV for uniform caudal needle displacements of 3, 6, 9, and 12 mm along the longitudinal axis was calculated using the computerised TPS. Dose–volume histograms for the CTV were exported in each case and data were used to calculate changes in TCP relative to the original plan. The TCP model of Wang *et al* (2003) showed that the reduced dose due to needle movement translated into a significant drop in median relative TCP. The pattern of decline in TCP as needles moved caudally was consistent in each model. In the model of Brenner *et al*, which used a lower α:β than that of Wang *et al*, TCP declined even more rapidly, whereas in the model of Nahum *et al* the decline was less rapid with needle displacement. The percentage of patients with a relative TCP decrease of more than 5% was determined for each model, and demonstrated a consistent increase as needle displacement increased. Overall, the three models produced broadly similar results. A 3 mm displacement resulted in most patients having TCP close to or greater than 95% of the original, but at 6 mm displacement, many (25% to 95%) patients were predicted to have a TCP decline greater than 5% of the original value. The margin for acceptable needle displacement will depend upon prostate shape, needle arrangement, and planned dose distribution; our data suggest the margin should be smaller than 5mm, and that it is feasible to maintain displacements less than 3 mm.

6.3 Preferred needle type.

Stainless steel and plastic implant needles with stainless steel and nitinol obturators were assessed to determine which offered an optimum imaging solution. Plastic needles with nitinol marker wires were found to reduce artifact in CT-acquired treatment planning images. It appears that plastic needles reduce the need for adjustments, however, their

flexibility can make accurate steering during implantation difficult, and without marker wires identification can be challenging on fluoroscopic images used for needle displacement checks at treatment. The use of nitinol marker wires can assist plastic needle identification in the pre-treatment needle displacement checks, and may assist to better replicate the treatment geometry in planning images. However, in view of the increased flexibility of plastic needles and the presence of significant artifact already in treatment planning CT images due to the bilateral hip prostheses, stainless steel needles may be preferred due to their increased stiffness and ease of identification in CT images.

Conversely, in newer treatment planning systems that take tissue heterogeneity into account, the artifact from hip prostheses and from implanted needles will introduce inaccuracies into dose calculations. For non-prosthesis patients, the use of plastic needles without metal obturators may assist to minimise image artifact and therefore improve dose calculation accuracy. For bilateral hip prosthesis patients, it may be prudent to revert to dose calculation engines that treat the patient as being composed of water-equivalent material, and therefore ignore the impact of streaking and other image artifacts.

6.4 Directions for future work.

Further investigation is warranted into the optimum imaging modality that will provide clear, accurate, distortionless visualisation of implanted HDR brachytherapy needles, with no loss of detail particularly at the needle tips, clear visualisation of implanted fiducial markers for prostate and needle localisation at each fraction, and clear detail of prostate anatomy. Potential studies are discussed below.

Ultrasound. The prospect of improved image quality using tissue harmonic imaging rather than B-mode imaging for prostate brachytherapy offers a way forward with the possibility of heightened edge definition and improved needle identification (Sandhu *et al.*, 2010). Successful treatment planning from ultrasound images will depend to an extent upon the axial spatial resolution of ultrasound transducers, and particularly upon the reproducibility of the target volume shape at each treatment fraction. The latter will likely require use of at least a surrogate transducer inserted into the patient's rectum at each treatment fraction to better match the treatment planning configuration. Our experience suggests that conscious patients find an *in-situ* transducer highly uncomfortable, and are unlikely to remain sufficiently immobile for the duration of a treatment fraction. If this limitation can be

overcome, a needle and target location verification technique will need to be developed that is clinically acceptable in terms of efficiency of use and dosimetric accuracy.

CT. As brachytherapy treatment planning systems begin to take account of tissue density variation via CT Hounsfield number, the ability to acquire artifact-free CT images for any patient, not just those with bilateral hip prostheses, will become increasingly important. Image processing to modify CT numbers before importation into treatment planning systems has merit, and indeed is the subject on ongoing research. However as discussed in Chapter 3, many techniques for artifact reduction essentially predict the appropriate CT number for a voxel based upon its nearest neighbours, which for small objects such as implanted marker seeds may obliterate them altogether. Such nearest neighbour interpolation techniques may not solve the problem of missing data that may cause inaccurate depiction of needle tips in CT images. As discussed in Chapter 3, iterative reconstruction techniques such as those reported by Boas and Fleischmann (2011) may go some way towards alleviating this limitation.

MR. While plastic needles potentially are acceptable for MR scans, finding an obturator material that will highlight the needles in MR images is challenging, due in part to the small volume of material that can be contained within the implanted needle. The need to ensure no fluid leaks into an implanted needle so that source wire paths are not obstructed means that suitable obturator 'straws' can contain only a small volume of contrast material. Possible materials do exist (Frank *et al.*, 2008; Varma *et al.*), but their utility for HDR needle identification is not well documented and should be investigated.

Given the attraction of MR imaging for prostate HDR brachytherapy due to its improved soft tissue detail compared with CT or ultrasound, an obvious future path is to acquire an endorectal MR coil and investigate the clinical practicality of its use in conscious patients recently recovered from general anaesthesia with an HDR needle implant in situ. Given the experience gained from this work, the prospect for good patient compliance is not encouraging, but the use of appropriate patient sedation to reduce discomfort for the duration of an MR scan should be considered. When used in combination with suitable needle marker straws, this may present a viable and clinically reliable imaging technique.

CT/MR fusion. As noted by Rivard *et al* (2009) implementation of image fusion where CT needle images and MR soft tissue images are co-registered (preferably via deformable

transformation of the MR image) for treatment planning should be investigated. Image fusion may impact upon treatment dosimetry and treatment planning techniques. It is known, for example, that the prostate volume defined on MR images can be up to 35% smaller than that defined on CT images (Hentschel *et al.*, 2011), however as Hentschel *et al* used 3mm MR slices and 5mm CT slices, it would be worthwhile to undertake a similar study with equal CT and MR slice thickness to reduce the possible impact of partial volume averaging. As demonstrated in this work, implanted needles can be difficult to detect on MR images, and as discussed earlier, an investigation of appropriate markers that will be visible in both CT and MR for co-registration would be required. As well, the clinical practicality of acquiring both CT and MR images for every patient should be considered.

Appendix 1

A1.1 Hip prostheses types and compositions.

An interesting account of the history of total hip arthroplasty from the 1700s to 1950's was provided by Gomez and Morcuende (2005a). The first reasonably successful repairs were made by inserting a piece of perishable material such as *fascia lata* (the soft tissue component of connective tissue) between damaged surfaces on the femoral head and acetabulum. Adipose tissue, pig bladder, and gold foil were amongst the materials tested with limited success. In 1923 Smith-Petersen (1948) used a glass mould that fitted into the acetabulum and contained the bony femoral head. Macalister Bicknell, who formed the first X-ray tube for Dr Walter Dodd, made the first glass moulds.

Metal-on-metal prostheses were introduced in the 1930s (Wiles, 1958), and around 1958 Charnley successfully implanted a stainless steel femoral post articulating against a polymeric (teflon) acetabular cup lining a space reamed out of the acetabulum (Charnley, 1960). Such was the impact of Charnley's ongoing work that he is considered the pioneer of modern-day total hip arthroplasty (Gomez and Morcuende, 2005b). In 1972 the first all-ceramic (alumina Al_2O_3) total hip replacement was reported (Boutin, 1972) and in recent times ceramics such as zirconia (ZrO_2) were used. A modern hip prosthesis typically consists of a cobalt-chrome alloy femoral stem, with a similar or ceramic femoral head articulating against a ceramic or ultra-high molecular weight polyethylene (UHMWPE) cup within a titanium acetabular shell. To reduce friction, specialised coatings may be applied to head and liners, and hydroxyapatite, a bone analogue, may be applied to stems to promote osseo-integration (Navarro *et al.*, 2008). Carbon fibre composite materials are also being evaluated (Dimitrievska *et al.*, 2009),

Friction between contact surfaces is the main source of particulate wear in hip prostheses, and the biological effect of wear debris depends upon quantity, particle size and shape, and composition (Sargeant and Goswami, 2006). It is thought that metal particles may increase the risk of cancer, and studies have shown this may be true for lymphomas and leukaemias, but that there may be reduced risk of breast, colon and rectal cancer (Gillespie *et al.*, 1988). On the other hand, a high concentration of metal ions around a prosthesis may afford some protection from infection (Hosman *et al.*, 2009), via preferential uptake of Co and Cr ions, inhibiting iron-dependent metabolic activity and hence reducing bacterial and biofilm

growth. Clearance between the femoral head and acetabular cup is typically about 40 μm, and for ceramic joints can be just 10 μm. The joint is lubricated by proteins in synovial fluid that adsorb onto the prosthesis surface. Synovial fluid exhibits non-Newtonian flow properties which include elastic, shear thinning and normal stress effects (Meziane *et al.*, 2008), and bench-tests of joint durability are confounded by the lack of a synthetic analogue. To improve friction and wear properties,smoother surfaces can be made with wrought or forged prostheses that contain less carbon (0.05%) than cast parts (0.2%).

The aim of prosthesis design is to match the properties of bone (Scannell and Prendergast, 2009) during everyday activities such as sitting, walking, jogging, stair climbing and load carrying. An overly stiff prosthesis can cause bone hypertrophy where stresses are concentrated, and resorption of bone in areas shielded from stress. Bone resorption can lead to joint loosening and the need for hip revision surgery, whereas a prosthesis that is too elastic may move against the bone, causing erosion and joint loosening. Components may be glued with polymethylmethacrylate (PMMA) cement, relying upon interlock between rough surfaces rather than adhesion, or fixed without cement, relying upon screws, press-fitting, or porous ingrowth into a rough surface (Morshed *et al.*, 2007).

In older patients more likely to be seen for HDR brachytherapy, a UHMWPE $(\text{-}CH_4\text{-})_n$, n = 70 000 – 200 000, acetabular shell usually is the softer wearing surface, with density about 0.93 gcm^{-3}. Techniques to increase the durability of UHMWPE include cross-linking by 100 kGy irradiation (Jasty *et al.*, 2005) with 10 MeV electrons or Co gamma radiation, followed by high temperature annealing to eliminate free radicals. Acetabular cups are typically titanium alloy hemispheres, 40 - 60 mm diameter, containing a UHWMPE or ceramic insert with 8 - 10 mm thick walls (Salvi *et al.*, 2005). At an estimated 0.1 mm annual wear rate, most cups should outlive their recipient (Cameron, 2002).

Many older prostheses have 28 - 32 mm diameter femoral heads, thought to be a compromise between joint utility and the amount of wear debris and subsequent risk of osteolysis. In recent times surgeons have used larger-diameter heads that better match the natural anatomical dimension of the joint, and metal-on-metal prostheses for improved wear particularly in younger, active, or heavier patients (Cuckler *et al.*, 2004). For medical imaging, the physical size and renewed use of metals is a disadvantage, but the prostheses afford recipients better stability and a greater range of motion, are more forgiving of surgical placement errors, and reduced likelihood of dislocation (Burroughs *et al.*, 2005).

Appendix 2

A2.1 Ultrasound.

Ultrasound uses the travel-time of reflected acoustic waves to visualise tissue, and the physics of ultrasound can essentially be summarised with three equations

$$v = f\lambda \qquad \text{(A2.1)}$$

$$v = Z/\rho \qquad \text{(A2.2)}$$

$$R = 1 - 4Z_2Z_1/(Z_1 + Z_2)^2 \qquad \text{(A2.3)}$$

Equation 2.1 describes the relation between acoustic wave velocity v, frequency f and wavelength λ. In soft tissue $v \approx 1540$ ms^{-1}, in fat $v \approx 1450$ ms^{-1}, and in femoral bone $v \approx 3800$ ms^{-1}. In a stainless steel hip prosthesis, $v \approx 5800$ ms^{-1} (Bensamoun *et al.*, 2004). Useful ultrasound signal frequencies are in the range 2 - 18 MHz, and around 6.5 MHz is typical for prostate imaging. Higher frequencies decrease the signal penetration depth but improve spatial resolution. Acoustic signals at 6.5 MHz typically have an image range of 6 - 7 cm.

Equation 2.2 describes how velocity v, and hence wavelength λ of an acoustic wave vary as a function of a medium's acoustic impedance, Z, and its density ρ. As waves propagate they deposit energy into the medium and are attenuated, mainly by scatter and absorption, by about 0.8 dBcm^{-1}MHz^{-1}. At boundaries between media with impedance Z_1 and Z_2, the fraction of signal reflected back towards the transducer crystal, R, is given by eqn 2.3.

Reflected signals (echoes) of sufficient intensity are used to generate ultrasound images. In a grey-scale B mode image commonly used for prostate imaging, brightness corresponds to echo amplitude. White is highly reflective, black is poorly reflective. A speckled image is observed from organs like the kidney or spleen that contain many scattering sites with dimensions similar to the transmitted wavelength (0.1 - 0.3 mm). A uniformly-filled object such as the bladder appears dark. Small objects of high density such as implanted HDR brachytherapy needles appear white.

The full dynamic range of received and amplified ultrasound signals may span 120 - 140 dB (i.e. up to 7 orders of magnitude), a far greater range than the 4 or 5 orders of magnitude variation the human eye is capable of simultaneously discerning (Li *et al.*, 2007). Further, a grey-scale B-mode image typically compresses the signal range into 256 shades of grey from white to black, further compounding the loss of contrast resolution inherently available in ultrasound data. Ultrasound display equipment relies upon a number of assumptions about media to determine the source and intensity of received echoes. It is assumed that echoes travel in a straight line and originate from a single reflection within the main acoustic beam, and that the depth of reflecting objects is directly related to the time taken for acoustic pulses to return to the transducer as an echo. In any imaged media, the speed of sound is assumed to be constant, and signal attenuation is assumed uniform.

Spatial resolution: The AAPM task group 128 report (Pfeiffer *et al.*, 2008) specifically addresses aspects of quality assurance for prostate brachytherapy ultrasound systems, including spatial resolution. An earlier report on B-mode ultrasound quality control by the AAPM Ultrasound Task Group (Goodsitt *et al.*, 1998) suggests a broader quality control programme for general ultrasound systems. For HDR brachytherapy, good spatial resolution is important for accurate needle localisation (and hence radioactive source placement), and accurate delineation of target volumes and organs at risk. A schematic of the 2-D B-mode imaging planes from a TRUS transducer is shown in figure A-1. Spatial resolution is axis-dependent (axes as shown in figure). Both AAPM reports recommend spatial resolution measurements be repeated at several depths in each direction to establish constancy (or otherwise) of measured parameters.

Figure A 2-1: Ultrasound transducer imaging planes and spatial resolution directions. Adapted from Hangiandreou *et al* (2003).

Axial resolution in a B-mode image is independent of depth, and higher transmitted frequencies provide better axial resolution but are more attenuated, and this may limit the maximum useful signal range. For prostate imaging 6.5 - 7.5 MHz is common, corresponding to axial resolution of 0.24 – 0.21 mm. Lateral resolution is depth dependent, and modern systems provide multiple focal zones in the axial direction so that lateral resolution can be optimised over a broader range. However, more focal zones reduce frame rates (i.e. images are redrawn less frequently). SCGH sets six focal zones, reducing frame rates to 8 Hz – sufficient in most situations. In practice the observed lateral dimension of needle images is wide, and true needle locations are at the centre of the lateral image.

Elevational resolution or slice thickness depends upon the physical length of the piezo-electric crystal, typically about 5.5 mm. Transducers sometimes include special focussing layers over piezo-electric crystals, designed to optimise elevational resolution over a range of depths corresponding to the intended transducer application. Unfortunately for transverse imaging in HDR brachytherapy, the elevational direction corresponds to transverse slices through the implanted needles, so that distal needle tips are resolved with comparatively poor resolution. In comparison, the longitudinal array in a biplanar TRUS transducer offers improved resolution of distal needle tips, as needles lie along rather than across the array. This reasoning contributed to the original design of volume acquisition imaging systems for HDR treatment planning that acquired longitudinal images over a range of sector angles for reconstruction in a TPS. Unfortunately, most longitudinal arrays in older biplanar transducers were too short to simultaneously capture the entire prostate target volume with sufficient margins, and the distal tips of all implanted needles.

A2.2 Magnetic Resonance Imaging.

The history of MRI is peppered with Nobel prizes – to date, thirteen (Boesch, 2004) were awarded for work directly linked with MRI: Damadian (1971, 1980) first demonstrated that nuclear magnetic resonance (MR) techniques could distinguish cancerous from normal tissue, and in 1980 Damadian's company, FONAR, provided the first commercially available imaging device that utilised nuclear magnetic resonance properties of atoms and molecules. This followed landmark work by Lauterbur (1973), who reported a new imaging technique he called 'Zeugmatography' that exploited magnetic resonance properties. Using gradients in applied magnetic fields, Lauterbur generated a 2-dimensional image of an object using nuclear magnetic resonance data and iterative back-

projection analysis, similar to analysis techniques used in original CT work by Hounsfield (1973). In 1975 Ernst reported 2-dimensional phase and frequency encoding using switching magnetic field gradients, and 2D Fourier analysis to further simplify MR image formation (Kumar *et al.*, 1975). Mansfield (1977) further refined the use of gradient fields and mathematical analysis techniques for MR imaging, and presented images of a human finger (Mansfield and Maudsley, 1977). The next 20 years saw continuous improvement of image quality with the introduction of cryogenic superconducting magnets that improved magnetic field stability, use of contrast agents (mainly gadolinium-based), and faster data acquisition times that enabled MRI in dynamic studies such as cardiac imaging. Historical reviews of MR are provided by Geva (2006), Blamire (2008), or Macovski (2009).

Many medical MR scanners operate with 1.5 T static magnetic fields, but since 2002 a growing number of 3 T scanners are in use. High field (> 2T) and ultra-high field (> 4T) MRI offers potential benefits (Kuhl *et al.*, 2008a; Willinek and Schild, 2008); signal to noise ratio improves, image contrast can increase, and imaging times can be shorter. However, the high volume of variably-conductive tissues in the abdomen and pelvis means that radio-frequency (RF) and static magnetic field heterogeneities and RF eddy currents are more noticeable in these areas. The specific absorption rate (SAR) or rate of energy deposition into an imaged object increases as the square of applied RF frequencies, and unfortunately, chemical shift and magnetic susceptibility artifacts (caused by metal hip prostheses) are more pronounced. Scanners operating with 7 T static fields are an emerging human imaging technology (Krug *et al.*, 2009; Zwanenburg *et al.*, 2009) capable of increased spatial resolution (to 0.1 mm) and improved diagnostic utility.

Physics of MRI.

Protons and neutrons possess ‘spin’ (magnetic moment). Due to their non-zero nuclear spin, atoms with an odd mass number will have net magnetisation when exposed to an external magnetic field. The net magnetisation vector precesses about the applied magnetic field direction at a characteristic frequency, first reported in 1897 by Lamor (Tubridy and McKinstry, 2000). To be medically useful, the target atoms need to be present in ‘high enough’ concentrations of the appropriate isotope that possess a high magnetic moment. The main signal source in medical imaging arises from hydrogen (protons), mostly present as water or fat in the human body.

Bloch (1946; Bloch *et al.*, 1946) and Purcell (Purcell *et al.*, 1946) independently presented work on magnetic resonance and nuclear spin precession properties of nuclei in bulk materials, for which a joint Nobel Prize in Physics was awarded (Bloch, 1964; Purcell, 1964). They showed that for target nuclei in static magnetic fields, application of a suitable RF field produced a 'resonance' signal, with magnitude dependent upon the excess number of protons aligned parallel with the applied field. The magnetic field aligns more proton spins in parallel (lowest energy) magnetisation states, and a particular amount of energy E (from the applied RF field) is required to 'flip' proton spins to anti-parallel alignment. Flipping back to parallel spin alignment emits a photon with characteristic energy E (frequency ν). The resonance frequency ω_0 that enables spin flip and maximises emitted signal is given by Larmor's equation

$$\omega_0 = 2\pi\nu = \gamma B_0 \qquad \text{(A2.4)}$$

γ is the gyromagnetic ratio (magnetic moment : angular momentum ratio), unique for each element. For protons, the Larmor frequency is 42.58 MHz/T. In a conventional MR coordinate system, the external field B_0 and net magnetization vector M_z at equilibrium are aligned along the z axis (longitudinally). The magnetic field B_1 of an applied RF pulse exerts a torque on the vector M_z, rotating it into the xy (transverse) plane by angle

$$\theta = 2\pi\gamma B_1 t \qquad \text{(A2.5)}$$

where t is the amount of time an RF signal was applied. A 90° RF pulse maximises transverse magnetisation M_{xy}, and makes longitudinal magnetisation M_z zero. A 180° RF pulse sets $M_z = -M_z$, and $M_{xy} = 0$. After RF pulse excitation, the time taken to return to the lowest energy state is characterised by two 'relaxation' times: T1, the time for M_z to return to its maximum value, and T2 (and T2*) the time for M_{xy} to return to zero.

T1 processes. At equilibrium, the net magnetization vector M_0 lies along the direction of the applied magnetic field B_0, and the transverse magnetization is zero i.e. $M_0 = (0, 0, M_z)$. The net magnetization M_z can be made zero by applying an RF pulse at the Larmor frequency, and the decay of the net magnetisation is

$$M_z = M_0[\ 1 - \exp(-t/\mathrm{T1})\ ] \qquad \text{(A2.6)}$$

where t is time since removal of the RF pulse (when $M_z = 0$) and T1 is the spin-lattice relaxation time. T1 increases as applied field B_0 increases, and typically is 0.1 – 1 msec for soft tissues, and 1 – 4 msec for water and cerebro-spinal fluid. At time $t \approx 5*T1$, $M_z \approx M_0$.

T2 Processes. If the net magnetization is rotated into the *xy* plane by a 90° RF pulse, it rotates about the *z* axis at the Larmor frequency. During rotation, the net magnetization dephases as each proton experiences a slightly different magnetic field strength and rotates at its own Larmor frequency. The time constant that describes return of the transverse magnetization, M_{xy}, to its equilibrium value, M_{xyo}, is the spin-spin relaxation time T2

$$M_{xy} = M_{xyo} \exp(-t/T2) \qquad \text{(A2.7)}$$

T2 is an intrinsic property of a material determined by its structure, independent of the applied static magnetic field, and typically is 50 – 200 msec. Molecular interactions and inhomogeneity in the local magnetic field strength both contribute to decay of transverse magnetization M_{xy}. The time constant that includes these extrinsic effects is labelled T2*

$$1/T2^* = 1/T2 + 1/T2_{inhomogeneity}. \qquad \text{(A2.8)}$$

An antenna receiver sensitive to the transverse magnetisation (M_{xy} forms the basis of all MRI data) records a free induction decay (FID) signal oscillating at the Larmor frequency and decaying with time constant T2*.

Figure A2-2: Dependence of relaxation times T1 and T2 on molecular properties. T2 is always less than or equal to T1. From Bushberg *et al* 2002.

Figure A2-2 demonstrates the dependence of T1 and T2 upon molecular motion (temperature), physical size, and type of interaction. As the static magnetic field strength increases T1 will increase and T2 (and T2*) will decrease, however the changes are not uniform for all tissues. As differences in T1 and T2 relaxation times between tissues are at the core of MR contrast, the changes may not be advantageous. For example, at 3 T the T1 relaxation times for white and grey matter converge and their contrast is reduced (Kuhl *et al.*, 2008b). Similarly, diseased tissue appears less dark on a high-field T1-weighted image.

Spin-Echo pulse sequencing. The amplitude of an MR signal after a single 90° RF excitation pulse decays with time constant T2* as the net magnetisation M_{xy} de-phases and decays due to intrinsic magnetic field inhomogeneities such as susceptibility changes at tissue interfaces, and extrinsic magnetic field variations. De-phasing can be reversed by applying a 180° inversion pulse at time TE/2 and an 'echo' signal is formed at time TE. The relaxation time TR is long enough to allow recovery of the magnetisation M_z that has relaxation time T1 (figure A2-3). The 180° pulse can be repeated many times within a pulse 'sequence' to generate many echoes, with echo peaks defining the T2 decay curve (each echo decays with time constant T2*). After time TR the sequence is repeated, typically *n* times, to acquire sufficient data for image formation.

Figure A2-3: Spin-echo pulse sequence timing. From Bushberg *et al* 2002.

The spin-echo pulse sequence shown in figure 55 is one of the most commonly used MR sequences – Pooley (2005) or Bitar *et al* (2006) provide a summary, and Plewes (1994) focuses on spin-echo sequences in particular. It forms the basis of fast spin-echo (FSE/TSE), echo planar imaging (EPI), and gradient and spin echo (GRASE). Spin-echo sequences are robust against local magnetic field inhomogeneities and susceptibility artifact because the free induction decay and echo vectors point in opposite directions and add destructively – an important consideration when seeking images from patients with

bilateral metal hip prostheses. In contrast, another common sequence, Gradient Recalled Echo (GRE) tends to emphasise tissue (or prosthesis) susceptibility artifacts, and magnetic field inhomogeneity, because the free induction decay and echo vectors point in the same direction and add constructively, rather than cancelling out as in spin-echo sequences.

Spatial MR signal encoding. To obtain a spatially-encoded MR image the Larmor frequency or signal phase must vary as a function of position on *x*, *y* and *z* axes. However, with only a static magnetic field B_0, all protons in the field precess at the Larmor frequency and individual voxels cannot be resolved. Selectivity is achieved by adding linear gradient fields to the static field B_0. The added fields are small compared with B_0, and are zero at the centre of the FOV. By selectively detecting different frequencies and observing the signal phase, *x*, *y*, and *z* co-ordinates of a detected signal can be determined.

Slice select. A slice selection gradient is applied during RF excitation, and it modifies the precession frequency of protons so that only those at a certain axial position absorb energy (and hence provide signal) due to resonance. In this way, the applied RF pulse frequency corresponds to selectivity in the axial direction. Pulse bandwidth and waveform determine slice thickness and profile. A *sinc* pulse = *sin(z)/z* provides a square slice profile, and steeper field gradients provide thinner slices. After selecting a particular axial slice, 2D spatial reconstruction within the slice is achieved using 2D Fourier transformation in k-space via frequency and phase encoding (in the following discussion frequency encodes *x* direction and phase encodes *y* direction):

***k*-space and Fourier transformation.** 2D Fourier transformation in *k*-space (Twieg, 1983; Ljunggren, 1983) is widely used for signal processing and image formation in MRI. Only a brief description is warranted here (readers are referred to Twieg's original paper, or almost any MRI textbook for additional detail). Briefly, a 2-dimensional grid is defined in *k*-space. A frequency encoding RF pulse (FEG, *x* direction) and phase encoding RF pulse (PEG, *y* direction) correspond to *k*-space parameters k_{FEG} and k_{PEG} defined such that

$$k_{FEG} = m\,\gamma B_{FE}\Delta t \qquad \text{(A2.9)}$$

$$k_{PEG} = n\,\gamma B_{PE}\tau \qquad \text{(A2.10)}$$

where Δt is sampling time and m is sample number in the frequency encoding direction, while τ is the duration of phase encoding gradient and n is sample number in phase encoding direction. With each PEG pulse an entire row of data is acquired for the k-space grid. A 2D-Fourier transform of encoded signals represents the spin density distribution in two dimensions – low spatial frequencies are encoded towards the grid centre and provide contrast resolution, while high spatial frequencies are encoded towards the grid edges and contribute to spatial resolution. k-space has the same number of rows and columns as the final image, and thus determines the spatial resolution of a transverse slice.

Frequency encoding. A frequency encode gradient is applied perpendicular to the slice encode gradient for the duration of the FID decay of spins excited by the slice encode gradient. Proton resonance frequency is determined by distance from the FOV centre, where the added field is zero. While the frequency encoding gradient is applied, signal is digitized at regular time intervals. Fourier transformation of recorded data yields signal amplitudes at different frequencies, binned into columns in the x direction. A frequency encode (readout) gradient causes the position in k-space to advance at a constant rate in the x direction. Thus, all data points acquired during readout are equally spaced along one line in k-space. Spatial resolution in the frequency encoding direction is determined by the acquisition window time width Δt (which determines frequency resolution) and the frequency-encoding gradient strength.

Phase encoding. Initially Larmor frequencies and phase angles are all identical in the phase encode (y) direction. A short RF pulse applied soon after the slice-encode gradient leads to position-dependent phase in the FID decay signal: while the gradient is on, Larmor frequencies are position dependent (hence phase is position dependent). When the gradient is switched off, Larmor frequencies are again the same, but the phase angles are different. The slope of the phase-encoding gradient is incremented in each of n pulse sequences. During readout, the signal phase is different in different columns in the y direction, with largest and most rapid sinusoidal variation at the FOV edges, and near zero at the centre. 2D Fourier transformation yields total signal amplitudes for columns in the y direction.

MR image contrast. The observed MR signal intensity is related to the transverse magnetisation magnitude M_{xy}, and in a spin-echo pulse sequence is

$$Signal \propto \rho_H [1-\exp(-TR/T1)] \exp(-TE/T2) \qquad (A2.11)$$

where ρ_H is proton (spin) density, and other parameters were defined earlier. By selectively tuning pulse repetition times TE and TR, operators can choose what is emphasised in reconstructed MR images. For example, proton density is highlighted by selecting short TE (around 20 msec) and long TR, while a 'T1 weighted' image is obtained with short TE (10 - 20 msec) and short TR (300 - 600 msec). A 'T2 weighted' image is acquired with long TE (> 60 msec) and long TR (> 1600 msec).

Figure A2-4: Examples of contrast in MR images with spin-echo pulse sequences designed to emphasise (a) T1, (b) proton density (c) T2 features. From Bushberg *et al* 2002.

Examples of contrast in MR images with different spin-echo pulse sequences are shown in figure A2-4. Sequences can emphasise T1 features (figure A2-4a) – bright for short T1 tissue such as fat, or proton density (figure A2-4b) – bright for higher proton density and with higher signal intensity but reduced contrast or T2 (figure A2-4c) – bright for long T2.

A2.3 Computed Tomography.

The first commercially available implementation of X-ray projection computed tomography (CT) was described in 1973 with a triplet of papers in the British Journal of Radiology (Hounsfield, 1973; Perry and Bridges, 1973; Ambrose, 1973). While not first to recognise the potential of x-ray tomographic imaging – see a summary by Webb (1992) – Godfrey Hounsfield shared the 1979 Nobel prize in Medicine with Alan Cormack, an earlier researcher working on CT imaging (Hounsfield, 1992; Cormack, 1992). Even in Hounsfield's 1973 paper where he described a CT system and introduced the now-familiar CT number scale, the evolution from single-slice to multi-slice CT scanning was recognised. At the same time, Ambrose demonstrated the potential of CT in clinical

applications, and discussed use of contrast agents and the importance of patient immobilisation. Perry and Bridges noted the integral radiation dose from a single-slice scan was likely to be less than that from a conventional plane film radiograph. Since 1973, CT has evolved into a widely-used imaging modality, finding application in medical settings and in areas as diverse as non-destructive testing of mechanical components and explosives detection (Smith *et al.*, 2009c) in airport baggage security.

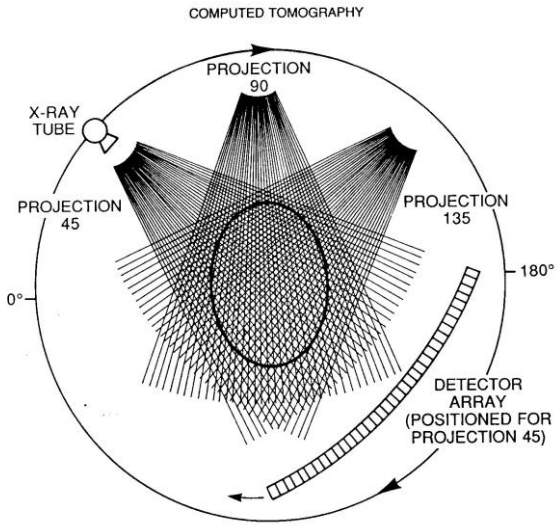

Figure A2-5: Schematic of CT x-ray source and detectors. Objects to be scanned are placed in the collimated x-ray fan beam emitted from an x-ray tube, and the tube and detector array rotate around the object. Slices are defined in the *xy* plane, and slice width in the *z*-direction.

Filtered back-projection (FBP) of x-ray projection data remains the backbone of CT image reconstruction techniques, and the development of exact analytic solutions for helical cone-beam CT image reconstruction algorithms (Katsevich, 2002) mean that efficient analytic reconstructions from x-ray projection data can be achieved even with truncated data sets, and for different scanning path trajectories. In unison with increased computing power, computationally intensive statistical iterative reconstruction techniques are gaining momentum (Fessler, 2000; Wang *et al.*, 2008b) but are yet to be made commercially available, despite being used in Hounsfield's original CT system. Based upon expectation-maximisation algorithms that estimate the most likely image to be formed from a given object (Lange and Carson, 1984), iterative techniques offer better noise suppression and improved contrast resolution. The improved artifact reduction of iterative techniques is particularly attractive when high-Z objects are in the field of view. The potential to improve image quality with simultaneous and significant dose reduction (Silva *et al.*, ; Hara *et al.*, 2009), is driving development of iterative techniques.

Metal and other high-density objects are often present in the CT field of view, and in this work the objects of interest are orthopaedic prosthetic hip implants located laterally about the prostate and implanted HDR brachytherapy needles. Artifacts generated by these high density objects potentially will become even more problematic as CT cone beam angles increase, and particularly with the introduction of dual-source CT devices since then beam-hardening artifacts will need to be suppressed to extract energy-dependent image data. Techniques like the alternating iteration scheme (Williamson *et al.*, 2002; O'Sullivan and Benac, 2007) may offer a way forward. However, until such reconstruction techniques are commercially available, clinical departments must rely upon specific and often proprietary Metal Artifact Reduction (MAR) techniques supplied with their CT scanner. As was shown earlier, the effectiveness of commercial solutions is variable.

Physics of CT.

CT is an x-ray projection technique, and photoelectric absorption and Compton scattering are the dominant physical processes that attenuate CT x-ray signal. Pair production is negligible at typical CT energies. Photoelectric absorption dominates between 50 - 100 keV, and occurs when the total energy of an incoming x-ray photon is transferred to an inner-shell electron, causing the electron to be ejected. In Compton scattering, which dominates above about 100 keV, an incoming photon transfers only part of its energy to an outer-shell electron that is subsequently ejected, while the photon is deflected in a different direction. The important difference is that photoelectric absorption $\propto Z^3$, where Z is the attenuating material's atomic number, and Compton scattering $\propto Z$. Since an incident photon is scattered rather than absorbed in Compton scattering, image blur due to scatter is more pronounced at higher energies. Low-energy x-rays are more sensitive to differences in material composition, and there is less scatter from low energy beams, but at the expense of reduced penetration and increased image noise.

The mathematics of CT image reconstruction is well understood, and the reader is referred to introductory texts such as that by Bushberg *et al* (2002), or more detailed clinical texts (Webb *et al.*, 2005), or to online resources such as the UK National Health Service (http://www.impactscan.org/slides/impactcourse/basic_principles_of_ct/index.html). A comparatively brief and non-mathematical description is given here:

X-rays projected along a ray through an object are absorbed and scattered by the object, and the resulting loss of signal intensity is

$$I = I_0 \exp(-\mu_{av} t) \qquad \text{(A2.12)}$$

where I_0 is incident x-ray intensity, t is object thickness and μ_{av} is average linear attenuation coefficient along the x-ray path. By dividing the x-ray path into N elements of thickness Δt so that $t = N\Delta t$, the intensity recorded at the detector is

$$I = I_0 \prod_{i=1}^{N} \exp\left(-\mu_i \Delta t\right) \qquad \text{(A2.13)}$$

If the location of element Δt is known, one can construct a detailed map of the variation of linear attenuation coefficient μ_i in the object. One advantage of CT imaging is that μ_i depends only upon the ratio I/I_0 and not their absolute values, so that machine-dependent parameters such as incident x-ray intensity I_0 are less important. In contrast, an underexposed film radiograph appears too white, and overexposed films appear too dark.

In 1917 Radon demonstrated the possibilities of tomographic reconstruction when he showed that any object could be reconstructed from an infinite number of line integrals, or projections, through the object (Radon, 1986 - english translation). Early in the 1960's Cormack (1963, 1964) applied the Radon transform to x-ray projection data acquired from an x-ray source and detector system rotating around an object. Hounsfield in 1973 reported the first commercial device, which relied as much upon mathematics as it did upon hardware. In modern scanners a single-source x-ray fan beam and a multi-element detector rotate around an object and thousands of projections are acquired at different angles.

Data for a single CT slice is recorded and displayed in a sinogram, which is simply a plot of projected x-ray intensity versus detection angle. Figure A2-6 shows a sinogram obtained from an industrial object. It is a 2-dimensional plot of average linear attenuation coefficient $\mu_{av}(r,\theta)$, with detection angle θ on the horizontal axis, and detector position r on the vertical axis. A sinogram contains sinusoidal patterns generated by scanned objects, with those closer to FOV edges producing sine waves of greater amplitude than objects closer to the FOV centre. Objects that cause more x-ray attenuation (i.e. have higher linear attenuation coefficient) appear darker, and sinusoid width represents object dimension.

NOTE:
This figure is included on page 120 of the print copy of the thesis held in the University of Adelaide Library.

Figure A2-6: Sinogram of projection data acquired from the object shown at right (Illerhaus *et al.*, 1997).

Image reconstruction is the mathematical conversion of a sinogram into a two-dimensional map of attenuation coefficient $\mu(x,y)$. Filtered back-projection is the most widely used technique – Goldman (2007) gives a summary, as do most CT textbooks: for a given x-ray source location θ, attenuation along a ray r through an object is known from the value at $\mu_{av}(r,\theta)$. This allows the average attenuation coefficient along that ray to be assigned (backprojected) to each pixel along the ray. The backprojection is repeated for every ray and every angle. The actual attenuation coefficient at a given pixel is the sum of all values from all ray projections that pass though that pixel. In practice, projected rays do not pass exactly through the centre of every pixel along their path and techniques such as nearest neighbour interpolation are used to determine accurate linear attenuation coefficients for each pixel. However, simple backprojection leads to $1/r$ blurring of reconstructed images, and suitable filters must be convolved with image data to eliminate blur. Transferring data into the Fourier (frequency) domain simplifies the convolution process into a simple multiplication of Fourier transformed image data with the selected filter's Fourier transform, followed by inverse Fourier transformation of convolved data back into the spatial (x,y) domain for backprojection. The simplest filter $H(\omega)$ that eliminates $1/r$ blurring is a ramp filter (Ramachandran and Lakshminarayanan, 1971)

$$H(\omega) = |\omega| \qquad \text{(A2.14)}$$

where ω is frequency in the Fourier domain. Unfortunately, the Ram-Lak filter is sensitive to noise because high frequencies ω that typify noise data are multiplied to a greater degree

than low frequencies. Usually, more complex filters that include varying degrees of high-frequency 'roll-off' reduce noise in backprojected images

$$H(\omega) = \begin{cases} |w| sinc\left(\frac{\omega}{\omega_{max}}\right) & |\omega| \leq \omega_{max} \\ 0 & |\omega| > \omega_{max} \end{cases} \qquad \text{(A2.15)}$$

The Shepp-Logan filter (Shepp and Logan, 1974) shown in eqn A2.15 reduces noise and causes only a small amount of blur, but does reduce the spatial resolution of images. Various other filters can be applied in the Fourier domain to highlight or diminish selected features in reconstructed data. For example, a typical 'bone' filter accentuates higher frequencies (i.e. locations where rapid changes in attenuation coefficient occur, such as at bone-tissue, prosthesis-tissue or a needle-tissue interfaces) while a 'soft tissue' filter reduces noise to improve contrast resolution, but at the expense of edge detail.

Following inverse Fourier transformation of filtered data, sinogram data are assigned to a 12-bit scale in which 4096 'bins' of width 1 HU are possible. The linear attenuation coefficients are converted to a 'CT number' or Hounsfield Unit (HU) number scale

$$HU = 1000\ (\mu_{pixel} - \mu_{water})/\ \mu_{water} \qquad \text{(A2.16)}$$

where μ_{water} is the linear attenuation coefficient of water. In this system the CT number of air is -1000 and of water is 0. Most soft tissues have CT numbers in the range -200 to 200, and bone ranges from about 600 to over 2000. Stainless steel needles have a CT number around 3700 HU while typical prostheses have CT numbers above 4000 HU. Recently, extended CT number scales were implemented to assist discrimination between high density objects such as hip prostheses and brachytherapy needles, and to better approximate linear attenuation coefficients for radiotherapy treatment planning (Coolens and Childs, 2003). In an extended CT number scale each of the 4096 bins spans 10 HU (spanning 40960 HU compared with 4096 HU), but at the expense of contrast resolution. As fats typically have CT numbers around -200 HU and the CT number of prostate tissue is similar to that of other tissues at around 40 HU, reduced contrast resolution can be problematic. CT numbers are known to be slightly dependent upon scanner kVp and mAs settings (Ebert *et al.*, 2008), but in most cases the influence on dosimetry is small.

Appendix 3

A3.1 BiLateral Implant Prostate (BLIP) Phantom.

As discussed in Chapter 4, it was essential in many cases to use a phantom rather than a real patient when working towards optimised image parameterisation. The phantom had to be of reasonable dimension and weight for transport, be suitably stable, but also modular so that different combinations of prostheses and needle implants (stainless steel or plastic) could be interchanged and tested in combination.

In this study, the BLIP phantom was constructed around three unplasticised poly-vinyl chloride (U-PVC) tubes. U-PVC is a plastic polymer $(\text{-}CH_2\text{-}CHCl\text{-})_n$, where n = 500 – 1500. The plastic is typically used for piping and usually contains a small amount of UV-stabiliser such as titanium dioxide (TiO_2). The density of U-PVC is typically 1.35-1.45 gcm^{-3}, and the observed CT number here was 903 ± 55 HU. The central tube was 75 mm diameter with 4.2 mm wall thickness. The two outer tubes were initially made from the same length of pipe, but were later increased to 90 mm outside diameter with 2.2 mm wall thickness to better accommodate acetabular cups into the modules. The outer tubes were set at 170 mm centre-to-centre spacing. The phantom was approximately 160 mm deep. To save bulk and weight, the phantom block was made 280 mm x 200 mm wide. The final BLIP phantom is shown in coronal and lateral CT scout images in figure A3-1 and A3-2.

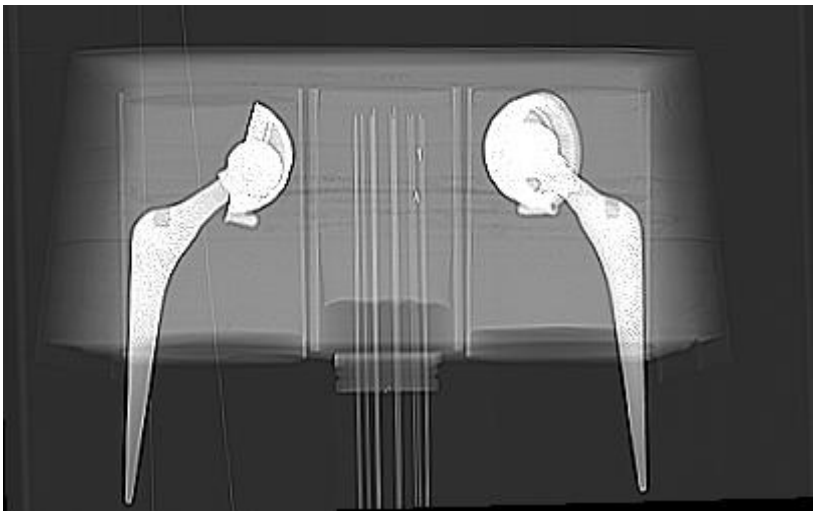

Figure A3-1: Coronal CT scout image of SCGH Bilateral Implant Prostate (BLIP) phantom, constructed from wax with PVC inserts to accept hip prosthesis and brachytherapy needle ‘modules’. Hip prostheses and a typical needle module (centre) are shown.

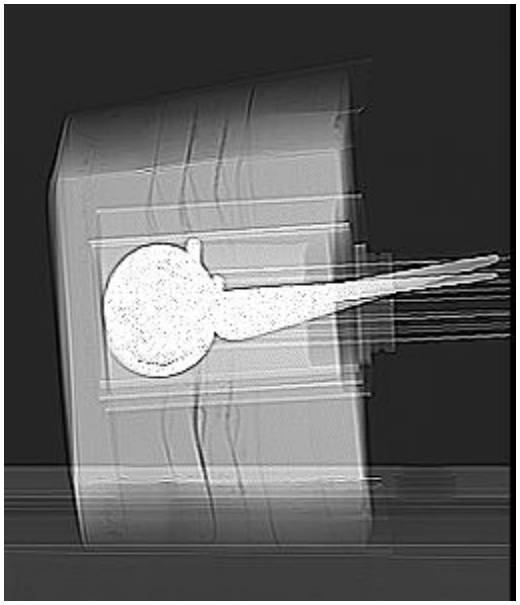

Figure A3-2: Lateral CT scout image of SCGH Bilateral Implant Prostate (BLIP) phantom, Small air gaps between wax layers, poured in stages, are visible. Prostheses and needle modules are visible.

The lateral dimensions and spacings in the phantom would match a small man; unfortunately many of our patients were larger, and some were significantly larger, however given that the most significant impact upon image quality was expected to be the metal prostheses, the compact nature of the phantom was not expected to be problematic.

The phantom 'body' was constructed initially using agar jelly, which yielded a CT number of 130 ± 23HU, however the agar gel was not sufficiently stable and the spatial reproducibility of the phantom was not reliable. As well, over a period of months the agar gel dehydrated and shrank and the original phantom had to be disposed. To eliminate spatial instability and to provide a rigid phantom that would not deteriorate over time, a second phantom of similar dimensions was constructed (shown in figure 4-1) but this time molten paraffin wax (C_nH_{2n+2}, with $20 < n < 40$, density = 0.93 gcm^{-3}) was used to fill the spaces around the U-PVC tubes, and allowed to set. The hardened paraffin wax demonstrated excellent rigidity and long term stability. The CT number of the paraffin wax was -61 ± 23 HU. The hip prostheses and the needle implants were similarly embedded in molten wax, with care being taken to minimise air bubbles in the mixture. The prosthesis and needle modules were made to fit inside the U-PVC tubes with a 0.5-1 mm air gap all round (a push-fit version to eliminate the air gaps was attempted, but the clearances proved insufficient for repeated use). Later, the phantom shown in figures A3-1 and A3-2 was

constructed from the same wax, with larger prosthesis modules to better accommodate the acetabular cups.

Several wax modules were constructed that contained acetabular cups and femoral stems in typical implant geometry. The acetabular cups were all titanium, while stainless steel, cobalt-chrome and titanium femoral stems and heads were installed into the modules. The prostheses were typical of those encountered in patients in this study.

Brachytherapy needle implant modules (plastic and stainless steel) replicated the implanted needle patterns used at SCGH, consisting of 15 implanted needles in a standard AOS 17-gauge prostate brachytherapy Syed-Neblet template. A Foley catheter and balloon were included to represent the urethra.

References

AAOS 2009 Facts on Hip Replacements *Am Assoc Orth Surg*

ABS 2009 3101.0 - Australian Demographic Statistics, Mar 2009 Australian Bureau of Statistics)

Ackerman I N, Dieppe P A, March L M, Roos E M, Nilsdotter A K, Brown G C, Sloan K E and Osborne R H 2009 Variation in age and physical status prior to total knee and hip replacement surgery: a comparison of centers in Australia and Europe *Arthritis Rheum* **61** 166-73

Ahmad S, Vogds B J, McKenna F and Vlachaki M T 2009 Tumor control probability (TCP) in prostate cancer: role of radiobiological parameters and radiation dose escalation *J Xray Sci Technol* **17** 347-54

AIHW 2005 Prostate cancer. Australian Institute of Health and Welfare Australian Government)

Alicikus Z A, Yamada Y, Zhang Z, Pei X, Hunt M, Kollmeier M, Cox B and Zelefsky M J 2011 Ten-year outcomes of high-dose, intensity-modulated radiotherapy for localized prostate cancer *Cancer* **117** 1429-37

Ambrose J 1973 Computerized transverse axial scanning (tomography): Part 2. Clinical application *The British Journal of Radiology* **46** 1023-47

Arias E 2007 United States Life Tables, 2004 *National Vital Statistics Reports* **56**

Atalar E and Menard C 2005 MR-guided interventions for prostate cancer *Magn Reson Imaging Clin N Am* **13** 491-504

Bachand F, Martin A G, Beaulieu L, Harel F and Vigneault E 2009 An eight-year experience of HDR brachytherapy boost for localized prostate cancer: biopsy and PSA outcome *Int J Radiat Oncol Biol Phys* **73** 679-84

Barrett J F and Keat N 2004 Artifacts in CT: recognition and avoidance *Radiographics* **24** 1679-91

Barten P G J 1992 Physical model for the contrast sensitivity of the human eye. Human Vision, Visual Processing, and Digital Display III, *Proc. SPIE* **1666** 57-72

Barten P G J 1999 *Contrast Sensitivity of the Human Eye and Its Effects on Image Quality* vol PM72 (Bellingham: SPIE Press Monograph)

Bensamoun S, Ho Ba Tho M C, Luu S, Gherbezza J M and de Belleval J F 2004 Spatial distribution of acoustic and elastic properties of human femoral cortical bone *J Biomech* **37** 503-10

Bentzen S M and Ritter M A 2005 The alpha/beta ratio for prostate cancer: what is it, really? *Radiother Oncol* **76** 1-3

Bill-Axelson A, Holmberg L, Filen F, Ruutu M, Garmo H, Busch C, Nordling S, Haggman M, Andersson S O, Bratell S, Spangberg A, Palmgren J, Adami H O and Johansson J E 2008 Radical prostatectomy versus watchful waiting in localized prostate cancer: the Scandinavian prostate cancer group-4 randomized trial *J Natl Cancer Inst* **100** 1144-54

Birrell F and Felson D 2009 The age of osteoarthritis *Age Ageing* **38** 2-3

Birrell F, Johnell O and Silman A 1999 Projecting the need for hip replacement over the next three decades: influence of changing demography and threshold for surgery *Ann Rheum Dis* **58** 569-72

Bitar R, Leung G, Perng R, Tadros S, Moody A R, Sarrazin J, McGregor C, Christakis M, Symons S, Nelson A and Roberts T P 2006 MR Pulse Sequences: What Every Radiologist Wants to Know but Is Afraid to Ask1 *Radiographics* **26** 513-37

Blamire A M 2008 The technology of MRI--the next 10 years? *Br J Radiol* **81** 601-17

Bloch F 1946 Nuclear Induction *Physical Review* **70** 460

Bloch F 1964 *Nobel Lectures, Physics 1942-1962,* (Amsterdam: Elsevier Publishing Company)

Bloch F, Hansen W W and Packard M 1946 The Nuclear Induction Experiment *Physical Review* **70** 474

Boas F E and Fleischmann D 2011 Evaluation of Two Iterative Techniques for Reducing Metal Artifacts in Computed Tomography *Radiology*

Boesch C 2004 Nobel Prizes for nuclear magnetic resonance: 2003 and historical perspectives *J Magn Reson Imaging* **20** 177-9

Boutin P 1972 [Total arthroplasty of the hip by fritted aluminum prosthesis. Experimental study and 1st clinical applications] *Rev Chir Orthop Reparatrice Appar Mot* **58** 229-46
Bowes D and Crook J 2011 A critical analysis of the long-term impact of brachytherapy for prostate cancer: a review of the recent literature *Curr Opin Urol*
Brenner D J, Martinez A A, Edmundson G K, Mitchell C, Thames H D and Armour E P 2002 Direct evidence that prostate tumors show high sensitivity to fractionation (low alpha/beta ratio), similar to late-responding normal tissue *Int J Radiat Oncol Biol Phys* **52** 6-13
Burroughs B R, Hallstrom B, Golladay G J, Hoeffel D and Harris W H 2005 Range of Motion and Stability in Total Hip Arthroplasty With 28-, 32-, 38-, and 44-mm Femoral Head Sizes: An In Vitro Study *The Journal of Arthroplasty* **20** 11-9
Bushberg J T, Seibert J A and Leidholdt E M 2002 *The Essential Physics of Medical Imaging*: Lippincott Williams & Wilkins)
Cahlon O, Hunt M and Zelefsky M J 2008a Intensity-modulated radiation therapy: supportive data for prostate cancer *Semin Radiat Oncol* **18** 48-57
Cahlon O, Zelefsky M J, Shippy A, Chan H, Fuks Z, Yamada Y, Hunt M, Greenstein S and Amols H 2008b Ultra-high dose (86.4 Gy) IMRT for localized prostate cancer: toxicity and biochemical outcomes *Int J Radiat Oncol Biol Phys* **71** 330-7
Cameron H U 2002 *Hip Replacement Current Trends and Controversies,* ed R K Sinha (New York: Marcel Dekker Inc.)
Carmi E, Liu S, Alon N, Fiat A and Fiat D 2006 Resolution enhancement in MRI *Magn Reson Imaging* **24** 133-54
Cesaretti J A 2007 Brachytherapy for the treatment of prostate cancer *The cancer journal* **13** 302
Chadwick K H and Leenhouts H P 2005 Radiation risk is linear with dose at low doses *Br J Radiol* **78** 8-10
Chakeres D W and de Vocht F 2005 Static magnetic field effects on human subjects related to magnetic resonance imaging systems *Prog Biophys Mol Biol* **87** 255-65
Charnley J 1960 Surgery of the hip-joint: present and future developments *Br Med J* **1** 821-6
Charnley N, Morgan A, Thomas E, Wilson S, Bacon S, Wilson D and Bottomley D 2005 The use of CT-MR image registration to define target volumes in pelvic radiotherapy in the presence of bilateral hip replacements *Br J Radiol* **78** 634-6
Chen L, Price R A, Jr., Nguyen T B, Wang L, Li J S, Qin L, Ding M, Palacio E, Ma C M and Pollack A 2004 Dosimetric evaluation of MRI-based treatment planning for prostate cancer *Phys Med Biol* **49** 5157-70
Chernak E S, Rodriguez-Antunez A, Jelden G L, Dhaliwal R S and Lavik P S 1975 The use of computed tomography for radiation therapy treatment planning *Radiology* **117** 613-4
Cho Z H, Kim D J and Kim Y K 1988 Total inhomogeneity correction including chemical shifts and susceptibility by view angle tilting *Med Phys* **15** 7-11
CIRS 2007 Technical Manual, Electron Density Reference Phantom Model 062 *Computerized Imaging Reference Systems Inc.* 2428 Almeda Ave Suite 316, Norfolk, Virginia USA, 23513
Citrin D, Ning H, Guion P, Li G, Susil R C, Miller R W, Lessard E, Pouliot J, Huchen X, Capala J, Coleman C N, Camphausen K and Menard C 2005 Inverse treatment planning based on MRI for HDR prostate brachytherapy *Int J Radiat Oncol Biol Phys* **61** 1267-75
Coolens C and Childs P J 2003 Calibration of CT Hounsfield units for radiotherapy treatment planning of patients with metallic hip prostheses: the use of the extended CT-scale *Phys Med Biol* **48** 1591-603
Cormack A M 1963 Representation of a function by its line integrals, with some radiological applications. *Journal of Applied Physics* **34** 2722-7
Cormack A M 1964 Representation of a function by its line integrals, with some radiological applications 2 *Journal of Applied Physics* **35** 2908-13
Cormack A M 1992 *Nobel Lectures, Physiology or Medicine 1971-1980*
ed J Lindsten (Singapore World Scientific Publishing Co.)
Corner C, Rojas A M, Bryant L, Ostler P and Hoskin P 2008 A Phase II study of high-dose-rate afterloading brachytherapy as monotherapy for the treatment of localized prostate cancer *Int J Radiat Oncol Biol Phys* **72** 441-6

Cuckler J M, Moore K D, Lombardi A V, McPherson E and Emerson R 2004 Large versus small femoral heads in metal-on-metal total hip arthroplasty *The Journal of Arthroplasty* **19** 41-4

Czervionke L F, Daniels D L, Wehrli F W, Mark L P, Hendrix L E, Strandt J A, Williams A L and Haughton V M 1988 Magnetic susceptibility artifacts in gradient-recalled echo MR imaging *AJNR Am J Neuroradiol* **9** 1149-55

Dagenais S, Garbedian S and Wai E K 2009 Systematic review of the prevalence of radiographic primary hip osteoarthritis *Clin Orthop Relat Res* **467** 623-37

Damadian R 1971 Tumor detection by nuclear magnetic resonance *Science* **171** 1151-3

Damadian R 1980 Field focusing n.m.r. (FONAR) and the formation of chemical images in man *Philos Trans R Soc Lond B Biol Sci* **289** 489-500

Damore S J, Syed A M, Puthawala A A and Sharma A 2000 Needle displacement during HDR brachytherapy in the treatment of prostate cancer *Int J Radiat Oncol Biol Phys* **46** 1205-11

Demanes D J, Martinez A A, Ghilezan M, Hill D R, Schour L, Brandt D and Gustafson G 2011 High-Dose-Rate Monotherapy: Safe and Effective Brachytherapy for Patients with Localized Prostate Cancer *Int J Radiat Oncol Biol Phys*

DePuy Orthopaedics Australia Inc, 20 Howleys Rd Notting Hill VIC 3168, Australia

Deutsch I, Zelefsky M J, Zhang Z, Mo Q, Zaider M, Cohen G, Cahlon O and Yamada Y 2010 Comparison of PSA relapse-free survival in patients treated with ultra-high-dose IMRT versus combination HDR brachytherapy and IMRT *Brachytherapy* **9** 313-8

Dimitrievska S, Whitfield J, Hacking S A and Bureau M N 2009 Novel carbon fiber composite for hip replacement with improved <I>in vitro</I> and <I>in vivo</I> osseointegration *Journal of Biomedical Materials Research Part A* **91A** 37-51

Duchesne G M and Peters L J 1999 What is the alpha/beta ratio for prostate cancer? Rationale for hypofractionated high-dose-rate brachytherapy *Int J Radiat Oncol Biol Phys* **44** 747-8

Duchesne G M, Williams S G, Das R and Tai K H 2007 Patterns of toxicity following high-dose-rate brachytherapy boost for prostate cancer: mature prospective phase I/II study results *Radiother Oncol* **84** 128-34

Ebert M A, Lambert J and Greer P B 2008 CT-ED conversion on a GE Lightspeed-RT scanner: influence of scanner settings *Australas Phys Eng Sci Med* **31** 154-9

Ehman R L and Felmlee J P 1990 Flow artifact reduction in MRI: A review of the roles of gradient moment nulling and spatial presaturation *Magnetic Resonance in Medicine* **14** 293-307

Eskelinen A, Remes V, Helenius I, Pulkkinen P, Nevalainen J and Paavolainen P 2005 Total hip arthroplasty for primary osteoarthrosis in younger patients in the Finnish arthroplasty register. 4,661 primary replacements followed for 0-22 years *Acta Orthop* **76** 28-41

Eustace S, Goldberg R, Williamson D, Melhem E R, Oladipo O, Yucel E K and Jara H 1997 MR imaging of soft tissues adjacent to orthopaedic hardware: techniques to minimize susceptibility artefact *Clin Radiol* **52** 589-94

Evans P M 2008 Anatomical imaging for radiotherapy *Phys Med Biol* **53** R151-91

Fatyga M, Williamson J F, Dogan N, Todor D, Siebers J V, George R, Barani I and Hagan M 2009 A comparison of HDR brachytherapy and IMRT techniques for dose escalation in prostate cancer: a radiobiological modeling study *Med Phys* **36** 3995-4006

Fessler J A 2000 *Handbook Medical Imaging, Medical Image Processing and Analysis,,* ed M Sonka and J M Fitzpatrick (Bellingham, WA: : SPIE) pp 1–70.

Fowler J F 2005 The radiobiology of prostate cancer including new aspects of fractionated radiotherapy *Acta Oncol* **44** 265-76

Frank S J, Stafford R J, Bankson J A, Li C, Swanson D A, Kudchadker R J and Martirosyan K S 2008 A novel MRI marker for prostate brachytherapy *Int J Radiat Oncol Biol Phys* **71** 5-8

Fransson A, Andreo P and Potter R 2001 Aspects of MR image distortions in radiotherapy treatment planning *Strahlenther Onkol* **177** 59-73

Futterer J J, Engelbrecht M R, Jager G J, Hartman R P, King B F, Hulsbergen-Van de Kaa C A, Witjes J A and Barentsz J O 2007 Prostate cancer: comparison of local staging accuracy of pelvic phased-array coil alone versus integrated endorectal-pelvic phased-array coils. Local

staging accuracy of prostate cancer using endorectal coil MR imaging *Eur Radiol* **17** 1055-65
Geva T 2006 Magnetic resonance imaging: historical perspective *J Cardiovasc Magn Reson* **8** 573-80
Giaccia A J and Hall E J 2006 *Radiobiology For The Radiologist*: Lippincott Williams & Wilkins)
Gillespie W J, Frampton C M, Henderson R J and Ryan P M 1988 The incidence of cancer following total hip replacement *J Bone Joint Surg Br* **70** 539-42
Gleason D F and Mellinger G T 1974 Prediction of prognosis for prostatic adenocarcinoma by combined histological grading and clinical staging. *The Journal of Urology* **111** 58-65
Glover G H 1982 Compton scatter effects in CT reconstructions *Medical Physics* **9** 860-7
Goldman L W 2007 Principles of CT and CT technology *J Nucl Med Technol* **35** 115-28; quiz 29-30
Gomez P F and Morcuende J A 2005a Early attempts at hip arthroplasty--1700s to 1950s *Iowa Orthop J* **25** 25-9
Gomez P F and Morcuende J A 2005b A historical and economic perspective on Sir John Charnley, Chas F. Thackray Limited, and the early arthoplasty industry *Iowa Orthop J* **25** 30-7
Goodsitt M M, Carson P L, Witt S, Hykes D L and Kofler J M, Jr. 1998 Real-time B-mode ultrasound quality control test procedures. Report of AAPM Ultrasound Task Group No. 1 *Med Phys* **25** 1385-406
Graves S, Davidson D, de Steiger R and Tomkins A 2009 Hip and Knee Arthroplasty Annual Report 2009 *Australian Orthopaedic Association National Joint Replacement Registry*
Guedea F, Venselaar J, Hoskin P, Hellebust T P, Peiffert D, Londres B, Ventura M, Mazeron J J, Limbergen E V, Potter R and Kovacs G 2011 Patterns of care for brachytherapy in Europe: updated results *Radiother Oncol* **97** 514-20
Hangiandreou N J 2003 AAPM/RSNA physics tutorial for residents. Topics in US: B-mode US: basic concepts and new technology *Radiographics* **23** 1019-33
Hara A K, Paden R G, Silva A C, Kujak J L, Lawder H J and Pavlicek W 2009 Iterative reconstruction technique for reducing body radiation dose at CT: feasibility study *AJR Am J Roentgenol* **193** 764-71
Hartwig V, Giovannetti G, Vanello N, Lombardi M, Landini L and Simi S 2009 Biological effects and safety in magnetic resonance imaging: a review *Int J Environ Res Public Health* **6** 1778-98
Haworth A, Ebert M, Waterhouse D, Joseph D and Duchesne G 2004a Assessment of i-125 prostate implants by tumor bioeffect *Int J Radiat Oncol Biol Phys* **59** 1405-13
Haworth A, Ebert M, Waterhouse D, Joseph D and Duchesne G 2004b Prostate implant evaluation using tumour control probability--the effect of input parameters *Phys Med Biol* **49** 3649-64
Heijmink S W, Futterer J J, Hambrock T, Takahashi S, Scheenen T W, Huisman H J, Hulsbergen-Van de Kaa C A, Knipscheer B C, Kiemeney L A, Witjes J A and Barentsz J O 2007 Prostate cancer: body-array versus endorectal coil MR imaging at 3 T--comparison of image quality, localization, and staging performance *Radiology* **244** 184-95
Hellebust T P, Kirisits C, Berger D, Perez-Calatayud J, De Brabandere M, De Leeuw A, Dumas I, Hudej R, Lowe G, Wills R and Tanderup K 2010 Recommendations from Gynaecological (GYN) GEC-ESTRO Working Group: considerations and pitfalls in commissioning and applicator reconstruction in 3D image-based treatment planning of cervix cancer brachytherapy *Radiother Oncol* **96** 153-60
Hentschel B, Oehler W, Strauss D, Ulrich A and Malich A 2011 Definition of the CTV Prostate in CT and MRI by Using CT-MRI Image Fusion in IMRT Planning for Prostate Cancer *Strahlenther Onkol* **187** 183-90
Horch R A, Wilkens K, Gochberg D F and Does M D 2010 RF coil considerations for short-T2 MRI *Magn Reson Med* **64** 1652-7
Hoskin P J, Bownes P J, Ostler P, Walker K and Bryant L 2003 High dose rate afterloading brachytherapy for prostate cancer: catheter and gland movement between fractions *Radiother Oncol* **68** 285-8

Hosman A H, van der Mei H C, Bulstra S K, Busscher H J and Neut D 2009 Metal-on-metal bearings in total hip arthroplasties: Influence of cobalt and chromium ions on bacterial growth and biofilm formation *J Biomed Mater Res A* **88** 711-6

Hounsfield G N 1973 Computerized transverse axial scanning (tomography): Part 1. Description of system *The British Journal of Radiology* **46** 1016-22

Hounsfield G N 1992 *Nobel Lectures, Physiology or Medicine 1971-1980,* ed J Lindsten (Singapore: World Scientific Publishing Co.)

Huang X and Chen W 2005 A fast algorithm to reduce gibbs ringing artifact in MRI *Conf Proc IEEE Eng Med Biol Soc* **2** 1367-70

Huggins C and Hodges C V 1941 Studies on Prostatic Cancer. I. The Effect of Castration, of Estrogen and of Androgen Injection on Serum Phosphatases in Metastatic Carcinoma of the Prostate *Cancer Res* **1** 293-7

Illerhaus B, Goebbels J, Riesemeier H and Staiger H 1997 Correction techniques for detector systems in 3D-CT *Proceedings SPIE* **3152** 101-6

Jacobs M A, Ibrahim T S and Ouwerkerk R 2007 AAPM/RSNA physics tutorials for residents: MR imaging: brief overview and emerging applications *Radiographics* **27** 1213-29

Jasty M, Rubash H E and Muratoglu O 2005 Highly cross-linked polyethylene: the debate is over--in the affirmative *J Arthroplasty* **20** 55-8

Jelden G L, Chernak E S, Lavik P S, Dhaliwal R S and Rodriguez-Antunez A 1976a The use of computed tomography in radiation therapy treatment planning *J Belge Radiol* **59** 301-7

Jelden G L, Chernak E S, Rodriguez-Antunez A, Haaga J R, Lavik P S and Dhaliwal R S 1976b Further progress in CT scanning and computerized radiation therapy treatment planning *AJR Am J Roentgenol* **127** 179-85

Jemal A, Siegel R, Ward E, Hao Y, Xu J and Thun M J 2009 Cancer statistics, 2009 *CA Cancer J Clin* **59** 225-49

Katsevich A 2002 Analysis of an exact inversion algorithm for spiral cone-beam CT *Phys Med Biol* **47** 2583-97

Kaur P, Kumaran S S, Tripathi R P, Khushu S and Kaushik S 2007 Protocol error artifacts in MRI: Sources and remedies revisited *Radiography* **13** 291-306

Keall P J, Siebers J V, Jeraj R and Mohan R 2003 Radiotherapy dose calculations in the presence of hip prostheses *Med Dosim* **28** 107-12

Kellerer A M and Rossi H H 1971 RBE and the primary mechanism of radiation action *Radiat Res* **47** 15-34

Keyes M, Miller S, Moravan V, Pickles T, McKenzie M, Pai H, Liu M, Kwan W, Agranovich A, Spadinger I, Lapointe V, Halperin R and Morris W J 2009 Predictive factors for acute and late urinary toxicity after permanent prostate brachytherapy: long-term outcome in 712 consecutive patients *Int J Radiat Oncol Biol Phys* **73** 1023-32

Kiffer J D, Schumer W A, Mantle C A, McKenzie B J, Feigen M, Quong G G and Waterman F M 2003 Impact of oedema on implant geometry and dosimetry for temporary high dose rate brachytherapy of the prostate *Australas Radiol* **47** 172-6

Kim D Y, Schnall M D, Rosen M A and Connick T 2008 Prostate MR imaging at 3T with a longitudinal array endorectal surface coil and phased array body coil *J Magn Reson Imaging* **27** 1327-30

Kim Y, Hsu I C, Lessard E, Pouliot J and Vujic J 2004 Dose uncertainty due to computed tomography (CT) slice thickness in CT-based high dose rate brachytherapy of the prostate cancer *Med Phys* **31** 2543-8

Kim Y, Hsu I C, Pouliot J, Noworolski S M, Vigneron D B and Kurhanewicz J 2005 Expandable and rigid endorectal coils for prostate MRI: impact on prostate distortion and rigid image registration *Med Phys* **32** 3569-78

Kolind S H, MacKay A L, Munk P L and Xiang Q S 2004 Quantitative evaluation of metal artifact reduction techniques *J Magn Reson Imaging* **20** 487-95

Koukourakis G, Kelekis N, Armonis V and Kouloulias V 2009 Brachytherapy for prostate cancer: a systematic review *Adv Urol* 327945

Kovacs G, Potter R, Loch T, Hammer J, Kolkman-Deurloo I K, de la Rosette J J and Bertermann H 2005 GEC/ESTRO-EAU recommendations on temporary brachytherapy using stepping sources for localised prostate cancer *Radiother Oncol* **74** 137-48
Krug R, Stehling C, Kelley D A, Majumdar S and Link T M 2009 Imaging of the musculoskeletal system in vivo using ultra-high field magnetic resonance at 7 T *Invest Radiol* **44** 613-8
Krupski T L, Saigal C S, Hanley J, Schonlau M and Litwin M S 2006 Patterns of care for men with prostate cancer after failure of primary treatment *Cancer* **107** 258-65
Kuban D A, Tucker S L, Dong L, Starkschall G, Huang E H, Cheung M R, Lee A K and Pollack A 2008 Long-term results of the M. D. Anderson randomized dose-escalation trial for prostate cancer *Int J Radiat Oncol Biol Phys* **70** 67-74
Kuhl C K, Traber F, Gieseke J, Drahanowsky W, Morakkabati-Spitz N, Willinek W, von Falkenhausen M, Manka C and Schild H H 2008a Whole-body high-field-strength (3.0-T) MR imaging in clinical practice. Part II. Technical considerations and clinical applications *Radiology* **247** 16-35
Kuhl C K, Traber F and Schild H H 2008b Whole-body high-field-strength (3.0-T) MR Imaging in Clinical Practice. Part I. Technical considerations and clinical applications *Radiology* **246** 675-96
Kumar A, Welti D and Ernst R R 1975 NMR Fourier zeugmatography *Journal of Magnetic Resonance (1969)* **18** 69-83
Kunkler I ed 2003a *Effects of radiation on normal tissues*: Churchill Livingstone, Edinburgh)
Kunkler I ed 2003b *Principles of management and dosage*: Churchill Livingstone, Edinburgh)
Kurtz S, Ong K, Lau E, Mowat F and Halpern M 2007 Projections of primary and revision hip and knee arthroplasty in the United States from 2005 to 2030 *J Bone Joint Surg Am* **89** 780-5
Lange K and Carson R 1984 EM reconstruction algorithms for emission and transmission tomography *J Comput Assist Tomogr* **8** 306-16
Langham K, Camille P and Waterhouse D 2006 Needle movement in HDR prostate brachytherapy. In: *ABG 15th ASM,* (Adelaide
Larson T C, 3rd, Kelly W M, Ehman R L and Wehrli F W 1990 Spatial misregistration of vascular flow during MR imaging of the CNS: cause and clinical significance *AJR Am J Roentgenol* **155** 1117-24
Lauterbur P C 1973 Image Formation by Induced Local Interactions: Examples Employing Nuclear Magnetic Resonance *Nature* **242** 190–1
Lee W R 2009 Extreme hypofractionation for prostate cancer *Expert Rev Anticancer Ther* **9** 61-5
Li X, Lam K M and Shen L 2007 An adaptive algorithm for the display of high-dynamic range images *Journal of Visual Communication and Image Representation* **18** 397-405
Link T M, Berning W, Scherf S, Joosten U, Joist A, Engelke K and Daldrup-Link H E 2000 CT of metal implants: reduction of artifacts using an extended CT scale technique *J Comput Assist Tomogr* **24** 165-72
Liu P T, Pavlicek W P, Peter M B, Spangehl M J, Roberts C C and Paden R G 2009 Metal artifact reduction image reconstruction algorithm for CT of implanted metal orthopedic devices: a work in progress *Skeletal Radiol* **38** 797-802
Ljunggren S 1983 A simple graphical representation of fourier-based imaging methods *Journal of Magnetic Resonance (1969)* **54** 338-43
Lohmander L S, Engesaeter L B, Herberts P, Ingvarsson T, Lucht U and Puolakka T J 2006 Standardized incidence rates of total hip replacement for primary hip osteoarthritis in the 5 Nordic countries: similarities and differences *Acta Orthop* **77** 733-40
Lu W, Pauly K B, Gold G E, Pauly J M and Hargreaves B A 2009 SEMAC: Slice Encoding for Metal Artifact Correction in MRI *Magn Reson Med* **62** 66-76
Macovski A 2009 MRI: a charmed past and an exciting future *J Magn Reson Imaging* **30** 919-23
Mahnken A H, Raupach R, Wildberger J E, Jung B, Heussen N, Flohr T G, Gunther R W and Schaller S 2003 A new algorithm for metal artifact reduction in computed tomography: in vitro and in vivo evaluation after total hip replacement *Invest Radiol* **38** 769-75
Mansfield P 1977 Multi-planar image formation using NMR spin echoes *Journal of Physics C: Solid State Physics* **10** L55-L8

Mansfield P and Maudsley A A 1977 Medical imaging by NMR *The British Journal of Radiology* **50** 188-94
Martin J, Frantzis J, Eade T and Chung P 2011 Clinician's guide to prostate IMRT plan assessment and optimisation *J Med Imaging Radiat Oncol* **54** 569-75
Matthijs P 2003 Barco white paper. Grayscale resolution: how much is enough? http://www.barco.com/barcoview/downloads/GrayscaleResolution.pdf.
Menard C, Susil R C, Choyke P, Gustafson G S, Kammerer W, Ning H, Miller R W, Ullman K L, Sears Crouse N, Smith S, Lessard E, Pouliot J, Wright V, McVeigh E, Coleman C N and Camphausen K 2004 MRI-guided HDR prostate brachytherapy in standard 1.5T scanner *Int J Radiat Oncol Biol Phys* **59** 1414-23
Merx H, Dreinhofer K, Schrader P, Sturmer T, Puhl W, Gunther K P and Brenner H 2003 International variation in hip replacement rates *Ann Rheum Dis* **62** 222-6
Meziane A, Bou-Saïd B and John T 2008 Modelling human hip joint lubrication subject to walking cycle *Lubrication Science* **20** 205-22
Mitterberger M, Horninger W, Pelzer A, Strasser H, Bartsch G, Moser P, Halpern E J, Gradl J, Aigner F, Pallwein L and Frauscher F 2007 A prospective randomized trial comparing contrast-enhanced targeted versus systematic ultrasound guided biopsies: impact on prostate cancer detection *Prostate* **67** 1537-42
Mohan R, Chui C, Miller D and Laughlin J S 1981 Use of computerized tomography in dose calculations for radiation treatment planning *J Comput Tomogr* **5** 273-82
Morris W J, Keyes M, Palma D, McKenzie M, Spadinger I, Agranovich A, Pickles T, Liu M, Kwan W, Wu J, Lapointe V, Berthelet E, Pai H, Harrison R, Kwa W, Bucci J, Racz V and Woods R 2009 Evaluation of dosimetric parameters and disease response after 125 iodine transperineal brachytherapy for low- and intermediate-risk prostate cancer *Int J Radiat Oncol Biol Phys* **73** 1432-8
Morshed S, Bozic K J, Ries M D, Malchau H and Colford J M, Jr. 2007 Comparison of cemented and uncemented fixation in total hip replacement: a meta-analysis *Acta Orthop* **78** 315-26
Muller J and Buzug T M 2009 Spurious structures created by interpolation-based CT metal artifact reduction *Proc. SPIE* **7258** 72581Y
Mullerad M, Hricak H, Kuroiwa K, Pucar D, Chen H N, Kattan M W and Scardino P T 2005 Comparison of endorectal magnetic resonance imaging, guided prostate biopsy and digital rectal examination in the preoperative anatomical localization of prostate cancer *J Urol* **174** 2158-63
Mullokandov E and Gejerman G 2004 Analysis of serial CT scans to assess template and catheter movement in prostate HDR brachytherapy *International Journal of Radiation Oncology*Biology*Physics* **58** 1063-71
Muntener M, Patriciu A, Petrisor D, Schar M, Ursu D, Song D Y and Stoianovici D 2008 Transperineal prostate intervention: robot for fully automated MR imaging--system description and proof of principle in a canine model *Radiology* **247** 543-9
Nahum A E, Movsas B, Horwitz E M, Stobbe C C and Chapman J D 2003 Incorporating clinical measurements of hypoxia into tumor local control modeling of prostate cancer: implications for the alpha/beta ratio *Int J Radiat Oncol Biol Phys* **57** 391-401
Navarro M, Michiardi A, Castano O and Planell J A 2008 Biomaterials in orthopaedics *J R Soc Interface* **5** 1137-58
NEMA 2004 *PS3 - Digital Imaging and Communications in Medicine (DICOM)*: National Electrical Manufacturers Association, Virginia USA)
Nickers P, Hermesse J, Deneufbourg J M, Vanbelle S and Lartigau E 2010 Which alpha/beta ratio and half-time of repair are useful for predicting outcomes in prostate cancer? *Radiother Oncol* **97** 462-6
O'Sullivan J A and Benac J 2007 Alternating minimization algorithms for transmission tomography *IEEE Trans Med Imaging* **26** 283-97
Oehler M, Kratz B, Knopp T, Müller J and Buzug T M 2008 Evaluation of surrogate data quality in sinogram-based CT metal-artifact reduction *Proc. SPIE* **7076** 10

Pallwein L, Aigner F, Faschingbauer R, Pallwein E, Pinggera G, Bartsch G, Schaefer G, Struve P and Frauscher F 2008a Prostate cancer diagnosis: value of real-time elastography *Abdom Imaging* **33** 729-35

Pallwein L, Mitterberger M, Pelzer A, Bartsch G, Strasser H, Pinggera G M, Aigner F, Gradl J, Zur Nedden D and Frauscher F 2008b Ultrasound of prostate cancer: recent advances *Eur Radiol* **18** 707-15

Pan X, Siewerdsen J, La Riviere P J and Kalender W A 2008 Anniversary paper. Development of x-ray computed tomography: the role of medical physics and AAPM from the 1970s to present *Med Phys* **35** 3728-39

Pellizzon A C, Nadalin W, Salvajoli J V, Fogaroli R C, Novaes P E, Maia M A and Ferrigno R 2003 Results of high dose rate afterloading brachytherapy boost to conventional external beam radiation therapy for initial and locally advanced prostate cancer *Radiother Oncol* **66** 167-72

Perry B J and Bridges C 1973 Computerized transverse axial scanning (tomography): Part 3. Radiation dose considerations *The British Journal of Radiology* **46** 1048-51

Pfeiffer D, Sutlief S, Feng W, Pierce H M and Kofler J 2008 AAPM Task Group 128: Quality assurance tests for prostate brachytherapy ultrasound systems *Medical Physics* **35** 5471-89

Pieters B R, van de Kamer J B, van Herten Y R, van Wieringen N, D'Olieslager G M, van der Heide U A and Koning C C 2008 Comparison of biologically equivalent dose-volume parameters for the treatment of prostate cancer with concomitant boost IMRT versus IMRT combined with brachytherapy *Radiother Oncol* **88** 46-52

Pisansky T M, Gold D G, Furutani K M, Macdonald O K, McLaren R H, Mynderse L A, Wilson T M, Hebl J R and Choo R 2008 High-dose-rate brachytherapy in the curative treatment of patients with localized prostate cancer *Mayo Clin Proc* **83** 1364-72

Plewes D B 1994 The AAPM/RSNA physics tutorial for residents. Contrast mechanisms in spin-echo MR imaging *Radiographics* **14** 1389-404; quiz 405-6

Pooley R A 2005 AAPM/RSNA physics tutorial for residents: fundamental physics of MR imaging *Radiographics* **25** 1087-99

Port J D and Pomper M G 2000 Quantification and minimization of magnetic susceptibility artifacts on GRE images *J Comput Assist Tomogr* **24** 958-64

Porter B A, Hastrup W, Richardson M L, Wesbey G E, Olson D O, Cromwell L D and Moss A A 1987 Classification and investigation of artifacts in magnetic resonance imaging *Radiographics* **7** 271-87

Punnen S and Nam R K 2009 Indications and timing for prostate biopsy, diagnosis of early stage prostate cancer and its definitive treatment: a clinical conundrum in the PSA era *Surg Oncol* **18** 192-9

Purcell E M 1964 *Nobel Lectures, Physics 1942-1962,* (Amsterdam: Elsevier Publishing Company)

Purcell E M, Torrey H C and Pound R V 1946 Resonance Absorption by Nuclear Magnetic Moments in a Solid *Physical Review* **69** 37

Radon J 1986 On the Determination of Functions from Their Integral Values along Certain Manifolds *Medical Imaging, IEEE Transactions on* **5** 170-6

Ramachandran G N and Lakshminarayanan A V 1971 Three-dimensional reconstruction from radiographs and electron micrographs: application of convolutions instead of Fourier transforms *Proc Natl Acad Sci U S A* **68** 2236-40

Ramos-Cabrer P, van Duynhoven J P, Van der Toorn A and Nicolay K 2004 MRI of hip prostheses using single-point methods: in vitro studies towards the artifact-free imaging of individuals with metal implants *Magn Reson Imaging* **22** 1097-103

Reft C, Alecu R, Das I J, Gerbi B J, Keall P, Lief E, Mijnheer B J, Papanikolaou N, Sibata C and Van Dyk J 2003 Dosimetric considerations for patients with HIP prostheses undergoing pelvic irradiation. Report of the AAPM Radiation Therapy Committee Task Group 63 *Med Phys* **30** 1162-82

Ritter M 2008 Rationale, conduct, and outcome using hypofractionated radiotherapy in prostate cancer *Semin Radiat Oncol* **18** 249-56

Ritter M, Forman J, Kupelian P, Lawton C and Petereit D 2009 Hypofractionation for prostate cancer *Cancer J* **15** 1-6

Rivard M J, Venselaar J L and Beaulieu L 2009 The evolution of brachytherapy treatment planning *Med Phys* **36** 2136-53

Salvi A E, Grappiolo G, Moraca G and Spotorno L 2005 First implant acetabular components: historical aspects, a comparison of models and a review of the literature *Chir Organi Mov* **90** 323-37

Samei E, Badano A, Chakraborty D, Compton K, Cornelius C, Corrigan K, Flynn M J, Hemminger B, Hangiandreou N, Johnson J, Moxley-Stevens D M, Pavlicek W, Roehrig H, Rutz L, Shepard J, Uzenoff R A, Wang J and Willis C E 2005 Assessment of display performance for medical imaging systems: executive summary of AAPM TG18 report *Med Phys* **32** 1205-25

Sandhu G K, Dunscombe P B and Khan R F 2010 A pre-clinical phantom comparison of tissue harmonic and brightness mode imaging for application in ultrasound guided prostate brachytherapy *Phys Med*

Sargeant A and Goswami T 2006 Pathophysiological aspects of hip implants *J Surg Orthop Adv* **15** 111-2

Scannell P T and Prendergast P J 2009 Cortical and interfacial bone changes around a non-cemented hip implant: Simulations using a combined strain/damage remodelling algorithm *Medical Engineering & Physics* **31** 477-88

Schlamann M, Yoon M S, Maderwald S, Pietrzyk T, Bitz A K, Gerwig M, Forsting M, Ladd S C, Ladd M E and Kastrup O 2009 Short Term Effects of Magnetic Resonance Imaging on Excitability of the Motor Cortex at 1.5T and 7T *Acad Radiol*

Seppenwoolde Y, Kolkman-Deurloo I-K, Sipkema D, de Langen M, Praag J, Jansen P and Heijmen B 2008a HDR prostate monotherapy - Dosimetric effects of implant deformation due to posture change between TRUS- and CT-imaging *Radiotherapy and Oncology* **86** 114-9

Seppenwoolde Y, Kolkman-Deurloo I K, Sipkema D, de Langen M, Praag J, Jansen P and Heijmen B 2008b HDR prostate monotherapy: dosimetric effects of implant deformation due to posture change between TRUS- and CT-imaging *Radiother Oncol* **86** 114-9

Shelley M D, Kumar S, Wilt T, Staffurth J, Coles B and Mason M D 2009 A systematic review and meta-analysis of randomised trials of neo-adjuvant hormone therapy for localised and locally advanced prostate carcinoma *Cancer Treat Rev* **35** 9-17

Shellock F G and Kanal E 1998 Aneurysm clips: evaluation of MR imaging artifacts at 1.5 T *Radiology* **209** 563-6

Shepp L A and Logan B F 1974 Reconstructing Interior Head Tissue from X-Ray Transmissions *IEEE Trans. Nucl. Sci.* **21** 228-36

Silva A C, Lawder H J, Hara A, Kujak J and Pavlicek W Innovations in CT dose reduction strategy: application of the adaptive statistical iterative reconstruction algorithm *AJR Am J Roentgenol* **194** 191-9

Smith-Nephew Pty Limited, PO Box 242 Mount Waverley VIC 3149, Australia

Smith-Petersen M N 1948 Evolution of mould arthroplasty of the hip joint *J Bone Joint Surg Am* **30B** 59-75

Smith B D, Smith G L, Hurria A, Hortobagyi G N and Buchholz T A 2009a Future of cancer incidence in the United States: burdens upon an aging, changing nation *J Clin Oncol* **27** 2758-65

Smith R A, Cokkinides V and Brawley O W 2009b Cancer screening in the United States, 2009: a review of current American Cancer Society guidelines and issues in cancer screening *CA Cancer J Clin* **59** 27-41

Smith R C, Connelly J M, Maurice M and Jimmie C O 2009c *Aspects of Explosives Detection,* (Amsterdam: Elsevier) pp 131-45

Sobin L H, Gospodarowicz M K and Wittekind C eds 2009 *TNM Classification of Malignant Tumours, 7th Edition*: Wiley-Blackwell)

Sofka C M and Potter H G 2002 MR imaging of joint arthroplasty *Semin Musculoskelet Radiol* **6** 79-85

Sontag M R, Battista J J, Bronskill M J and Cunningham J R 1977 Implications of computed tomography for inhomogeneity corrections in photon beam dose calculations *Radiology* **124** 143-9
Sontag M R and Cunningham J R 1978 Clinical application of a CT based treatment planning system *Comput Tomogr* **2** 117-30
Sorantin E 2008 Soft-copy display and reading: what the radiologist should know in the digital era *Pediatr Radiol* **38** 1276-84
Sriprasad S, Feneley M R and Thompson P M 2009 History of prostate cancer treatment *Surg Oncol* **18** 185-91
Steel G G 2002 *Basic Clinical Radiobiology*: Hodder Arnold)
Stone N N, Potters L, Davis B J, Ciezki J P, Zelefsky M J, Roach M, Shinohara K, Fearn P A, Kattan M W and Stock R G 2009 Multicenter analysis of effect of high biologic effective dose on biochemical failure and survival outcomes in patients with Gleason score 7-10 prostate cancer treated with permanent prostate brachytherapy *Int J Radiat Oncol Biol Phys* **73** 341-6
Stradiotti P, Curti A, Castellazzi G and Zerbi A 2009 Metal-related artifacts in instrumented spine. Techniques for reducing artifacts in CT and MRI: state of the art *European Spine Journal* **18** 102-8
Stryker Australia Pty Ltd, 8 Herbert Street St Leonards NSW 2065 Australia
Sun L, Moul J W, Hotaling J M, Rampersaud E, Dahm P, Robertson C, Fitzsimons N, Albala D and Polascik T J 2007 Prostate-specific antigen (PSA) and PSA velocity for prostate cancer detection in men aged <50 years *BJU Int* **99** 753-7
Tartaglino L M, Flanders A E, Vinitski S and Friedman D P 1994 Metallic artifacts on MR images of the postoperative spine: reduction with fast spin-echo techniques *Radiology* **190** 565-9
Thomadsen B R, Williamson J F, Rivard M J and Meigooni A S 2008 Anniversary Paper: Past and current issues, and trends in brachytherapy physics *Medical Physics* **35** 4708-23
Thomsen M, Schneider U, Breusch S J, Hansmann J and Freund M 2001 [Artefacts and ferromagnetism dependent on different metal alloys in magnetic resonance imaging. An experimental study] *Orthopade* **30** 540-4
Tiong A, Bydder S, Ebert M, Caswell N, Waterhouse D, Spry N, Camille P and Joseph D 2009 A Small Tolerance for Catheter Displacement in High-Dose Rate Prostate Brachytherapy Is Necessary and Feasible *Int J Radiat Oncol Biol Phys*
Tubridy N and McKinstry C S 2000 Neuroradiological history: Sir Joseph Larmor and the basis of MRI physics *Neuroradiology* **42** 852-5
Turkbey B, Albert P S, Kurdziel K and Choyke P L 2009 Imaging localized prostate cancer: current approaches and new developments *AJR Am J Roentgenol* **192** 1471-80
Turpen R and Rosser C J 2009 Focal therapy for prostate cancer: revolution or evolution? *BMC Urol* **9** 2
Twieg D B 1983 The k-trajectory formulation of the NMR imaging process with applications in analysis and synthesis of imaging methods *Medical Physics* **10** 610-21
Valero J, Cambeiro M, Galan C, Teijeira M, Romero P, Zudaire J, Moreno M, Ciervide R, Aristu J J and Martinez-Monge R 2009 Phase II Trial of Radiation Dose Escalation with Conformal External Beam Radiotherapy and High-Dose-Rate Brachytherapy Combined with Long-Term Androgen Suppression in Unfavorable Prostate Cancer: Feasibility Report *Int J Radiat Oncol Biol Phys*
Varma G, Clough R E, Acher P, Senegas J, Dahnke H, Keevil S F and Schaeffter T Positive visualization of implanted devices with susceptibility gradient mapping using the original resolution *Magn Reson Med*
Visuri T, Pulkkinen P and Paavolainen P 2006 Malignant tumors at the site of total hip prosthesis. Analytic review of 46 cases *J Arthroplasty* **21** 311-23
Wan G, Wei Z, Gardi L, Downey D B and Fenster A 2005 Brachytherapy needle deflection evaluation and correction *Medical Physics* **32** 902-9

Wang C, Chao M, Lee L and Xing L 2008a MRI-based treatment planning with electron density information mapped from CT images: a preliminary study *Technol Cancer Res Treat* **7** 341-8

Wang G, Yu H and De Man B 2008b An outlook on x-ray CT research and development *Med Phys* **35** 1051-64

Wang J Z and Li X A 2003 Evaluation of external beam radiotherapy and brachytherapy for localized prostate cancer using equivalent uniform dose *Med Phys* **30** 34-40

Wang J Z, Li X A, Yu C X and DiBiase S J 2003 The low alpha/beta ratio for prostate cancer: what does the clinical outcome of HDR brachytherapy tell us? *Int J Radiat Oncol Biol Phys* **57** 1101-8

Warren J L, Yabroff K R, Meekins A, Topor M, Lamont E B and Brown M L 2008 Evaluation of trends in the cost of initial cancer treatment *J Natl Cancer Inst* **100** 888-97

Webb G A 2006 *Modern Magnetic Resonance, Volumes 1-3*: Springer - Verlag.)

Webb S 1992 Historical experiments predating commercially available computed tomography *Br J Radiol* **65** 835-7

Webb W R, Major N M and Brant W E 2005 *Fundamentals of Body CT* (Philadelphia, USA: Saunders Elsevier)

White L M, Kim J K, Mehta M, Merchant N, Schweitzer M E, Morrison W B, Hutchison C R and Gross A E 2000 Complications of total hip arthroplasty: MR imaging-initial experience *Radiology* **215** 254-62

Wiles P 1958 The surgery of the osteoarthritic hip *Br J Surg* **45** 488-97

Williams S G, Taylor J M, Liu N, Tra Y, Duchesne G M, Kestin L L, Martinez A, Pratt G R and Sandler H 2007 Use of individual fraction size data from 3756 patients to directly determine the alpha/beta ratio of prostate cancer *Int J Radiat Oncol Biol Phys* **68** 24-33

Williamson J F, Whiting B R, Benac J, Murphy R J, Blaine G J, O'Sullivan J A, Politte D G and Snyder D L 2002 Prospects for quantitative computed tomography imaging in the presence of foreign metal bodies using statistical image reconstruction *Med Phys* **29** 2404-18

Willinek W A and Schild H H 2008 Clinical advantages of 3.0 T MRI over 1.5 T *Eur J Radiol* **65** 2-14

Yazdi M, Gingras L and Beaulieu L 2005 An adaptive approach to metal artifact reduction in helical computed tomography for radiation therapy treatment planning: experimental and clinical studies *Int J Radiat Oncol Biol Phys* **62** 1224-31

Yoshida K, Nose T, Shiomi H, Yoshioka Y, Fujita Y, Kuroda S, Yoshida M, Takahashi T, Kitamura M, Akai H, Oka T and Hosoki T 2006 New ambulatory implant technique of high-dose-rate interstitial brachytherapy for prostate cancer *Radiat Med* **24** 595-9

Yoshida K, Yamazaki H, Nose T, Shiomi H, Yoshida M, Mikami M, Takenaka T, Kotsuma T, Tanaka E, Kuriyama K, Harada Y, Tohda A, Yasunaga Y and Oka T 2010 Needle applicator displacement during high-dose-rate interstitial brachytherapy for prostate cancer *Brachytherapy* **9** 36-41

Yu H, Zeng K, Bharkhada D K, Wang G, Madsen M T, Saba O, Policeni B, Howard M A and Smoker W R 2007 A segmentation-based method for metal artifact reduction *Acad Radiol* **14** 495-504

Zelefsky M J, Kuban D A, Levy L B, Potters L, Beyer D C, Blasko J C, Moran B J, Ciezki J P, Zietman A L, Pisansky T M, Elshaikh M and Horwitz E M 2007 Multi-institutional analysis of long-term outcome for stages T1-T2 prostate cancer treated with permanent seed implantation *Int J Radiat Oncol Biol Phys* **67** 327-33

Zelefsky M J, Yamada Y, Fuks Z, Zhang Z, Hunt M, Cahlon O, Park J and Shippy A 2008 Long-term results of conformal radiotherapy for prostate cancer: impact of dose escalation on biochemical tumor control and distant metastases-free survival outcomes *Int J Radiat Oncol Biol Phys* **71** 1028-33

Zhuo J and Gullapalli R P 2006 AAPM/RSNA physics tutorial for residents: MR artifacts, safety, and quality control *Radiographics* **26** 275-97

Zwanenburg J J, Hendrikse J, Visser F, Takahara T and Luijten P R 2009 Fluid attenuated inversion recovery (FLAIR) MRI at 7.0 Tesla: comparison with 1.5 and 3.0 Tesla *Eur Radiol*

A patient's perspective.

"if the Devil had a device that all men should fear, it would look like that"

HDR prostate brachytherapy patient, 2006

"if you'd shown me that thing before I said yes, I wouldn't have said yes"

HDR prostate brachytherapy patient, 2008

"it better bloody work aye?!"

HDR prostate brachytherapy patient, 2010